Plasma surface interactions at interlayer dielectric (ILD) and metal surfaces

by

Xin Liu

A Dissertation Presented in Partial Fulfillment
of the Requirements for the Degree
Doctor of Philosophy

Approved November 2012 by the
Graduate Supervisory Committee:

Robert Nemanich, Chair
Ralph Chamberlin
Tingyong Chen
David Smith
Fernando Ponce

ARIZONA STATE UNIVERSITY

December 2012

ABSTRACT

In this dissertation, remote plasma interactions with the surfaces of low-k interlayer dielectric (ILD), Cu and Cu adhesion layers are investigated. The first part of the study focuses on the simultaneous plasma treatment of ILD and chemical mechanical polishing (CMP) Cu surfaces using N_2/H_2 plasma processes. H atoms and radicals in the plasma react with the carbon groups leading to carbon removal for the ILD films. Results indicate that an N_2 plasma forms an amide-like layer on the surface which apparently leads to reduced carbon abstraction from an H_2 plasma process. In addition, FTIR spectra indicate the formation of hydroxyl (Si-OH) groups following the plasma exposure. Increased temperature (380 ℃) processing leads to a reduction of the hydroxyl group formation compared to ambient temperature processes, resulting in reduced changes of the dielectric constant. For CMP Cu surfaces, the carbonate contamination was removed by an H_2 plasma process at elevated temperature while the C-C and C-H contamination was removed by an N_2 plasma process at elevated temperature. The second part of this study examined oxide stability and cleaning of Ru surfaces as well as consequent Cu film thermal stability with the Ru layers. The ~2 monolayer native Ru oxide was reduced after H-plasma processing. The thermal stability or islanding of the Cu film on the Ru substrate was characterized by *in-situ* XPS. After plasma cleaning of the Ru adhesion layer, the deposited Cu exhibited full coverage. In contrast, for Cu deposition on the Ru native oxide substrate, Cu islanding was detected and was described in terms of grain boundary grooving and surface and interface energies. The thermal stability of 7 nm Ti, Pt and Ru

interfacial adhesion layers between a Cu film (10 nm) and a Ta barrier layer (4 nm) have been investigated in the third part. The barrier properties and interfacial stability have been evaluated by Rutherford backscattering spectrometry (RBS). Atomic force microscopy (AFM) was used to measure the surfaces before and after annealing, and all the surfaces are relatively smooth excluding islanding or de-wetting phenomena as a cause of the instability. The RBS showed no discernible diffusion across the adhesion layer/Ta and Ta/Si interfaces which provides a stable underlying layer. For a Ti interfacial layer RBS indicates that during 400 ℃ annealing Ti interdiffuses through the Cu film and accumulates at the surface. For the Pt/Cu system Pt interdiffuion is detected which is less evident than Ti. Among the three adhesion layer candidates, Ru shows negligible diffusion into the Cu film indicating thermal stability at 400 ℃.

DEDICATION

I dedicate this thesis to my wife Jie Wu, my parents Maoping Liu, Xiaomei Jin and my parents-in-law Shaopeng Wu, Xiaoxia Zheng, who have supported me throughout my doctoral research.

ACKNOWLEDGMENTS

The completion of this thesis would not be possible without the help of so many people. It is my great pleasure to acknowledge my advisor Dr. Robert Nemanich for his constant help and guidance throughout my graduate school study and research. His expertise in the physics and material science has helped me understand the problems and how to solve the problem. His dedication and enthusiasm in research are inspiring me for my life.

I would like to thank all of my group members that helped me in my Ph.D. study. I am grateful to Franz Koeck who built up the whole lab and taught me all the knowledge about vacuum techniques. I appreciate Dr. Fu Tang's and Dr. Chiyu Zhu's help since I joined the group as a fresh Ph.D. student. They trained me on all the equipment and have discussing with any research questions. I would like to extend my appreciation to Dr. Yang Sun, and Dr. Gary Hembree for their supports in microscopy experiments. Thanks to all my colleagues Tianying Sun, Sandeep Gill, Jialing Yang, Brianna Eller, and Manpuneet Kaur who help me with any questions I got. I wish to thank Dr. Sean King from Intel Corporation for providing all the samples and all the mentorship and discussions in the three years. Many thanks to Semiconductor Research Corporation for the financial support.

I am grateful to my wife, my parents and parents in-law for their lasting love and support.

TABLE OF CONTENTS

Page

LIST OF TABLES ix

LIST OF FIGURES x

CHAPTER

1 INTRODUCTION 1

1.1 Background 1

1.2 Dielectric constant and low-k materials 5

1.3 Post CMP plasma processing 7

1.4 Cu thermal stability 8

1.5 Brief description of the chapters 9

REFERENCES 13

2 DESCRIPTION OF THE SAMPLES, INSTRUMENTS AND CHARACTERIZATION MOTHODS 15

2.1 Introduction 15

2.2 The samples in this study 14

2.2.1 Low-k dielectric materials and CMP Cu 16

2.2.2 Cu adhesion and barrier layer 17

2.3 Remote plasma system and processing 18

2.3.1 Remote plasma system 18

2.3.2 Plasma discharge and processing 19

2.4 Electron beam evaporation 20

2.5 X-ray photoelectron spectroscopy 22

2.6 Fourier transform infrared spectroscopy 25

2.7 Atomic force microscopy 27

REFERENCES 29

3 REMOTE H_2/N_2 PLASMA PROCESS FOR SIMULTANEOUS PREPARATION OF LOW-K INTERLAYER DIELECTRIC AND INTERECONNECT COPPER SURFACE 30

3.1 Abstract 30

3.2 Introduction 31

3.3 Experiment 34

3.3.1 Low-k dielectric materials and CMP Cu 34

3.3.2 Remote plasma processing 36

3.3.3 Film characterization 37

3.4 Results and Discussion 38

3.4.1 ILD carbon abstraction during N_2/H_2 plasma processes 38

3.4.2 Structural changes related to Si-OH formation in LCHP ILD45

3.4.3 Effects of N_2/H_2 plasma processing on CMP Cu surfaces 48

3.5 Summary and conclusions 51

REFERENCES 54

4 CU FILM THERMAL STABILITY ON PLASMA CLEANED POLYCRYSTALLINE RU 57

4.1 Abstract 57

4.2 Introduction 57

CHAPTER Page

4.3 Experiment 60

4.4 Result and Discussion 63

4.4.1 Ruthenium oxide and surface processes 63

4.2.2 Cu thermal stability on Ru 70

4.5 Conclusion 77

REFERENCES 79

5 THERMAL STABILITY OF Ti, Pt AND Ru INTERFACIAL LAYERS BETWEEN SEEDLESS COPPER AND A TANTALUM DIFFUSION BARRIER 82

5.1 Abstract 82

5.2 Introduction 82

5.3 Experimental 84

5.4 Result and Discussion 87

5.4.1 XPS and AFM characterization 87

5.4.2. RBS analysis 91

5.4.3 Cu/Ti, Cu/Pt and Cu/Ru interdiffusion analysis 94

5.5 Conclusion 96

REFERENCES 98

6 SUMMARY AND FUTURE WORK 101

6.1 Summary 101

6.2 Future work 103

6.2.1 Plasma interaction at surface of ultra low-k ILD (k<2.2) 104

CHAPTER Page

6.2.2 Thermochemical stability of ultra-thin direct plate Cu barrier materials 104

REFERENCES 106

REFERENCES 107

LIST OF TABLES

Table Page

2.1 Dielectric constant, porosity, thickness and chemical concentrations for the high carbon low porosity (HCLP) and low carbon high porosity (LCHP) ILD films. The concentrations were determined from XPS and RBS as indicated. 17

3.1. Dielectric constant, porosity, thickness and chemical concentrations for the high carbon low porosity (HCLP) and low carbon high porosity (LCHP) ILD films. The concentrations were determined from XPS and RBS as indicated 35

5.1 The FWHM of each peak in the RBS spectra before annealing. 87

5.2 The XPS surface atomic ratio of the three films before and after 400 ℃ 88

LIST OF FIGURES

Figure Page

1.1 Cross-sectional 3D image of a 90 nm IBM microprocessor................ 3

1.2 Schematic of the Cu interconnect structure after CMP processes........ 4

1.3 Diagram of (a) network structure of SiCOH film; (b) porous cage network structure of SiCOH film. 6

1.4 (a) The schematic illustration of the Cu/low-k ILD surfaces after CMP process; (b) Ideal condition of Cu fill after thermal process; (c) Actual view of Cu fill after thermal process (de-wetting).. 8

2.1 Actual view and schematic illustration of the transfer line with integrated ultrahigh vacuum (UHV) systems.................................... 15

2.2 Schematic of the RF remote plasma system used in the study. 19

2.3 Schematic illustration of the electron beam source used for e-beam evaporation system. The electron emitter, crucible liner and deposition source are shown and the electron beam path is marked in red. 21

2.4 Schematic illustration of the photoemission process for XPS........... 22

2.5 Electrons average escape depth vs kinetic energy. 23

2.6 XPS scans of the two pristine low-k ILD materials. 25

2.7 The FTIR transmittance of the two pristine low-k ILD materials after base line correction with peak assignments. 27

3.1 Schematic of Cu interconnects and low-k ILD after CMP. The post-CMP plasma process is necessary to remove surface contamination on the Cu and ILD. 31

Figure Page

3.2 Schematic of the rf remote plasma system used in the study. 37

3.3 XPS and FTIR spectra characterize the surface and bulk atomic species of the 100 nm ILD, respectively. 39

3.4 Relative absorbance of the Si-CH_3 mode of 100 nm ILD after 5 min H_2/N_2 remote plasma processes. 40

3.5 Absorbance of Si-H (2270-2160 cm^{-1}) FTIR spectra of 100 nm LCHP film as a function of (N_2/H_2) plasma treatments. 41

3.6 Bonding changes of LCHP ILD after 30 min N_2 plasma treatment as displayed in (a) the C 1 s XPS spectrum; (b) the N 1 s XPS spectrum; and (c) the FTIR spectrum, which shows peaks associated with saturated aldehyde (1734 cm^{-1}) and saturated ketone (1716 cm^{-1}) configurations. 43

3.7 XPS spectrum before and after N_2 plasma treatment as displayed in (a) Si 2 p and (b) O 1 s. 44

3.8 Relative absorbance of the Si-C/Si-O ratio after different time of N_2 plasma pretreatment followed by 5 min H_2 plasma processes. 45

3.9 Changes of the FTIR Si-OH absorption band and dielectric constant after various RT and 380 ℃ plasma processes of the 500 nm LCHP film 47

3.10 Contact angle after various RT and 380 ℃ plasma processes of the 500 nm LCHP film. 48

Figure Page

3.11 XPS spectra of CMP Cu film before and after different thermal anneals. (a) O 1 s peak, (b) C 1 s peak. 49

3.12 (a) XPS spectrum of CMP Cu surfaces before and after various N_2 and H_2 plasma cleaning at 380 ℃; (b) integrated XPS peaks normalized to the as received sample for various plasma processes at RT and 380 ℃ 50

4.1 Schematic of the RF remote plasma chamber for surface processing and vacuum annealing 62

4.2 XPS scans of the Ru $3d_{3/2}$ and $3d_{5/2}$ core levels (a) of the as-received Ru sample showing the fitting to the oxygen related and bulk peaks; and (b) comparing the as-received surface before and after H_2 plasma processing (4 min).. 64

4.3 XPS scans of the O 1s core level of (a) the as-received Ru surface; (b) after H_2 plasma processing (1 min); (c) after H_2 plasma processing (4 min); and (d) relative oxygen concentration vs H_2 plasma exposure time. The dashed lines in (a) (b) and (c) show peak fittings: where the 531.2 eV feature (531.5 eV in (c)) was associated with grain boundary oxygen and the 529.8 eV feature was associated with surface oxide. 65

4.4 XPS scans of the O 1s core level of (a) as-received Ru after H-plasma processing and vacuum annealing, and the carbon-free Ru film followed by oxidation and H-plasma processing; and (b) the carbon-free Ru film following vacuum annealing.. 67

Figrure Page

4.5 XPS scans of the Ru 3d core level for 10 nm Cu on Ru, (a) prior to annealing; After annealing at 450 ℃ for Cu on processed Ru substrates; (b) 150 ℃ thermal anneal of Ru; (c) H_2 plasma processed; (d) as-received. 71

4.6 AFM images of 10 nm Cu coated on different Ru substrates, (a) Ru as-received, RMS = 7.0 nm; (b) Ru substrate with H_2 plasma processed, RMS = 1.0 nm; (c) Ru substrate with 150 ℃ thermal flash, RMS = 0.9 nm; (d) Prior to annealing, RMS = 0.5 nm. 72

4.7 Groove structure evolution and contact angle changes due to different surface energies configuration (a) initial stage of groove structure formation with contact angle θ_0; (b) critical continuity condition θ_C; (c) isolated Cu island formation when $\theta_D > \theta_C$. 74

4.8 XPS scans of the Ru 3d core level for 10 nm Cu films on oxidized as-received Ru substrates upon annealing as indicated. 75

4.9 Schematic of possible reaction paths for vacuum annealing Cu films on Ru oxidized and clean substrates. 76

5.1 A schematic of the multilayer structure with pertinent length scales. 86

5.2 XPS scans of (a) Ti 2p core levels for 10 nm Cu on Ti; (b) Pt 3d core levels for 10 nm Cu on Pt; (c) Ru 3d core levels for 10 nm Cu on Ru. Each frame shows scans before and after vacuum annealing at 400 ℃. 88

Figure Page

5.3 AFM images of 10 nm Cu on different adhesion layers, (a1) Ta/Ti/Cu as-deposited, RMS = 0.61 nm; (a2) Ta/Ti/Cu 400 ℃ annealing, RMS = 1.47 nm; (b1) Ta/Pt/Cu as-deposited, RMS = 0.95 nm; (b2) Ta/Pt/Cu 400 ℃ annealing, RMS = 0.55 nm; (c1) Ta/Ru/Cu as-deposited, RMS = 1.33 nm; (c2) Ta/Ru/Cu 400 ℃ annealing, RMS = 1.1 nm. 90

5.4 He^{2+} RBS spectra (2 MeV) obtained from an as-deposited and 400 ℃ annealed Cu/Ti/Ta multi-layer structure. 91

5.5 (a) 2 MeV; and (b) 4.3 MeV He^{2+} RBS spectra obtained from as-deposited and annealed Cu/Pt/Ta multi-layer structure. 93

5.6 He^{2+} RBS spectra (2 MeV) obtained from an as-deposited and annealed Cu/Ru/Ta multi-layer structure. 94

Chapter 1

INTRODUCTION

1.1 Background

Introduced in 1965, Moore's law indicates the numbers of transistors and resistors incorporated in a chip will approximately double every 18 months [1]. Over the last five decades, semiconductor industries have progressed through a continuous reduction of device dimensions and increase in device speed and density [2, 3]. Consequently, due to the rapid development of the technology, the interconnect metal lines have become narrower, and the interlayer dielectric thickness has decreased [4]. These changes have eventually resulted in resistance-capacitance (R-C) delay in signal propagation [5]. To solve the problem and meet the requirement of increased electronic device density, new metals for interconnect technology have been developed. As a result, alloyed Al with lower resistivity Cu was used to mitigate electromigration effects [6]. Gradually, the semiconductor industry was able to adopt low-resistivity Cu to replace conventional and alloyed Al [7, 8]. As for the interlay dielectric (ILD), the first Cu interconnect technology was based on SiO_2 as the ILD.

However, for the 90 nm technology node and beyond, SiO_2 ILD dielectrics have been replaced by lower dielectric constant materials (k less than 3.9) [9]. Fig. 1 [10] shows a cross sectional 3D image of a 90 nm IBM microprocessor containing several hundred million integrated devices and 10 levels of interconnect wiring. The interconnect processes are designated as bank-end-of-the-line (BEOL) technology. The introduction of the low dielectric constant

materials as the ILD alleviates R-C delay due to the metal/dielectrics interconnection.

In addition, low-k materials are required for low power consumption for ultra large scale integrated (ULSI) circuits [11]. Besides signal delay, power consumption is a major concern for interconnects. The increased frequency and higher densities in devices lead to a significant increase in power consumption. The power consumption is given by

$$P=\alpha C f V^2 \qquad (1.1)$$

where P is the power consumption, α is the wire conductivity, f is the frequency, V is the voltage for the power supply and C is the capacitance of the transistor [12]. Evidently, if the dielectric constant of the ILD is reduced, the energy consumption can be reduced.

Therefore, the International Technology Roadmap for Semiconductors (ITRS) projected that the insulator dielectric constant implemented at a given technology node should be 2.6-2.9 for 45 nm in 2011, 2.4-2.8 for 32 nm in 2012, and 1.9-2.2 for 19 nm in 2016 [13]. The fact that these dielectrics have already been implemented into current microchips is promising for the significance of these low-k materials.

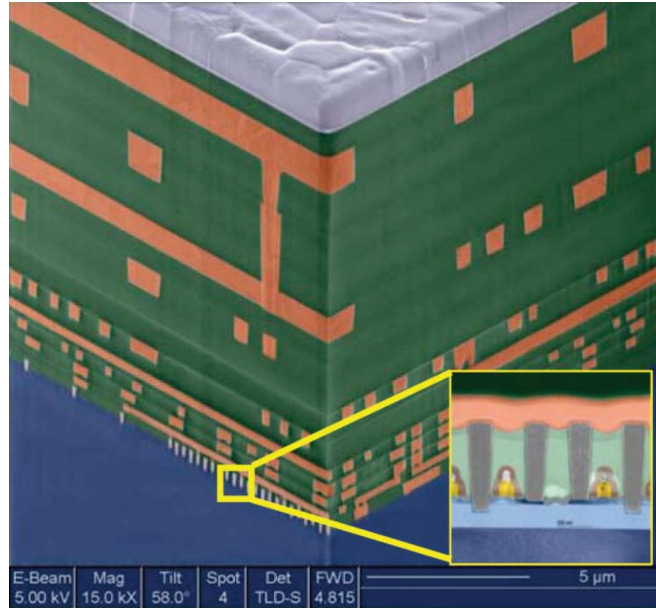

Fig. 1.1 Cross-sectional 3D image of a 90 nm IBM microprocessor [10].

Due to these changes in new interconnect technology development, the BEOL manufacturing has changed substantially. First, the Cu dual-damascene processing has been developed [14]. In the processing, both the vias and the trenches are patterned in the low-k dielectrics before depositing the metal. Second, while Al is a metal that can be directly plated onto SiO_2, it is not currently possible to directly plate Cu on SiO_2. Al has good adhesion to a SiO_2 surface and it resists diffusion into the wafer [15]. In contrast, Cu does not show strong interface bonding with SiO_2 and it also displays diffusion into Su. The Cu dual-damascene processing follows following steps. The Cu liner or barrier is first deposited by physical vapor deposition (PVD), chemical vapor deposition (CVD) or atomic layer deposition (ALD). The deposited barrier is then covered by a copper seed layer. The final step is to electroplate Cu onto the surface and over-fill the remaining structures [16]. The excess Cu in the field region is removed by

a chemical–chemical–mechanical polishing (CMP) process [17]. The result is that the planarized wires are embedded in a low-k dielectrics insulator. A post-CMP cleaning process is then required since various contaminants remain on the copper and exposed ILD surfaces (Fig 1.2) [18].

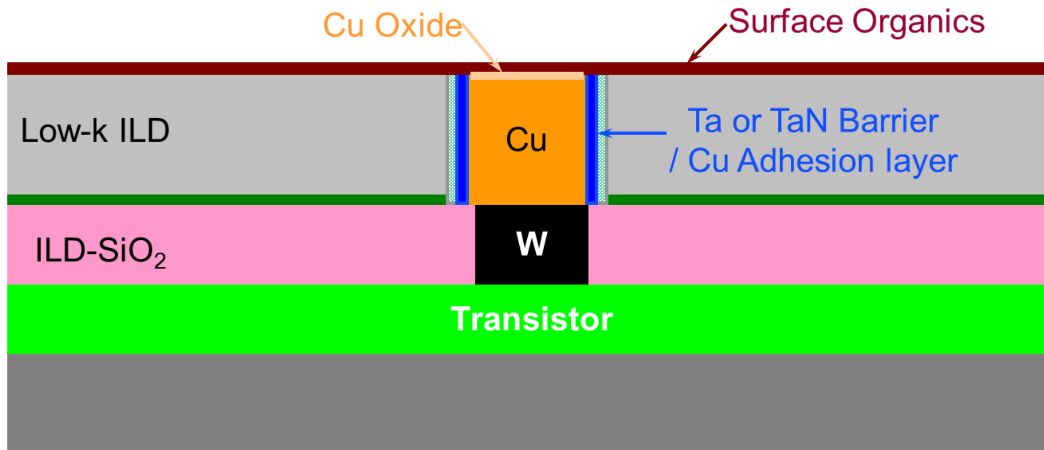

Fig. 1.2 Schematic of the Cu interconnect structure after CMP processes.

In addition, with continued device scaling, plasma dry etching/cleaning processes exhibit obvious technical advantages such as improved accuracy, stability and reproducibility [19]. Also, the plasma dry etching/cleaning technique has economic and environmental advantages. It is a relatively less costing, lower pollution and programmable processing approach compared with conventional wet etching/cleaning. However, incorporation of low-k materials as ILD layers brings about great challenges when various plasma-based processing and cleaning methods are applied to manufacturing of the Cu interconnect technology [20, 21].

Overall, the performance of Cu interconnect structure is currently limited by resistance (due to the surface oxide formed during the CMP processes) as well as adhesion and diffusion at the dielectric copper interface (due to poor adhesion

and significant diffusion to the dielectrics). Various plasma and gas treatments of the Cu surface after CMP have been demonstrated and utilized to remove the Cu-oxide as well as improve adhesion and electromigration performance of the interface between the Cu and capping layer [22]. Unfortunately, the low-k dielectrics, especially the porous low-k dielectrics that are now being implemented as the ILD in Cu interconnects, are susceptible to plasma damage, including pore collapse, carbon group abstraction, moisture uptake and the consequent increase of the dielectric constant [23-25]. In this thesis, a detailed study is performed to examine the combined impact of plasma treatments on the surfaces and interfaces of low-k ILD, Cu, and Cu adhesion.

1.2 Dielectric constant and low-k materials

The Clausius-Mosotti equation describes the relation of the dielectric constant of a material to the polarizability of the atoms or molecules. The Clausius-Mosotti's relation is represented by:

$$\frac{k-1}{k+2} = \frac{4\pi}{3}\sum N_i \alpha_i \qquad (1.2)$$

where k is the dielectric constant, α is polarizability of the atom or molecule, and N is the number of atom or molecules per unit volume [12]. This formula provides a guide to developing approaches to reduce the dielectric constant of a material. For SiO_2 based dielectrics, the dielectric constant value can be reduced by replacing Si-O bonds (polarizability/unit volume = 0.123 [26]) with lower polarizability bonds such as $Si\text{-}CH_3$ (polarizability/unit volume = 0.076 [26]). The dielectric constant value can be again reduced by decreasing the density of the

material. In this approach, porosity is introduced into the material to prepare lower dielectric constant films. Fig. 1.3 shows a schematic of the structure of two different low-k dielectrics materials [27].

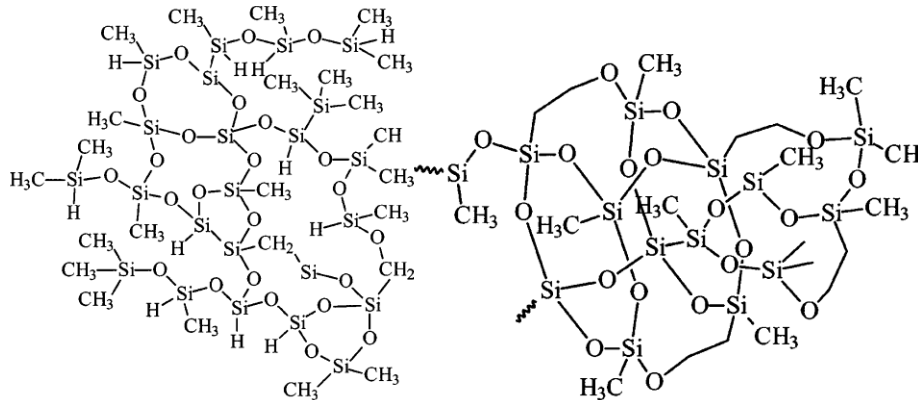

Fig. 1.3 Diagram of (a) network structure of SiCOH film; (b) porous cage network structure of SiCOH film [27].

The first commercial introduction of a low-k interlayer dielectric occurred around 2000. The process basically replaced SiO_2 with fluorosilicate glass for the 180 nm technology node [10]. Since that time, the dielectric constant has been further decreased by using ILDs with carbon groups. These ILDs are composed of hybridized carbons such as Si-CH_3 to replace the Si-O [28]. The deposition method of choice for this class of materials is plasma-enhanced chemical vapor deposition (PECVD) at various pressures, power and substrate temperature, and bias. The 32 nm technology node and below specifies the integration of dielectric materials with a k value within the range of 2.4-2.2 [12]. To further lower the dielectric constant for PECVD materials, porosity has been introduced into the films. This modification leads to a decrease of the film density, therefore reducing

the total number of polar molecules N per unit volume, as anticipated from equation 1.2 [26].

1.3 Post CMP plasma processing

As discussed above, the solution to upcoming generation of ULSI is the utilization of a multilevel metallization scheme where interconnections are made through trenches and vias in the different dielectric layers. For such a scheme to work, it is important that each level is flat to enable the lithographie and patterning processes. Several planarization techniques have been used for dielectric and metal surfaces. At present, the current technique that has proven capable of achieving the requisite planarity is chemical mechanical polishing (CMP).

Chemical mechanical polishing is a process that is used for planarization and consequent interconnect pattern formation. A schematic of the Cu interconnect structure after CMP process is shown in Fig. 1.4. Mechanical and chemical interactions with a patterned wafer surface introduce damage and contamination on both the ILD and Cu surfaces [18]. The polishing slurries are typically comprised of low density solids, such as fumed alumina or colloidal silica. These slurries contain additional chemicals such as nitric acid, peroxide or ammonium hydroxide based solutions [17]. A post-CMP process after Cu electroplating and CMP processes is required for removal of organic residuals remaining on the ILD surface, and also to reduce the Cu oxide [22]. Moreover, due to different removal rates, the triangle area, shown in Fig 1.4, contains surface oxide which leads to de-wetting phenomenon during thermal processing

afterwards [29]. An O_2 plasma is used for photoresist removal, however, a H_2-containing plasma is preferred for the post CMP plasma processing to remove hydrocarbon contamination while not simultaneously damaging the ILD.

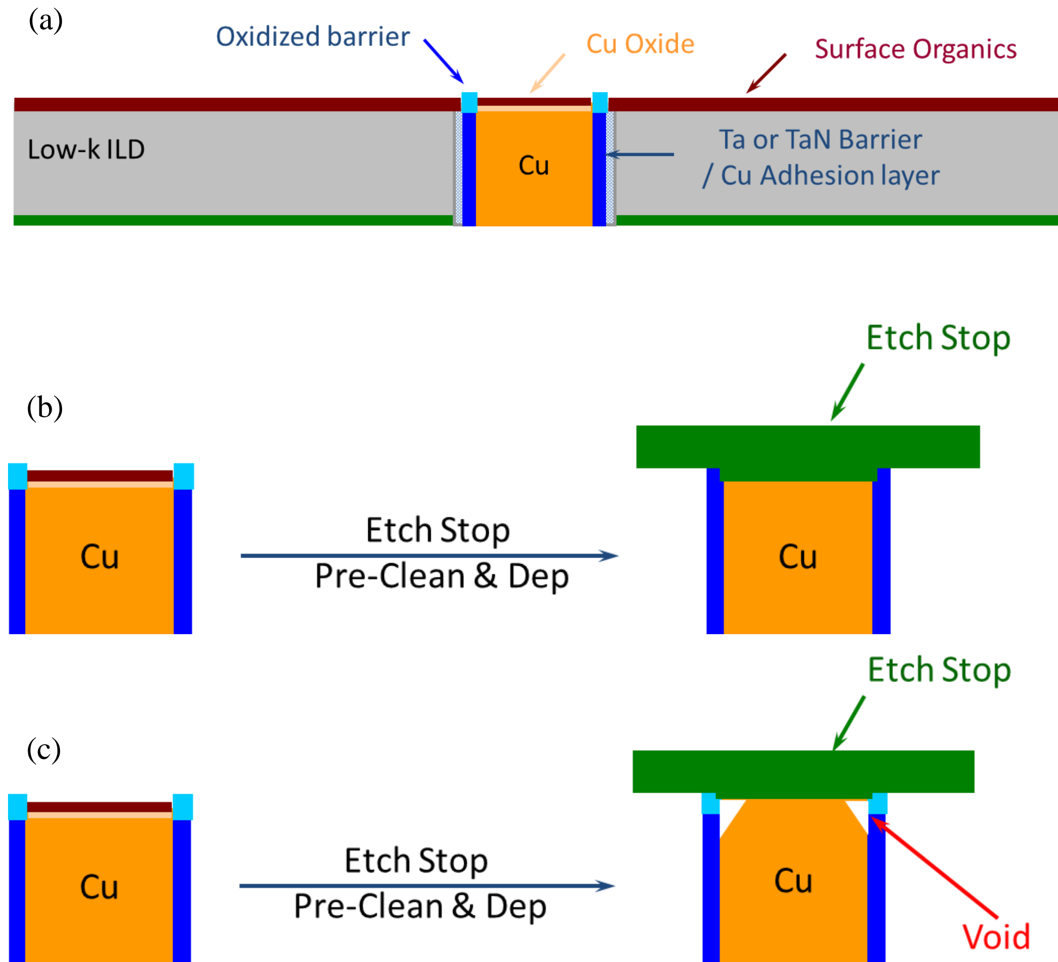

Fig 1.4 (a) Schematic illustration of the Cu/low-k ILD surfaces after CMP process; (b) Ideal condition of Cu fill after thermal process; (c) Indication of Cu de-wetting after thermal process.

1.4 Cu thermal stability

The enhanced atomic displacement and the accumulated effect of mass transport under the influence of an electric field (mainly, electric current) are called electromigration. For example, in the 45 nm technology node, the Cu

interconnect carry a typical current of 1 mA, which can be translated into a current density of ~10^6 A/cm^2. Such high current density can induce mass transport in the conducting lines in the device and lead to void formation and extrusion predominately in regions of poor adhesion. Electromigration in Cu lines occurs predominately by surface diffusion which has a lower activation energy than grain boundary diffusion [15]. Thus, adhesion and thermal stability between Cu and the adhesion/barrier layer become technical issues.

The reliability of interconnect structures with a multi-layer barrier structure is significantly determined by the stability of the bi-layer interfaces [11] due to the effect of Cu electromigration. The stability is essentially determined by interface interdiffusion and Cu film wettability on the underlying layer. In this thesis, I focus the research on these two determinants of Cu thermal stability.

1.5 Brief description of the Chapters

Cu interconnects and low-k dielectric materials have been introduced into the current and next generation of integrated circuit technology to reduce R-C delays and energy consumption. Incorporation of these new materials in new state-of-the-art manufacturing, brings new advantages, and new challenges. The background of Cu interconnects and low-k dielectrics have been described in Chapter 1. In this thesis, I focus on the plasma surface interactions at metal and interlayer dielectric (ILD) surfaces.

Chapter 2 describes the experimental facilities and characterization equipment used to analyze the results, including: a) the remote plasma surface processing system; b) the surface characterization equipment, x-ray photoelectron

spectroscopy (XPS), Fourier transform infrared spectroscopy (FTIR) and atomic force microscopy (AFM); (c) the *in-situ* metal thin film deposition system, electron beam evaporation.

Chapter 3 focuses on plasma induced modifications of low-k ILD dielectrics and contamination reduction of CMP Cu films which is motivated by the post-CMP processing. The scientific issue in this chapter is the determination of the surface reactions for N- and H- containing plasma processes with both ILD and CMP Cu surfaces. For the ILD films, the carbon concentration is substantially reduced in an H-containing plasma as indicated by FTIR analysis. The process results in an increase in the dielectric constant that can be attributed to moisture uptake in air and increased density due to structural relaxation. Moreover, elevated temperature (380 ℃) processing and an N_2 plasma pretreatment are investigated as approaches to minimize the low-k degradation. The elevated temperature enhances the stability of the low-k ILD layer by inhibiting the formation of polar Si-OH structures. The initial remote N_2 plasma plays a role in protecting the low-k ILD layer by forming a densified surface. For Cu surfaces, the elevated temperature N_2/H_2 remote plasma processes that minimize ILD damage results in efficient contamination removal from the CMP Cu surfaces.

In Chapter 4, both oxide stability/cleaning of Ru surfaces and the thermal stability of Cu on a Ru layer are presented. The scientific issue in this chapter is to understand the surface chemistry changes of Ru thin films due to plasma processing and the subsequent influences on Cu thermal stability on Ru substrates. In addition, the surface and interface energies have been proposed to explain the

experimental results. The presence of a ~2 monolayer native Ru oxide is determined by *in-situ* XPS which can be reduced after an H-plasma process while absorbed oxygen, presumably in the grain boundaries, remains after processing. The thermal stability or islanding of the Cu film on the Ru substrate is characterized by *in-situ* XPS. After plasma cleaning of the Ru adhesion layer, the deposited Cu exhibited full coverage. In contrast, for Cu deposition on the Ru native oxide substrate, Cu islanding was detected and was described in terms of grain boundary grooving and surface and interface energies.

In Chapter 5, the thermal stability of 7 nm Ti, Pt and Ru interfacial adhesion layers between a Cu film (10 nm) and a Ta barrier layer (4 nm) have been investigated. This chapter is an extension of the research of chapter 4. The scientific issue in this chapter is the interactions at the bi-layer interfaces for of the thin films upon thermal processing, including the interfaces of Ta/Si, adhesion (Ti, Pt and Ru) layer/Ta, and Cu/adhesion layer. The Ta RBS peaks remain unchanged after annealing, indicating negligible diffusion at the Ta/Si and adhesion/Ta interfaces. For Cu/Ti/Ta system, both the XPS and RBS spectra indicate that Ti has accumulated on the surface after 400 ℃ annealing. In the Cu/Pt/Ta system, Pt interdiffusion was detected from both XPS and RBS. Moreover, it appears Ti diffused into Cu to a greater extent than Pt diffused into Cu. The interdiffusion could be described by the Kirkendall effect. Ru as an adhesion layer has a stable interface with Cu after 400 ℃ annealing. All the surfaces were relatively smooth after annealing and no significant islanding or de-wetting was found. We proposed that a bilayer structure of 4 nm of Ta and 7 nm

of Ru will serve as a diffusion barrier and direct plate layer for Cu electrodeposition.

In Chapter 6, the results of this dissertation are summarized, and future research directions are proposed.

REFERENCES

1. Gorden E. Moore, Electronics, 38, 114 (1965).
2. M. R. Baklanov and K. Maex, Philosophical Transactions of the Royal Society A: Mathematical, Physical and Engineering Sciences 364, 201(2006).
3. M. T. Bohr, International Electron Devices Meeting, 241 (1995).
4. International Technology Roadmap for Semiconductors (ITRS).
5. S. P. Murarka and S. W. Hymes, Critical Reviews in Solid State and Materials Sciences 20, 87(2006).
6. I. Ames, F. M. d'Heurle, and R. Horstman, IBM J. Res. Dev. 4, 461(1970).
7. J. Paraszczak, D. Edelstein, S. Cohen, E. Babich and J. Hummel, International Electron Devices Meeting, 261(1993).
8. D. Edelstein, J. Heidenreich, R. Goldblatt, W. Cote, C. Uzoh, N. Lustig, et al. International Electron Devices Meeting, 773(1997).
9. D. Edelstein, H. Rathore, C. Davis, L. Clevenger, A. Cowley, T. Nogami, et al. Reliability Physics Symposium Proceedings, 316(2004).
10. W. Volksen, R. D. Miller, and G. Dubois, Chem. Rev. 110, 56(2010).
11. T. Homma, Mater. Sci. Eng. R 23, 243(1998).
12. K. Maex, M. R. Baklanov, D. Shamiryan, F. lacopi, S. H. Brongersma, and Z. S. Yanovitskaya, J. Appl. Phys. 93, 8793(2003).
13. International Technology Roadmap for Semiconductors, Semiconductor Industry Association, http://www.itrs.net/Links/2011ITRS/Home2011.htm (2010)
14. C-K Hu, J. M. E. Harper, Mater. Chem. Phys. 51, 5(1998).

15. K. N. Tu, J. Appl. Phys. 94, 5451 (2003).

16. D. Edelstein, J. Heidenreich, R. D. Goldblatt, W. Cote, C. Uzoh, N. Lustig, et al., International Electron Devices Meeting, 773(2000).

17. Y. Ein-Eli, D. Starosvetsky, Electrochimica Acta, 52, 1825 (2007).

18. J. Torres, J. Palleaua, F. Tardif, H. Bernard, A. Beverina, P. Motte, R. Pantel and M. Juhel, Microelectronic Engineering, 50, 425-431 (2000).

19. H. Abe, M. Yoneda, and N. Fujiwara, Jpn. J. Appl. Phys. 47, 1435(2008).

20. M. A. Goldman, D. B. Graves, G. A. Antonelli, S. P. Behera, and J. A. Kelber, J. Appl. Phys. 106, 013311 (2009).

21. X. Hua, M. Kuo, G. S. Oehrlein, P. Lazzeri, E. Iacob, M. Anderle, C. K. Inoki, T. S. Kuan, P. Jiang, and W. Wu, J. Vac. Sci. Technol. B, 24, 1238 (2006).

22. X. Liu, S. Gill, F. Tang, S. W. King, and R. J. Nemanich, J. Vac. Sci. Technol. B 30, 031212 (2012).

23. J. Lee and D. B. Graves, J. Phys. D: Appl. Phys. 43, 425201(2010).

24. P. Liu, T. Chang, Y. Mor and S. M. Sze, Jpn. J. Appl. Phys. 38, 3482 (1999).

25. Y. Kim, H. J. Kim, J. Y. Kim and Y. Lee J. Korean Phys Soc. 40, 94 (2002).

26. R. S. Smith, The effect of ultra-violet light curing on the molecular structure and fracture properties of an ultra low-k material, ProQuest, 2007.

27. A. Grill and D.A. Neumayer, J. Appl. Phys., 94, 6697 (2003).

28. A. Grill, V. Patel, K. L. Saenger, C. Jahnes, S. A. Cohen, A. G. Schrott, D. C. Edelstein and J .R. Paraszczak, Mater. Res. Soc. Symp. Proc. 443, 155(1997).

29. X. Liu, C. Zhu, B. S. Eller, T. Sun, C. J. Jezewski, S. W. King, and R. J. Nemanich, J. Vac. Sci. Technol. B 30, 052203 (2012).

Chapter 2

DESCRIPTION OF THE SAMPLES, INSTRUMENTS AND CHARACTERIZATION MOTHODS

2.1 Introduction

The experiments in this dissertation were mainly accomplished *in-situ* using an integrated ultrahigh vacuum (UHV) system, as shown in Fig. 2.1. The *in-situ* measurements were supported with other *ex-situ* characterization techniques. The materials used to study the plasma effects or thermal stability are discussed in this chapter. Also the details of the experimental methods and characterization are discussed individually.

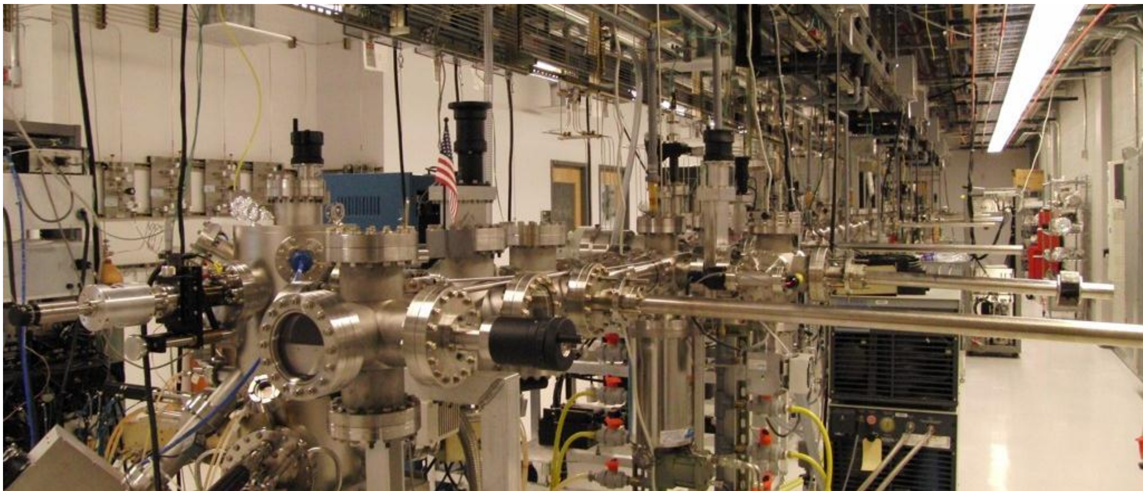

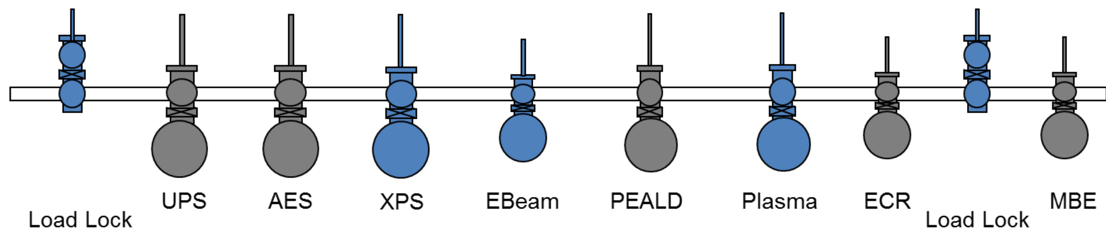

Fig. 2.1 Actual view and schematic illustration of the transfer line with integrated ultrahigh vacuum (UHV) systems.

The UHV system is maintained at ~5x10^{-10} Torr with multiple chambers interconnected through a ~20 m linear transfer line. The experiments in this study involve the following systems: remote H_2 plasma chamber for plasma processing and vacuum annealing, electron beam evaporation for metal layer deposition (including Cu, Ru, Ti, Pt and Ta), and XPS for core level analysis. After completing all *in-situ* measurements, the low-k samples were removed and analyzed with RBS for film stoichiometry, Capacitance-Voltage (C-V) measurement for dielectric constant and FTIR for bulk bonding information. The multiple-layer metal films were removed from UHV system and analyzed with RBS for film stoichiometry and interdiffusion and AFM for surface morphology.

2.2 The samples in this study

2.2.1 Low-k dielectric materials and CMP Cu

In chapter 2, the low-k dielectrics and CMP Cu surfaces are studied. This work investigates two different low-k films deposited on ~300 mm diameter Si (100) wafers by plasma-enhanced chemical vapor deposition (PECVD). The properties of the two ILD layers described as high carbon, low porosity (HCLP, k=2.55, porosity ~0) and low carbon, high porosity (LCHP, k=2.5, porosity 25%), are shown in Table 2.1.

material	k value	porosity	thickness	chemical concentrations
HCLP	2.55	0%	100±6 nm	Si (21.0%) C (40.7%) O (38.3%) XPS Si (13%) C (37%) O (23%) H (27%) RBS
LCHP	2.50	25%	100±5 nm	Si (26.8%) C (16.9%) O (56.3%) XPS Si (19%) C (23%) O (38%) H (21%) RBS

Table 2.1. Dielectric constant, porosity, thickness and chemical concentrations for the high carbon low porosity (HCLP) and low carbon high porosity (LCHP) ILD films. The concentrations were determined from XPS and RBS as indicated.

The Cu thin films utilized for these experiments were prepared as follows: a TaN adhesion layer was plated onto 300 mm diameter (100) Si substrates with 100 nm of thermal oxide. Then a Cu seed layer was sputter deposited onto the adhesion layer. The Cu film was finally electrochemically plated (ECP) on the seed layer. The surface was chemically mechanically polished using a Cu CMP process with a carbonate solution. The final Cu thickness was ~350 nm.

2.2.2 Cu adhesion and barrier layer

In chapter 4, the study was focused on the chemical stability of Ru oxide and thermally induced changes of Cu film wattability. The Ru film (provided by Intel) was deposited by atomic layer deposition (ALD) onto 300 mm diameter

(100) Si wafers which had a 100 nm thermal oxide (SiO_2). The films were ~8 nm thick. The Ru adhesion film is polycrystalline and X-ray diffraction (XRD) shows (100) and (101) peaks.

In chapter 5, the study was focused on the thermal stability of 7 nm Ti, Pt and Ru interfacial adhesion layers between Cu film (10 nm) and a Ta barrier layer (4 nm). The samples were grown on 25mm dia p-type, boron doped, (100) silicon wafers with a resistivity of 0.006-0.01 Ω·cm. The oxidized Si wafers were cleaned in an ultrasonic acetone bath for 15 min, an ultrasonic methanol bath for another 15 min, and dried with ultra-high purity nitrogen gas. Then the Si wafer is transferred into the UHV system. After a 5 min remote H_2 plasma cleaning, a 4 nm Ta barrier layer was deposited on the cleaned, oxidized Si wafer followed by a 7 nm adhesion layer (Ti, Pt and Ru respectively), and finally, the 10 nm Cu film was deposited.

2.3 Remote plasma system and processing

2.3.1 Remote plasma system

All plasma processing was carried out in a system shown schematically in Fig. 2.2 which is designed for application of various gases. The experimental chamber is maintained at a base pressure of $7x10^{-9}$ Torr. The sample is held at the center of the chamber facing the quartz plasma tube. Gases are delivered through the tube using mass flow controllers. The rf power (13.56 MHz) was coupled to the plasma by a 12 turn copper coil which encircled the ~32 mm diameter quartz tube. The plasma is generated in the quartz tube and excited molecules and radicals are transported through the chamber to the sample. The pressure is

controlled through a combination of the gas flow and a throttle valve in front of the turbo molecular pump. The typical plasma operating conditions are 30 W rf power, 60 millitorr pressure and 90 standard cubic centimeter per minute (sccm) gas flow. The samples are heated to constant temperature (calibrated with a Mikron-M90Q infrared pyrometer) with a tungsten irradiation filament heater behind the sample holder, and the substrate temperature is monitored with a thermocouple behind the center of the molybdenum plate. The sample temperature is controlled with a Eurotherm 808 system using the thermocouple output.

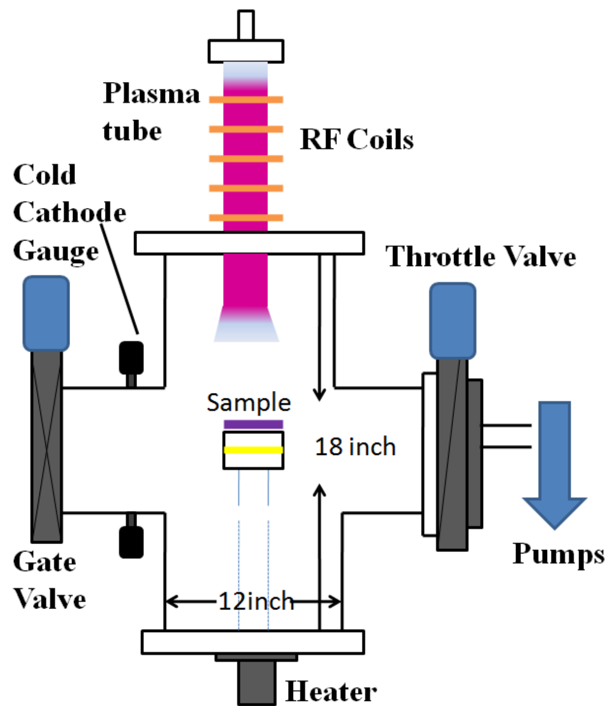

Fig 2.2 Schematic of the RF remote plasma system used in the study [1].

2.3.2 Plasma discharge and processing

The initial ionization and the sustainment of the plasma discharge can be deduced from electromagnetic theory [2]. The initial ionization is accomplished

by the electric field which is set up between the coils and the top flange of the chamber. Thus the gas molecule experience two forces. One is a pull in one direction on the positive charged nuclei and the other is in the opposite direction on the electron cloud. The combined effect of the two forces to remove an electron from the neutral atom which is accelerated by the rf field and after a breakdown event the plasma is established. It follows subsequently cascading ionization to an equilibrium discharge. Therefore, molecules are excited to higher energy states and also partially ionized. As the excited species are delivered onto the surface of the film, the reactions occur. This is the basic route for plasma processing.

As a reference, since H_2 gas plasma has been used through this study, the characteristics are described as follows. The previous research by Thomas Schneider [2] using a double Langmuir probe to determine the ion density. The results indicated a density of ~10^8 cm^{-3} and ~10^6 cm^{-3} at 15 and 300 mTorr respectively in the sample region. Based on the equipment geometry gas flow rate and processing pressure, there are ~5×10^5 H ions striking the surface every second. In addition, a catalytic probe system was used to determine the atomic H density is ~10^{11} cm^{-3} in the sample region which indicates a rate of ~5×10^9 /s arriving on the sample surface. Based on these numbers, the excited neutral radicals (i.e. atomic H) presumably play the most important role in the plasma processing. The detailed discussion will be in Chapter 3.

2.4 Electron beam evaporation

The e-beam metallization system employed a five pocket Thermionics e-GUN^{TM} evaporation source (model 100-0050, 3 kW) was installed in a chamber with a base pressure of 4×10^{-10} torr. The equipment is used for depositing metal thin films, including Ta, Ti, Ru, Pt and Cu. A typical electron gun including an electron emitter and metal source is shown in Fig. 2.3.

A current passing through the tungsten filament generates an electron beam by thermionic electron emission. The electron beam then is accelerated by an electric field and confined by a magnetic field to focus onto the center of the selected source. In the model 100-0050, there are totally five source pockets. The metal sources are put inside of the crucible liners sitting in the five pockets. While the electron beam position is fixed, a feedthrough with bellows is utilized to switch between the metal sources for deposition. To obtain a controlled deposition flux, the emission current is varied, from 50 mA to 250 mA, depending on the various metals. For each layer, a growth rate of 0.01 nm/s was maintained with a quartz crystal thickness rate meter (Sycon STM–100/MF).

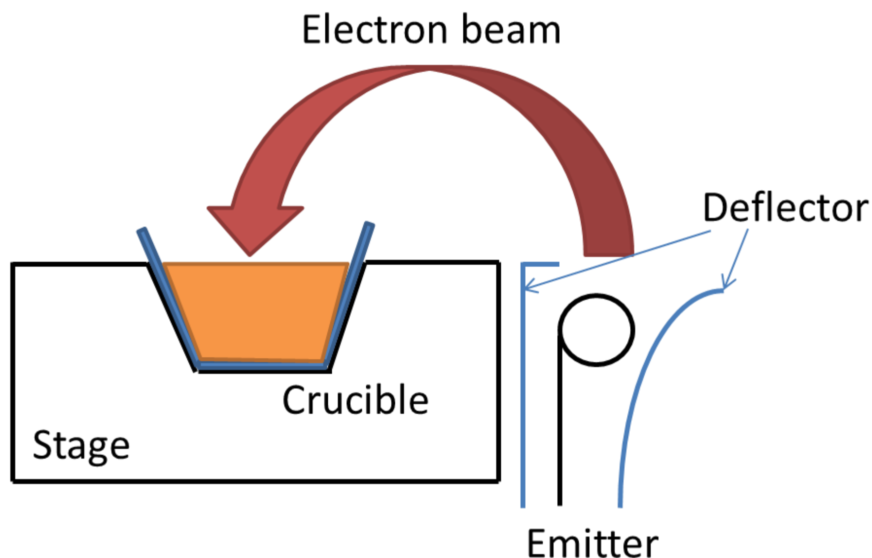

Fig. 2.3 Schematic illustration of the electron beam source used for e-beam evaporation system. The electron emitter, crucible liner and deposition source are shown and the electron beam path is marked in red.

2.5 X-ray photoelectron spectroscopy

The XPS system is employed in this dissertation for chemical composition identification of the film surfaces. The photo electrons are excited by x-ray and collected by an electron spectrometer. The schematic of the photoemission process is shown in Fig. 2.4. The spectrometer records the counts of electrons versus kinetic energies, typically from 0 ~ 1keV. The kinetic energy (KE) is usually converted to binding energy (BE) by the following the relation: $BE = h\nu - KE - W$, where $h\nu$ is the energy of the photon and W is the work function of the spectrometer. The binding energy is referenced to Fermi level which is defined as the zero binding energy.

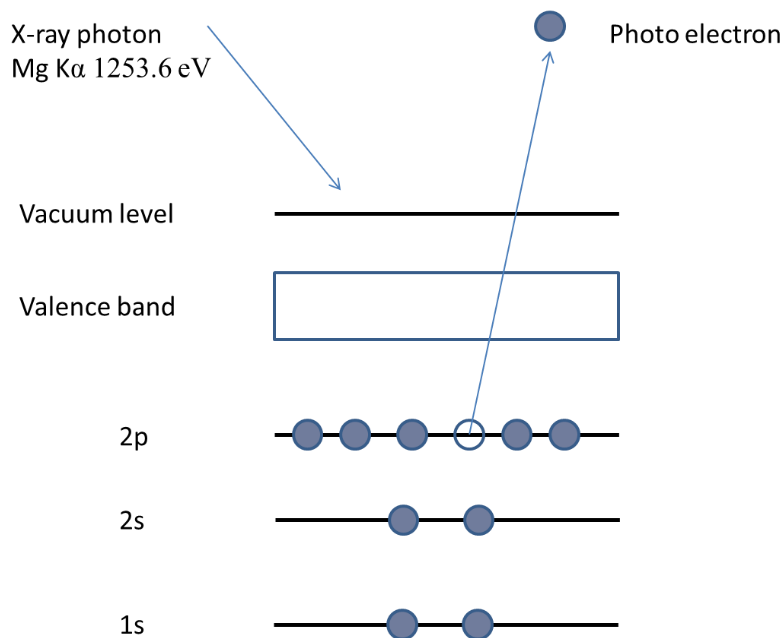

Fig. 2.4 Schematic illustration of the photoemission process for XPS.

The XPS is a surface technique because most of the electrons which are excited in the deep region of the sample are not emitted due to scattering and recombination. Only excited electrons near surface can escape from the sample. The dependence of the average electron escape depth versus kinetic energy is plotted in Fig. 2.5. The electrons generated near the sample surface will be emitted into the vacuum if they have sufficient kinetic energy to overcome the work function of the material. Many scattered electrons are also emitted, but these electrons show up as secondaries in the spectrum and cannot be used to describe the valence band electronic states. The photoelectrons are retarded to a constant energy (pass energy) as they reach the analyzer. The electrons from near the surface are emitted without energy loss.

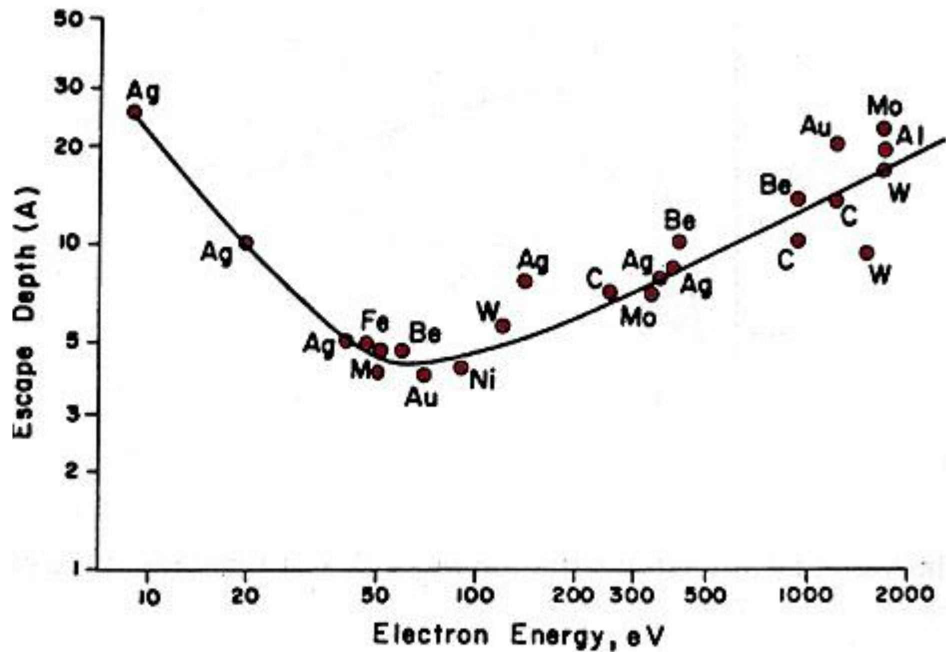

Fig 2.5 Electrons average escape depth vs kinetic energy [3].

The XPS is performed at a base pressure of 5×10^{-10} Torr using a VG Clam II spectrometer operated with a Mg Kα x-ray source (hν=1253.6 eV). The pass energy was kept at 20 eV. The XPS spectrum of Au 4f peaks was used for calibration done by previous work. A correction of the binding energy by + 0.1 eV was determined [4]. Also a full width at half maximum (FWHW) of 1.0 eV which can be treated as a resolution parameter of the XPS was determined. Typical survey scans (0-600 eV) of XPS spectra for low-k SiCOH samples studied in this thesis are shown in Fig 2.6. By collecting the high-resolution spectra for specific core levels, the changes of both binding energy and intensity are used for data analysis.

In chapter 3, the low-k ILD materials have been measured by XPS. During this process, insulating samples are subjected to charging effects because of their insulating nature. Shifting of spectra on the energy scale which leads to

difficulties in interpreting chemical states was observed. Essentially, the positive charges during the photo emission process results in positive surface charge accumulation. Therefore, sample surface acquires a positive potential and the kinetic energies of the photoelectrons are decreased by the electric field. The observed binding energy shifts in chapter 2 have been corrected based on the Si 2p peak at 103.3 eV for Si-O bonding.

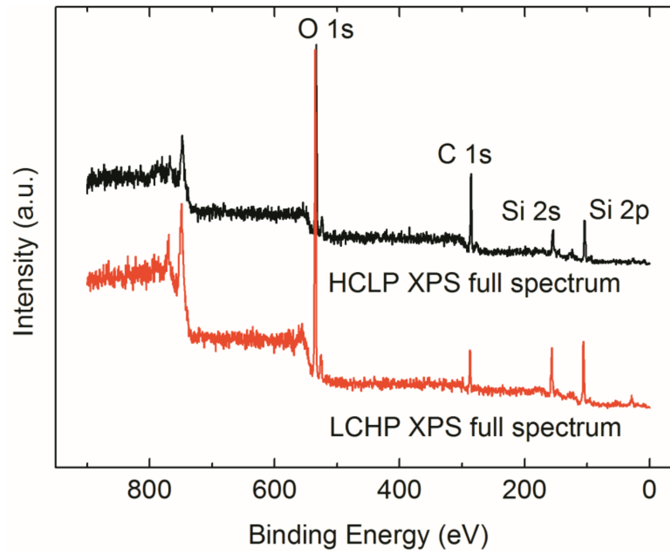

Fig. 2.6 XPS scans of the two pristine low-k ILD materials. [1].

2.6 Fourier transform infrared spectroscopy

FTIR is a technique for materials analysis where the infrared region of the electromagnetic spectrum is used. In this study, the FTIR was employed to measure the bulk bonding of the low-k ILD materials. The infrared light is transmitted through the sample and the characteristic wavelengths are absorbed corresponding to the specific bonds that are present in the materials. In this study, a Bruker IFS 66V/S FTIR was employed to carry out the measurements. The mid IR (5000-500 cm^{-1}) light source was selected, and KBr was used as a beam

splitter with a MCT detector. In this thesis, all the spectra are collected in transmittance mode and converted to absorbance. Spectra were recorded between 500-5500 cm^{-1} with 4 cm^{-1} resolution and 64 scans. To characterize the low-k dielectrics material bulk bonding properties, a background spectrum of a bare Si substrate is collected as a reference spectrum. The default software, OPUS, was used for data manipulation, including transmittance-absorbance conversion and base line correction.

Typical FTIR spectra of absorbance of ILD film after baseline correction are presented in Fig 2.7. In IR spectroscopy, the absorbance of a material is a logarithmic ratio of the radiation falling upon a material, to the radiation transmitted through a material which is given by:

$$A_{\lambda} = \log_{10}(I_{Out} / I_{Incident}) \quad (2.1)$$

where I_{Out} is the intensity of the radiation (light) that has passed through the material (transmitted), and $I_{Incident}$ is the intensity of the radiation before it passes through the material (incident). Moreover, the absorbance at different characteristic wavelength is associated with the absorption of specific bonds. Therefore, the difference between the two is attributed to the absorption of the target film. Also, the quantitative relationship between the bond concentration and absorbance intensity are widely used to study the low-k materials [5-8].

In Chapter 3, a quantitative analysis was carried out based on the FTIR spectra. The relative bond concentrations after plasma processing were determined from the FTIR absorbance spectra. After the baseline correction and wavenumber selection, the target peak associated with specific bonds was plotted.

Integrated absorption peak areas were normalized relative to that of the Si-O absorption band to avoid effects of possible thickness changes. The integrated absorption peaks were then normalized to those from the pristine film in order to determine the $Si\text{-}CH_3$ concentration (~1273 cm^{-1}) and the silanol group formation (3000 cm^{-1}-3800 cm^{-1}).

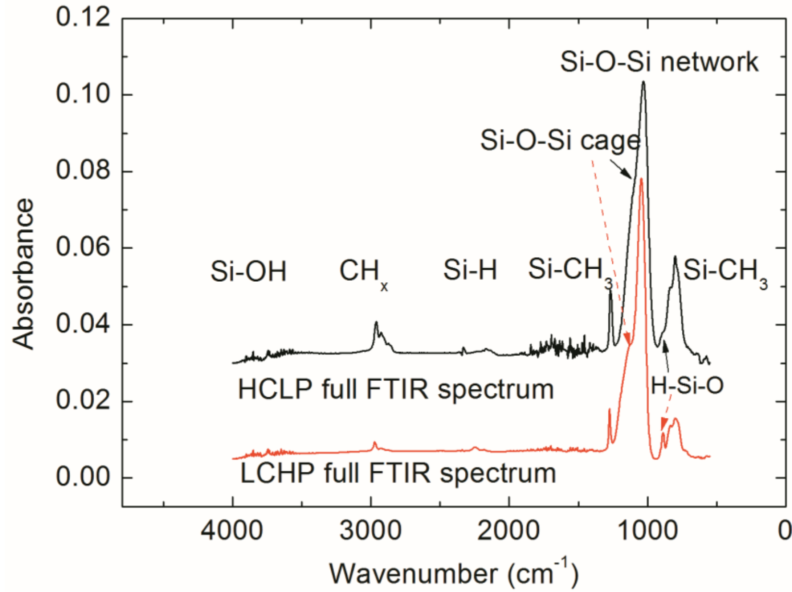

Fig. 2.7 The FTIR transmittance of the two pristine low-k ILD materials after base line correction with peak assignments. [1].

2.7 Atomic force microscopy

An Agilent™ AFM (model 5500) is used to monitor the surface morphology of the metal films before and after annealing in Chapter 4 and Chapter 5. All measurements were performed in contact mode using a silicon probe over an area of 5 μm × 5 μm. The AFM employs a scanning tip attached to the end of the cantilever across the sample surface and monitors the charges in the deflection by a photodiode detector. A piezoelectric scanner controls the

movement of the tip and the distance between tip and sample. The force between the tip and the sample is kept a constant. A laser beam is reflected from the backside of the cantilever to the photodiode detector which records the deflection of the cantilever as it moves across the sample. The data processor and feedback electronics convert the signals and generate an image of the sample surface. In ambient condition, the resolution in the X and Y directions is 1-10 nm while in vacuum it can reach 1-4 nm [9].

REFERENCES

1. Xin Liu, Sandeep Gill, Fu Tang, Sean W. King, and Robert J. Nemanich, J. Vac. Sci. Technol. B 30, 031212 (2012).
2. Thomas P. Schneider, Ph.D. thesis, Hydrogen Plasma Interaction with Silicon Surfaces, North Carolina State University (1994).
3. C. B. Drake. J. Vac. Sci. Technol. 13, 761 (1976).
4. Chiyu Zhu, Ph.D. thesis, Electronic States of High-k Oxides in Gate Stack Structures, Arizona State University (2012).
5. A. Grill and D. A. Neumayer, J. Appl. Phys., 94, 6697 (2003).
6. M. A. Goldman, D. B. Graves, G. A. Antonelli, S. P. Behera, and J. A. Kelber, J. Appl. Phys. 106, 013311 (2009).
7. J. Lee and D. B. Graves, J. Phys. D: Appl. Phys. 43, 425201(2010).
8. M. Fukasawa, T. Tatsumi, K. Oshima, and K. Nagahata, J. Vac. Sci. Technol. A, 26, 870 (2008).
9. Yang Sun, Ph.D. thesis, Ferroelectric Lithium Niobate Surfaces for Depositions of Metallic Nanostructure and ZnO Semiconducting Thin Film, Arizona State University (2011).

Chapter 3

REMOTE H_2/N_2 PLASMA PROCESS FOR SIMULTANEOUS PREPARATION OF LOW-K INTERLAYER DIELECTRIC AND INTERECONNECT COPPER SURFACE

3.1 Abstract

This study focuses on the simultaneous plasma treatment of interlayer dielectric (ILD) and chemical mechanical polished (CMP) Cu surfaces using N2/H2 plasma processes. The modifications induced by the gas chemistries are investigated for two ILD films with different porosities and carbon concentrations. H atoms and radicals in the plasma react with the carbon groups leading to carbon removal for both of the ILD films. Fourier transfer infrared (FTIR) spectra show a greater fractional reduction of CH_3 in the high porosity ILD compared to the low porosity ILD. Results indicate that an N_2 plasma forms an amide-like layer on the surface which apparently leads to reduced carbon abstraction from an H plasma process. In addition, FTIR spectra indicate the formation of hydroxyl (Si-OH) groups following the plasma exposure. Increased temperature (380 ℃) processing leads to a reduction of the hydroxyl group formation compared to ambient temperature processes, and the dielectric constant is increased by a smaller amount. It appears that the increase of the dielectric constant is mainly attributed to moisture uptake rather than network topography change due to carbon loss. The plasma experiments were repeated with CMP Cu surfaces at both ambient temperature and 380 ℃. The carbonate contamination was removed by an H_2

plasma process at elevated temperature while the C-C and C-H contamination was removed by an N_2 plasma process at elevated temperature.

3.2 Introduction

Low dielectric constant (low-k) materials as an interlayer dielectric (ILD) with copper interconnects display significant advantages for the reduction of RC time delays and energy consumption for future generations of silicon integrated circuit technology. The low-k materials incorporate low polarizability Si-C bonds replacing Si-O bonds, consequently reducing the dielectric constant from 3.9 to 2.5, and the high conductivity of Cu interconnects reduces the ohmic resistance compared to Al or other interconnect metals. The technological motivation of this study is to simultaneously clean low-k ILD and chemical mechanically polished (CMP) Cu surfaces using a remote plasma process which minimizes the damage to the low-k materials. As shown schematically in Fig. 3.1, after CMP processes, organic contamination and Cu surface oxide accumulate on the surface. A post CMP cleaning step is required before the capping layer deposition to enable adhesion to the ILD and Cu surfaces and to achieve low resistance Cu interconnects.

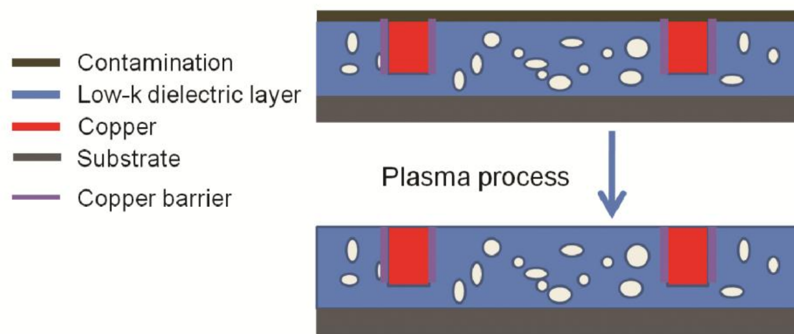

Fig. 3.1 Schematic of Cu interconnects and low-k ILD after CMP. The post-CMP plasma process is necessary to remove surface contamination on the Cu and ILD.

For the 32 nm technology node and beyond, the International Technology Roadmap for Semiconductors requires integration of dielectric materials with dielectric constant within 2.1-2.4 [1]. To fulfill this target, dielectric materials have been produced with a porosity of ~30% [2, 3]. However, the integration of porous, low-k materials presents challenges because of their enhanced reactivity to different technological processes such as ash etching, CMP, and plasma cleaning [4, 5]. Thus, understanding the complex interactions in plasma surface processes applied to porous low-k material is necessary to design future interconnect technologies.

Based on the success of oxygen plasma cleaning of Si surfaces and O_2 plasma dry etching, this approach has been considered for cleaning dielectric surfaces. However, the exposure of a carbon containing ILD film to an O_2 plasma environment leads to significant chemical and structural modifications [6, 7]. Goldman *et al.* [6] reported that plasma generated O radicals penetrate into the film and induce the removal of carbon containing groups. This carbon removal process also changes the porous surfaces from hydrophobic to hydrophilic which enhance the uptake of ambient moisture leading to a further increase in the dielectric constant. In addition, the porosity of the material may be changed through a transformation from a cage structure to a network structure. Recently, carbon abstraction induced by UV light exposure with an O_2 gas flow has been

reported by Lee *et al.* [8], which indicates that plasma generated photons contribute to the removal of the carbon groups.

To avoid these significant oxidation effects, H_2 plasma processes have been proposed for cleaning ILD layers [9, 10]. However, results have established that H radicals react with carbon groups and form volatile CH_4. Formation of high polarizability components, such as Si-OH is a consequence of moisture absorption after H_2 plasma treatment. These changes lead to a significant increase of the dielectric constant [11, 12], even though there is no additional oxygen incorporation during the plasma process. The absorption of water and the incorporation of hydrophilic OH groups lead to a much greater increase in k due to the high polarizability of OH groups [13] compared to the change due to the carbon abstraction induced network change.

One approach to minimizing the degradation of the dielectric constant is to produce a densified surface that confines the radicals at the local surface and limits further diffusion into the ILD layer. Results have shown that UV light curing leads to bond rearrangement that converts the Si-O-Si bond topography from cage to network resulting in a densified surface layer [14]. Other studies have established that noble gas bombardment (Ar^+ ions with bias) results in densification of the outer surface of the ILD film through energy transfer from kinetic collisions and excited molecules [6].

With the limitations of O_2 and H_2 processes, researchers have employed N containing plasma processes with N_2 or NH_3 to passivate ILD surfaces [15, 16]. It has been proposed that activated molecular species ($N2^*$) or radicals (N^*) react

with carbon groups near the surface, forming C-N bonds which leads to a densified layer [16].

Chemical mechanical polishing is a process that is used for planarization and consequent interconnect pattern formation. Mechanical and chemical interactions with a patterned wafer surface introduce damage and contamination on both the ILD and Cu surfaces [17]. The polishing slurries are typically comprised of low density solids, such as fumed alumina or colloidal silica. These slurries contain additional chemicals such as nitric acid, peroxide or ammonium hydroxide based solutions [18]. More recently, carbonate based solutions (such as K_2CO_3) have been employed [19] for copper CMP where a contamination layer containing carbonates and hydroxide copper-species, CuCO3•$Cu(OH)_2$, was reported [20]. The post-CMP process after Cu electroplating and CMP processes is required for removal of organic residuals remaining on the ILD surface, and also to reduce the Cu oxide.

In this study we employ a range of N_2 and H_2 mixed plasma processes applied to ILD and CMP Cu surfaces individually. The properties of the low-k ILD film are characterized, and the chemical interactions at the CMP Cu surfaces are studied as a function of plasma chemistry and substrate temperature. The mechanisms that lead to a clean Cu surface are explored while minimizing variations in two different ILD materials.

3.3 Experiment

3.3.1 Low-k dielectric materials and CMP Cu

This work investigates two different low-k films deposited on ~300 mm diameter Si wafers by plasma-enhanced chemical vapor deposition (PECVD). The properties of the two ILD layers described as high carbon, low porosity (HCLP, k=2.55, porosity ~0) and low carbon, high porosity (LCHP, k=2.5, porosity 25%), are shown in Table 1. The surface atomic concentrations were determined from XPS spectra where the integrated peak areas were normalized using the XPS sensitivity factors. The film concentrations were also obtained with Rutherford backscattering spectroscopy (RBS). The RBS C: Si ratio is ~2.8 for HCLP and ~1.2 for LCHP which follows the same trend for the respective XPS ratios of ~1.9 for HCLP and ~0.6 for LCHP. The experiments in this study employed ~100 nm thick LCHP and HCLP as well as 500 nm thick LCHP films.

material	**k value**	**porosity**	**thickness**	**chemical concentrations**
HCLP	2.55	0%	100±6 nm	Si (21.0%) C (40.7%) O (38.3%) XPS
				Si (13%) C (37%) O (23%) H (27%) RBS
LCHP	2.50	25%	100±5 nm	Si (26.8%) C (16.9%) O (56.3%) XPS
				Si (19%) C (23%) O (38%) H (21%) RBS

TABLE 3.1 Dielectric constant, porosity, thickness, and chemical concentrations for the high carbon low porosity (HCLP) and low carbon high porosity (LCHP)

ILD films. The concentrations were determined from XPS and RBS as indicated.

The Cu thin films utilized for these experiments were prepared as follows: a TaN adhesion layer was plated onto 300 mm diameter (100) Si substrates with 100 nm of thermal oxide. Then a Cu seed layer was sputter deposited onto the adhesion layer. The Cu film was finally electrochemically plated (ECP) on the seed layer. The surface was chemically mechanically polished using a Cu CMP process with a carbonate solution. The final Cu thickness was ~350 nm.

3.3.2 Remote plasma processing

The wafers are were diced into ~ 1.5 x 1.5 cm^2 sections and mounted onto a molybdenum plate using tantalum wires. The samples are transferred into vacuum through a UHV transfer line. All plasma processing was carried out in a system shown schematically in Fig. 3.2 which is designed for application of various gases. The experimental chamber is maintained at a base pressure of $7x10^{-9}$ Torr. The sample is held at the center of the chamber facing the quartz plasma tube. Gases are delivered through the tube using mass flow controllers. The rf power (13.56 MHz) was coupled to the plasma by a 12 turn copper coil which encircled the ~32 mm diameter quartz tube. The plasma is generated in the quartz tube and excited molecules and radicals are transported through the chamber to the sample. The pressure is controlled through a combination of the gas flow and a throttle valve in front of the turbo molecular pump. The typical plasma operating conditions are 30 W rf power, 60 millitorr pressure and 90 standard cubic centimeter per minute (sccm) gas flow. The samples are heated to constant temperature (calibrated with a Mikron-M90Q infrared pyrometer) with a

tungsten irradiation filament heater behind the sample holder, and the substrate temperature is monitored with a thermocouple behind the center of the molybdenum plate. The sample temperature is established with a Eurotherm 808 system using the thermocouple output.

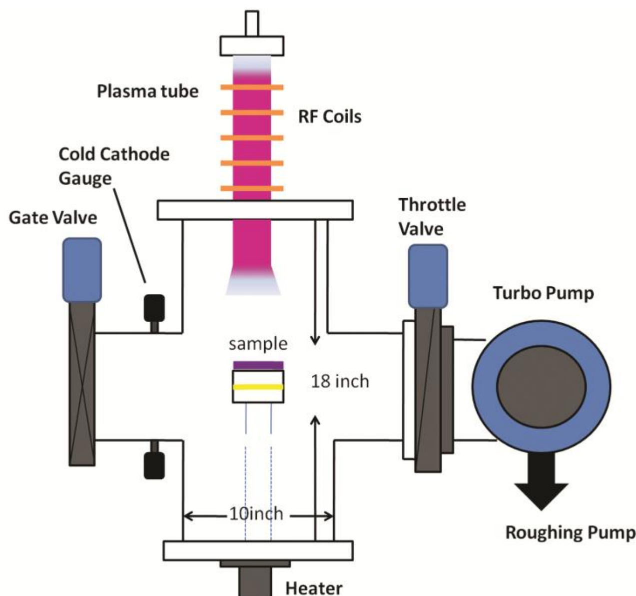

Fig. 3.2 Schematic of the rf remote plasma system used in the study.

3.3.3 Film characterization

After each plasma process, *in-situ* XPS analysis of the ILD and CMP Cu surfaces was carried out via UHV transfer from the remote plasma system to the XPS chamber. The spectra were collected using a VG Clam II spectrometer operating with a Mg Kα x-ray source (hv=1253.6 eV). The XPS spectra were shifted by ~6 eV due to charging effects. The observed charging shifts have been corrected based on the Si 2p peak at 103.3 eV for Si-O bonding. After removing the ILD samples from vacuum, FTIR was measured in transmission mode using a Bruker IFS 66V/S. Spectra were recorded between 500-5500 cm^{-1} with 4 cm^{-1}

resolution and 64 scans. The relative bond concentrations after plasma processing were determined from the FTIR absorbance spectra. Integrated absorption peak areas were normalized relative to that of the Si-O absorption band to avoid effects of possible thickness changes. The integrated absorption peaks were then normalized to those from the pristine film in order to determine the Si-CH3 concentration (~1273 cm^{-1}) and the silanol group formation (3000 cm^{-1}-3800 cm^{-1}). The dielectric constant of each film was determined before and after the different plasma treatments using capacitance-voltage (C-V) measurements at 1 MHz. The experiments were carried out using a mercury probe station system (MSI Electronics Mercury Probe Hg412-3). Water contact angles were measured using a Kruss Easy Drop system, and the angles were determined from the default software. All values were determined from the average of multiple measurements and the uncertainty was determined from the standard deviation.

3.4 Results and Discussion

3.4.1 ILD carbon abstraction during N_2/H_2 plasma processes

The XPS and FTIR of the pristine film before plasma treatment are displayed in Fig. 3.3 The different carbon concentration of the two 100 nm ILD are reflected in the respective XPS scans and FTIR spectra. The FTIR absorption has been normalized to the Si-O peak of the two scans such that the spectra are displayed as full scale. In this study FTIR absorbance and XPS spectra were employed to characterize the bulk and surface bonding concentrations and configurations, respectively.

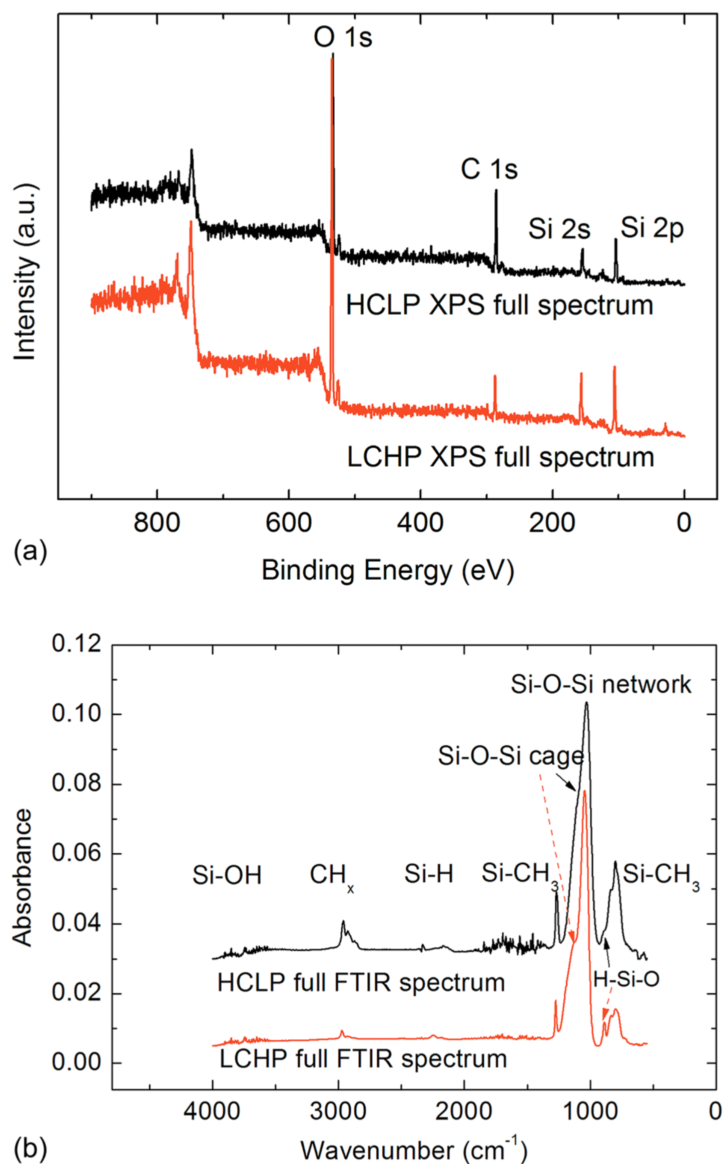

Fig. 3.3 XPS and FTIR spectra characterize the surface and bulk atomic species of the 100 nm ILD, respectively.

The Si-CH_3 (~1273 cm^{-1}) in the FTIR spectrum is typically used to determine the concentration of the methylated groups. The relative concentration of methylated groups removed from the film can be characterized by the relative reduction of the Si-CH_3 mode absorbance. The relative Si-CH_3 (1273 cm^{-1}) mode absorbance versus the percentage of H_2 in the plasma mixture is displayed in Fig.

3.4. The results indicate a greater fractional reduction of CH3 in the LCHP ILD compared to the HCLP ILD. For both ILD layers the fractional reduction of CH_3 remains essentially constant as the hydrogen content increases. These results establish that hydrogen induced carbon abstraction in the high carbon (low porosity) film is lower than the low carbon high porosity film which indicates that porosity is more significant for these films. Moreover, according to Goldman *et al*. [6], for oxygen induced carbon abstraction, oxygen radical diffusion through the pores is an essential factor attributed to carbon abstraction. Meanwhile, the N_2 in the plasma has a limited effect on the carbon abstraction.

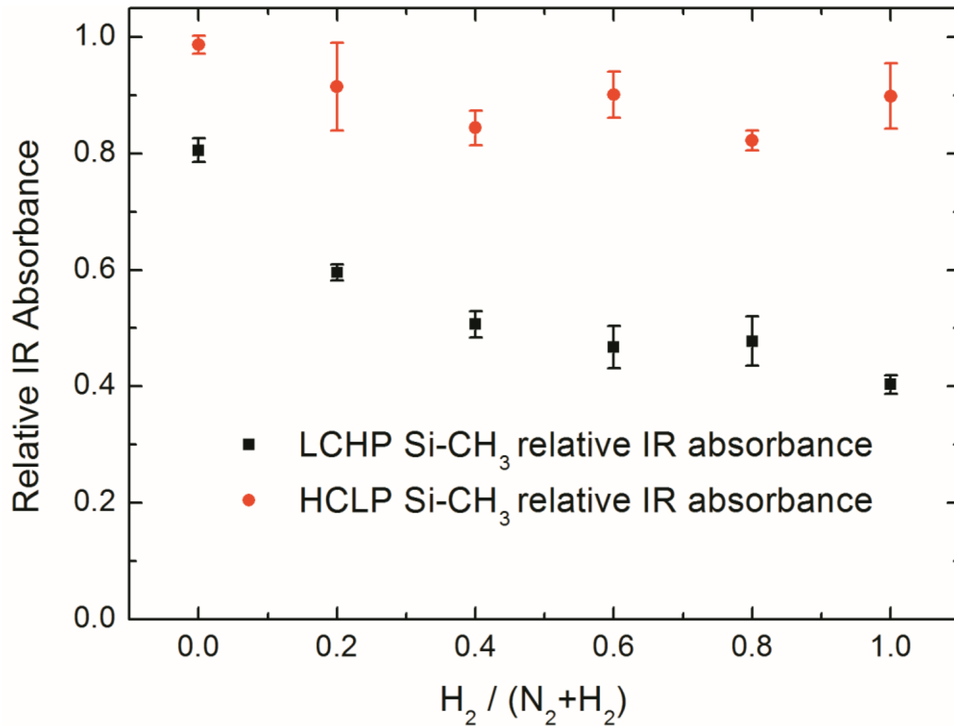

Fig 3.4 Relative absorbance of the Si-CH_3 mode of 100 nm ILD after 5 min H_2/N_2 remote plasma processes.

The replacement reaction of CH_3 groups by H atoms may occur as follows:

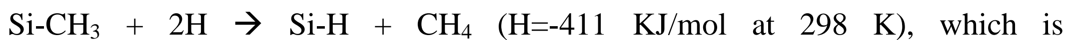
Si-CH_3 + 2H → Si-H + CH_4 (H=-411 KJ/mol at 298 K), which is

thermodynamically favorable [21]. It is likely that this is a two step process: the first step is abstraction ($Si\text{-}CH_3 + H \rightarrow -Si + CH_4$) [22, 23] resulting in the formation of a Si- dangling bond which is followed by absorption of H to form Si-H [24]. To explore this possibility, the Si-H (2270-2160 cm^{-1}) absorbance before and after processing of the LCHP films is shown in Fig 3.5. The Si-H (2270-2160 cm^{-1}) FTIR absorbance decreases as the H2 plasma concentration increases, however the Si-OH absorption increases substantially. The Si-H structures are not stable in air, and ambient moisture reacts at the Si-H sites to form Si-OH.

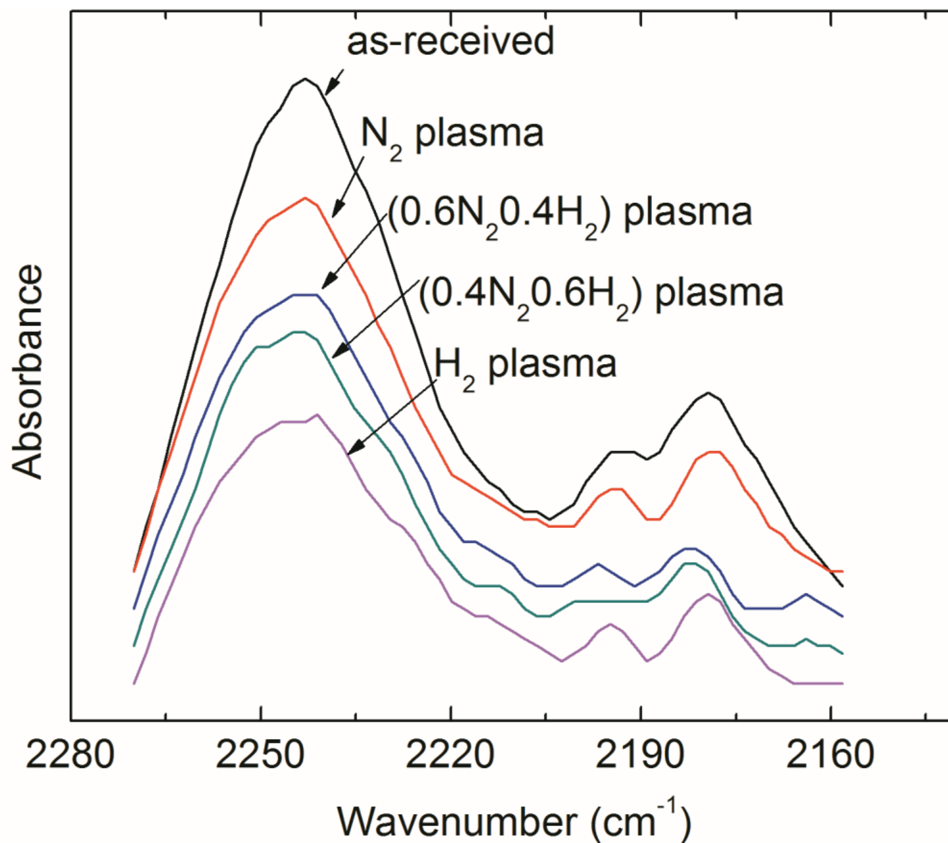

Fig. 3.5 Absorbance of Si-H (2270-2160 cm^{-1}) FTIR spectra of 100 nm LCHP film as a function of (N_2/H_2) plasma treatments.

It has been noted that the mixed plasma may generate additional active species [16] such as NH2, NH3, NH4, and N2H which could contribute to the following reactions [22]:

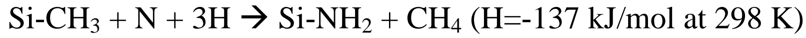

$Si\text{-}CH_3 + N + 3H \rightarrow Si\text{-}NH_2 + CH_4$ (H=-137 kJ/mol at 298 K)

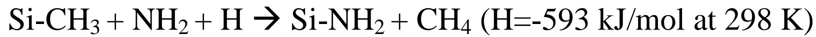

$Si\text{-}CH_3 + NH_2 + H \rightarrow Si\text{-}NH_2 + CH_4$ (H=-593 kJ/mol at 298 K)

These reactions may contribute to the removal of the carbon groups in N_2 containing plasmas. However, the results in this study seem to indicate they are not significant compared to the H radical reactions. The CH_3 structures in either ILD film are not impacted as significantly for N_2 plasma exposure. The effective species in N_2 plasmas are excited N_2 molecules and a small fraction of N radicals. However, it has been reported that a surface amide layer containing N-C=O bonds is generated during exposure to an N_2 plasma [16]. In support of this model, our in-situ XPS spectra indicate the presence of N at the surface of the low-k films.

To further identify the bonding configurations due to N_2 plasma exposure, longer exposures were carried out on 500 nm thick LCHP ILD films. The XPS scans before and after a 30 min N_2 plasma exposure of the LCHP is shown in Fig. 3.6(a). Charging effects have been accounted for by using the 103.3eV SiO_2 Si 2p peak as the reference. The peak at 284.6 eV is attributed to C-Si and C-H bonding, and the peak at higher binding energy ~287.7 eV is assigned to N-C=O structures [25]. Moreover, the N core level at ~399.0 eV shown in Fig. 3.6(b) is indicative of C-N bonding [25]. The Si and O XPS peaks are shown in Fig. 3.7 (a) and (b), respectively. The intensity small increase after processing is attributed to the abstraction of carbon from the film. The film was also evaluated by FTIR, as

shown in Fig. 3.6(c). The double peak structure in the range from 1680 to 1820 cm-1 is related to saturated N-C=O aldehyde (1734 cm^{-1}) and ketone (1716 cm^{-1}) structures. Thus the XPS and FTIR data indicate that the surface layer contains amide like structures. This layer may act as a protective layer reducing radical diffusion into the film.

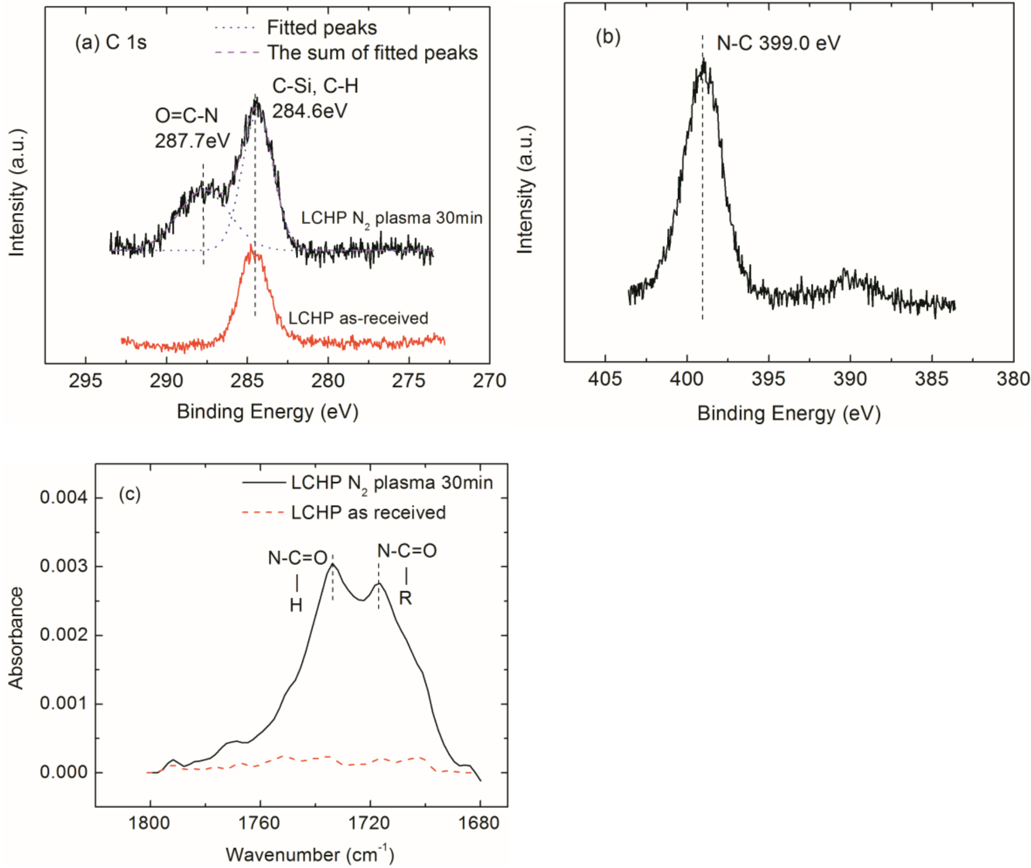

Fig. 3.6 Bonding changes of LCHP ILD after 30 min N_2 plasma treatment as displayed in (a) the C 1 s XPS spectrum; (b) the N 1 s XPS spectrum; and (c) the FTIR spectrum, which shows peaks associated with saturated aldehyde (1734 cm^{-1}) and saturated ketone (1716 cm^{-1}) configurations.

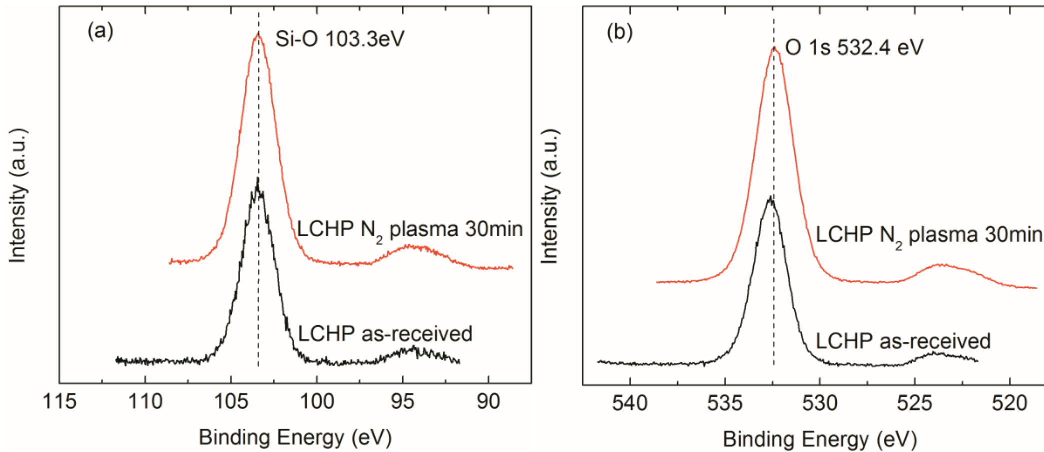

Fig 3.7 XPS spectrum before and after N_2 plasma treatment as displayed in (a) Si 2 p and (b) O 1 s.

A set of experiments has been carried out to study whether the N_2 plasma induces a sealing effect prior to H_2 plasma exposure. A time series of N_2 plasma pre-treatments were completed on the 500 nm LCHP ILD prior to a 5 min H_2 plasma exposure. The N_2 plasma pre-treatment results in a small decrease of CH_3 groups (Fig. 3.8) after H-plasma exposure. The fractional decrease increases as the N_2 plasma exposure time increases. More importantly, compared to N_2/H_2 plasma processes, the N_2 plasma treatment apparently protects carbon groups from H radical abstraction. The fraction of carbon abstraction caused by the H_2 plasma without N_2 plasma pretreatment is about 20%. In contrast, with a 5 min N_2 plasma pretreatment, the fraction is reduced to 3.3%. In addition, the H radicals apparently limit the N2 plasma sealing effect in mixed N_2/H_2 plasmas. The effect may be due to the high diffusivity of H radicals penetrating through the incompletely densified layer. The longer N_2 plasma pretreatments do not provide increased resistance to H_2 plasma exposure which indicates that the thin amide

layer effectively retards the H radical diffusion into the film. The longer time exposures are apparently less effective in sealing pores.

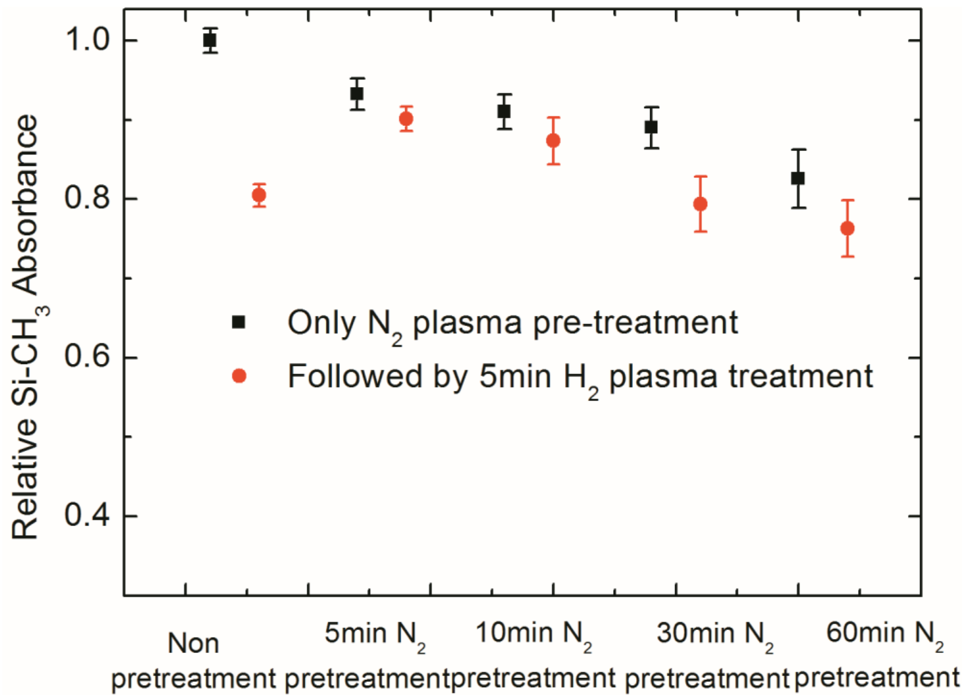

Fig. 3.8 Relative absorbance of the Si-C/Si-O ratio after different time of N_2 plasma pretreatment followed by 5 min H_2 plasma processes.

In summary, since the thermodynamically favorable reactions leading to carbon removal are associated with H radicals, the presence of H2 in the plasma is an essential source for carbon abstraction. However, N radicals lead to the formation of an amide like densified surface that result in a protective layer. After the N2 plasma process, the surface of the ILD layer becomes hydrophilic as the C=O species can react with water leading to -OH termination [16].

3.4.2 Structural changes related to Si-OH formation in LCHP ILD

Besides carbon abstraction, the plasma processes may also introduce other changes which contribute to degradation of the low-k ILD. After plasma

processing the FTIR spectra often indicate an absorption band between 3200 and 3800 cm^{-1} that is assigned to hydroxyl (-OH) groups. The origin of this bond formation is still under debate. It has been proposed that the OH groups are associated with H and N reactions with Si-O-Si structures through reactions such as [10, 13, 26]:

Si-O-Si +2H → Si-H + Si-OH (H=-325 kJ/mol at 298 K)

Si-O-Si + N +2H →$Si-NH_2$ + Si-OH (H=-915 kJ/mol at 298 K)

Si– H + H_2O → Si-OH + 2H (H=-42 kJ/mol at 298 K)

Alternatively, Lee and Grave [8] have argued that the Si-OH formation is due to H2O reacting with Si dangling bonds after the -CH3 groups have been abstracted from the ILD.

Results presented in Fig. 3.8 indicate that for H-containing plasmas, the Si-OH absorption peaks increase significantly compared to the as-received films. In contrast, N_2 plasma processes do not induce obvious water uptake or Si-OH formation. The dielectric constant changes significantly as the H_2 fraction increases. After an H_2 plasma treatment at RT, the dielectric constant increases to 3.5 which is a ~40% increase. In contrast, the processes at 380 ℃ resulted in only a ~16% increase. Evidently, the water uptake is another critical factor that contributes to degradation.

In general, the presence of hydrophobic surface groups leads to problematic metal adhesion issues. In contrast, a hydrophilic surface enables adhesion but results in moisture uptake leading to an increase in k. In order to investigate the changes in the dielectric properties due to hydroxyl formation, the

plasma processes were carried out at elevated temperature (380 ℃), which is considered appropriate for low-k ILD films.

As indicated in Fig. 3.9, the Si-OH concentration is significantly reduced for the sample processed at increased temperature relative to films processed at RT. Thus, the film processed at 380 ℃ apparently absorbs less water during or after processing. The carbon loss has been determined to be at about the same level for both high temperature and room temperature processes. In addition, the contact angle is enhanced with the 380 ℃ plasma process as shown in Fig. 3.10 which also indicates the surfaces processed at increased temperature tend towards hydrophobic character. For the 380 ℃ process, the dielectric constant increase is only 16% after H2 plasma compared to 40% for the RT process. Consequently, if Si-OH formation is limited, the dielectric constant changes are also minimized.

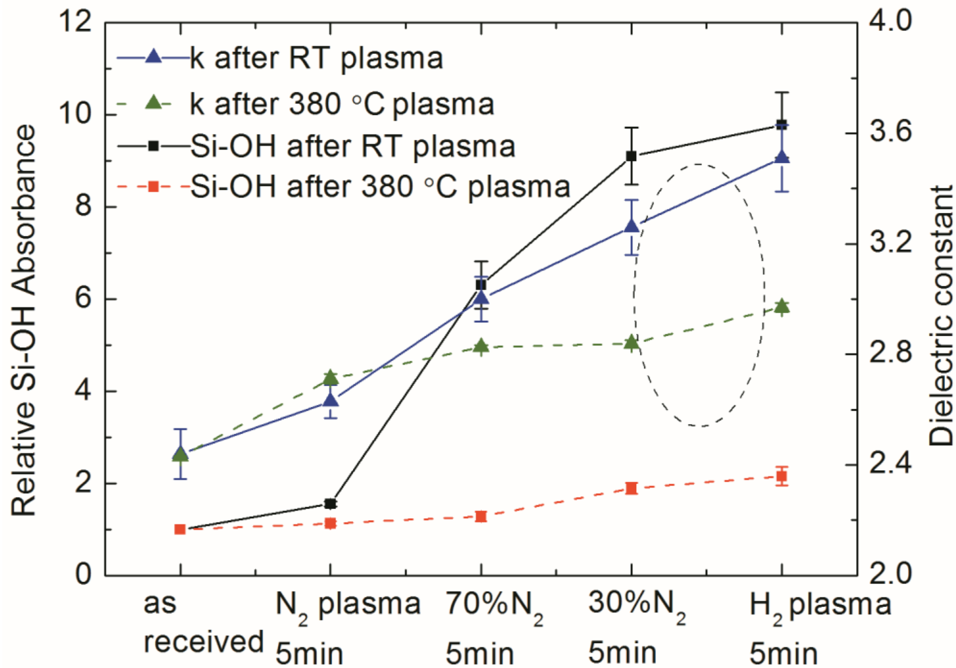

Fig. 3.9 Changes of the FTIR Si-OH absorption band and dielectric constant after various RT and 380 ℃ plasma processes of the 500nm LCHP film.

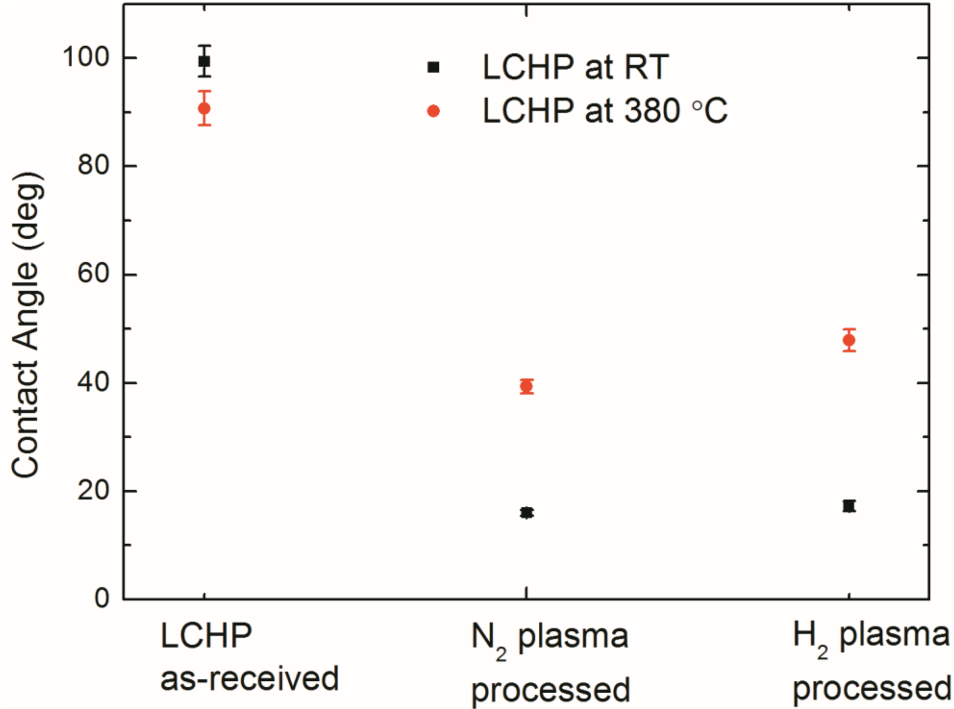

Fig. 3.10 Contact angle after various RT and 380 ℃ plasma processes of the 500 nm LCHP film.

The most substantial increase in k appears related to polar group formation (Si-OH) due to the availability of Si dangling bonds. While water readily reacts with these sites to incorporate OH groups, the high temperature process leads to a reduction in the concentration of OH which may be explained by secondary reactions such as Si-OH+HO-Si → Si-O-Si+H_2O (H=0 kJ/mol at 298 K). Thus at higher temperature the transformation of 2 (Si-OH) to a Si-O-Si configuration would be enhanced [27], and the concentration of Si dangling bonds available for Si-OH polar species formation would decrease.

3.4.3 Effects of N_2/H_2 plasma processing on CMP Cu surfaces

XPS examination of the as-received Cu surfaces indicated the presence of a surface oxide as well as carbon and carbon-oxide (carbonate) contamination. The XPS results (Fig. 3.11) show that both carbon and metal oxide contamination are decreased after vacuum thermal annealing. It is evident that after the 480 ℃ thermal annealing process, the surface contamination is not discerned in the XPS scans. However, according to ITRS 2010 interconnect processes require keeping the overall temperature budget below 400-450 ℃ [1]. Therefore, it is essential to optimize the N_2/H_2 plasma process at lower temperature.

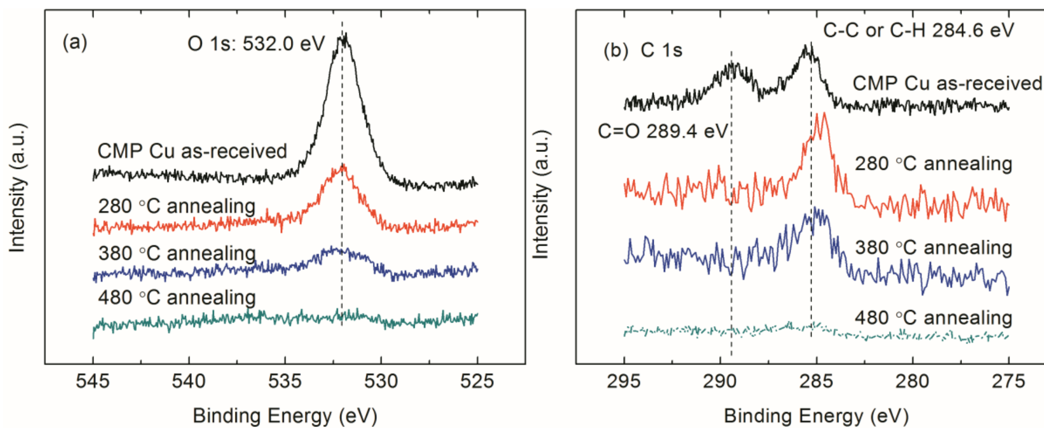

Fig. 3.11 XPS spectra of CMP Cu film before and after different thermal anneals. (a) O 1 s peak, (b) C 1 s peak.

The N2/H2 plasma processes have been applied to the CMP Cu surfaces using the conditions studied for plasma cleaning of the ILD layers. The results for in-situ XPS after various N_2/H_2 plasma cleaning processes are indicated in Fig. 3.12(a). The RT N_2/H_2 plasma processes reduced the oxide and carbon contamination, but significant contamination remains on the surface. Repeating the processes with the sample at 380 ℃ shows that the CMP Cu is effectively

cleaned using a range of N_2/H_2 plasma processes. Reactions that are important for the process are suggested below:

$CuCO_3 \rightarrow CO_2 + CuO$ (heating) $2CuO + C \rightarrow 2Cu + CO_2$ (heating)

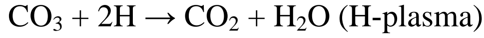
$CO_3 + 2H \rightarrow CO_2 + H_2O$ (H-plasma)

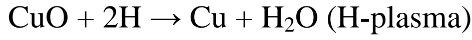
$CuO + 2H \rightarrow Cu + H_2O$ (H-plasma)

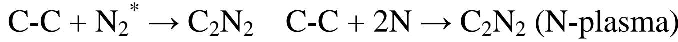
$C\text{-}C + N_2^* \rightarrow C_2N_2$ $C\text{-}C + 2N \rightarrow C_2N_2$ (N-plasma)

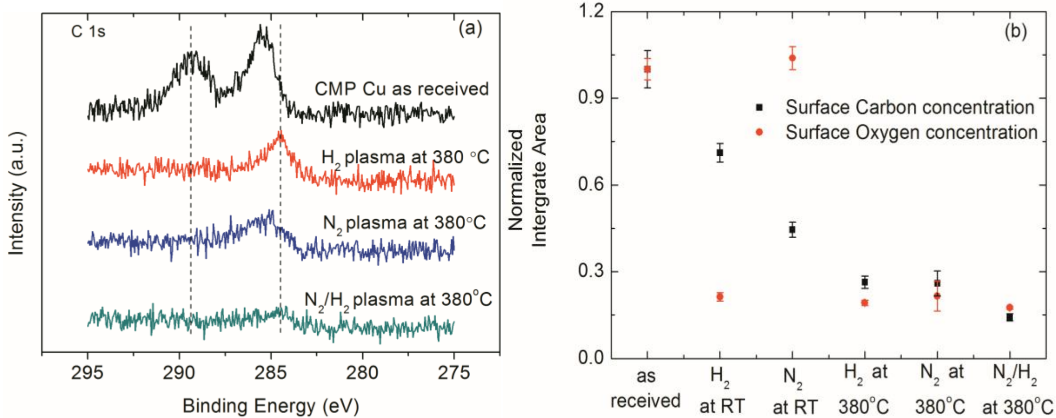

Fig. 3.12 (a) XPS spectrum of CMP Cu surfaces before and after various N_2 and H2 plasma cleaning at 380 ℃; (b) integrated XPS peaks normalized to the as received sample for various plasma processes at RT and 380 ℃.

Heating effectively induces the copper oxide to react with carbon contamination leading to a reduction in both carbon and oxide contamination. The presence of H radicals also contributes to the removal of carbonates and reduction of the remaining oxide. The reactive species reported in an N_2 plasma include N^*, N^{2+}, N_2^* [16, 28, 29], which may react with C-C bonded structures. Since evidence of N was not detected by XPS, we may assume that the product of the reaction evolves as a volatile gas. Fig. 3.12(b) compares the normalized integrated areas of the O 1s and C 1s XPS peaks for various plasma processes at RT and 380 ℃.

(The C 1s integrated peak includes the peaks associated with carbonate and C-C structures.) From the results presented here, an effective cleaning process involves N_2/H_2 plasma with the sample at an elevated temperature of ~380 ℃. These same plasma processes would also clean the ILD surfaces without substantial degradation, and the elevated temperature assists in removing contamination from the Cu surfaces.

3.5 Summary and conclusions

This study focused on plasma induced modifications of low-k ILD dielectrics and contamination reduction of CMP Cu films. For the CMP-Cu surfaces, vacuum annealing to 480 ℃ resulted in reduction of carbonate and surface oxide contamination. However, the low-k ILD films are not stable at this temperature [1].

Consequently, a range of N_2/H_2 remote plasma process were applied to ILD layers to determine approaches to minimize degradation of the low-k characteristics, while identifying a process that simultaneously reduces contamination on CMP-Cu surfaces.

For the ILD films, the carbon concentration is substantially reduced in an H-containing plasma indicating the role of hydrogen in abstracting carbon groups. The process results in an increase in the dielectric constant that can be attributed to two effects. First, the carbon removal generates Si dangling bonds which may react with moisture after the sample is exposed to atmosphere. Second, at elevated temperature, the carbon loss can result in a change of network topography from cage to network and the increased density leads to an increase in the dielectric

constant. Meanwhile, the elevated temperature inhibits the formation of Si-OH structure. In our experiments, the OH incorporation leads to a more significant increase in dielectric constant than the change in network topography.

The results established that an initial remote N_2 plasma plays a role in protecting the low-k ILD layer by forming a densified surface. The surface can then be exposed to an H-containing plasma with minimal degradation of the dielectric properties.

The results indicated that elevated temperature N_2/H_2 remote plasma processing enhances the stability of the low-k ILD layer by inhibiting the formation of polar Si-OH structures. The higher temperature processes tend to a more hydrophobic surface condition as indicated by contact angle measurements. The dielectric constant measurements also indicate that the elevated temperature processes retain the low-k properties as compared to RT processes. Finally, the elevated temperature N_2/H_2 remote plasma processes that minimize ILD damage results in efficient contamination removal from the CMP Cu surfaces. Therefore, a range of N_2/H_2 plasma process at increased temperature that follow an remote N_2 plasma pretreatment should be effective in reducing ILD damage and cleaning both ILD and CMP-Cu surfaces.

While this has been an extensive study with over 100 plasma processing experiments, there is still room to further improve the process by optimizing the temperature and plasma parameters. In addition, multi-step N_2/H_2 plasma processes should also be considered. The specific reactions identified in this study

should help guide further improvement of the plasma process to simultaneously clean CMP Cu and low-k ILD.

REFERENCES

1. "International Technology Roadmap for Semiconductors," Semiconductor Industry Association, http://www.itrs.net/Links/2010ITRS/Home2010.htm.
2. A. Grill and D. A. Neumayer, J. Appl. Phys. 94, 6697 (2003).
3. A. Grill, Annu. Rev. Mater. Res. 39, 49 (2009).
4. G. J. Stueber, G. S. Oehrlein, P. Lazzeri, M. Bersani, M. Anderle, E. Busch, and R. McGowan, J. Vac. Sci. Technol. B 25, 1593(2007).
5. M. A. Worsley, S. F. Bent, N. C. M. Fuller, T. L. Tai, J. Doyle, M. Rothwell, and T. Dalton, J. Appl. Phys. 101, 013305 (2007).
6. M. A. Goldman, D. B. Graves, G. A. Antonelli, S. P. Behera, and J. A. Kelber, J. Appl. Phys. 106, 013311 (2009).
7. X. Hua et al., J. Vac. Sci. Technol. B 24, 1238 (2006).
8. J. Lee and D. B. Graves, J. Phys. D: Appl. Phys. 43, 425201(2010).
9. P. Liu, T. Chang, Y. Mor, and S. M. Sze, Jpn. J. Appl. Phys., Part 1 38, 3482 (1999).
10. Y. Kim, H. J. Kim, J. Y. Kim, and Y. Lee, J. Korean Phys. Soc. 40, 94(2002).
11. K. Yonekura, S. Sakamori, K. Goto, M. Matsuura, N. Fujiwara, and M. Yoneda, J. Vac. Sci. Technol. B 22, 1071 (2004).
12. S. Xu et al., J. Vac. Sci. Technol. B 25, 156 (2007).
13. N. Posseme, T. Chevolleau, T. David, M. Darnon, O Louveau, and O. Joubert, J. Vac. Sci. Technol. B 25, 1071(2007).
14. L. Prager et al., Microelectron. Eng. 85, 2094 (2008).

15. P. Liu, T. Chang, Y. Yang, Y. Cheng, and S. M. Sze, IEEE Trans. Electron Devices 47, 1733 (2000).

16. M. Fukasawa, T. Tatsumi, K. Oshima, and K. Nagahata, J. Vac. Sci. Technol. A 26, 870 (2008).

17. J. Torres, J. Palleaua, F. Tardif, H. Bernard, A. Beverina, P. Motte, R. Pantel, and M. Juhel, Microelectron. Eng. 50, 425 (2000).

18. Y. Ein-Eli and D. Starosvetsky, Electrochim. Acta 52, 1825 (2007).

19. Y. Ein-Eli, E. Abelev, M. Auinat, and D. Starosvetsky, Electrochem. Solid-State Lett. 8, B69 (2005).

20. R. L. Deutscher and R. Woods, J. Appl. Electrochem. 16, 413 (1986).

21. M. A. Worsley, S. F. Bent, S. M. Gates, Nicholas C. M. Fuller, W. Volksen, M. Steen, and T. Dalton, J. Vac. Sci. Technol. B 23, 395 (2005).

22. A. M. Urbanowicz, D. Shamiryan, A. Zaka, P. Verdonck, S. De Gendt, and M. R. Baklanov, J. Electrochem. Soc. 157, H565 (2010).

23. M. Mesi, C. Cavallotti, and S. Carra in Chemical Vapor Deposition, Proceedings of the Fourteenth International Conference and EUROCVD-11, edited by M. Allendorf and C. Bernard (The Electrochemical Society, Pennington, NJ, 1997), pp. 278–285.

24. S. Chen, T. Chang, W. Chen, Y. Lo, K. Wu, S. M. Sze, J. Chen, I. H. Liao, and F. Y. Huang, Thin Solid Films 519, 3897 (2011).

25. G. Beamson and D. Briggs, High Resolution XPS of Organic Polymers (Wiley, London, 1992).

26. A. Grill, V. Sternhagen, D. Niemeyer, and V. Patel, J. Appl. Phys. 98, 074502 (2005).

27. T. Fukumura, S. Sugahara, and M. Matsumura, Jpn. J. Appl Phys., Part 1 40, 46 (2001).

28. R. P. Vaudo, J. W. Cook, and J. F. Schetzina, J. Vac. Sci. Technol. B 12, 1232 (1994).

29. S. Miyanaga, T. Kaneko, H. Ishida, and R. Hatakeyama, Thin Solid Films 518, 3509 (2010).]

Chapter 4

CU FILM THERMAL STABILITY ON PLASMA CLEANED POLYCRYSTALLINE RU

4.1 Abstract

The first part of this study examined oxide stability and cleaning of Ru surfaces. The surface reactions during H_2 plasma exposure of Ru polycrystalline films were studied using X-ray photoelectron spectroscopy (XPS). The ~2 monolayer native Ru oxide was reduced after H-plasma processing. However, absorbed oxygen, presumably in the grain boundaries, remains after processing. A vacuum thermal anneal at 150 ℃ substantially removes both surface oxide and absorbed oxygen which is attributed to a reduction by carbon contamination. The second part of the study examined the thermal stability of Cu on a Ru layer. The thermal stability or islanding of the Cu film on the Ru substrate was characterized by *in-situ* XPS. After plasma cleaning of the Ru adhesion layer, the deposited Cu exhibited full coverage. In the contrast, for Cu deposition on the Ru native oxide substrate, Cu islanding was detected and was described in terms of grain boundary grooving and surface and interface energies. The oxygen in the grain boundary has negligible contribution to the surface energy and does not contribute to Cu islanding.

4.2 Introduction

Materials with low dielectric constants (low-k), when used as an interlayer dielectric (ILD) with copper interconnects, have shown significant promise in reducing RC time delays and energy consumption in next-generation silicon

integrated-circuit technology [1-3]. Traditionally, Cu interconnect technology has utilized a physical vapor deposition (PVD) Cu seed layer grown on a Ta/TaN diffusion barrier prior to the Cu electroplating process[4]. However, the relatively complex and thick tri-layer configuration presents scalability issues for upcoming interconnect technology generations [5]. Specifically, the PVD Cu process has limitations in providing step coverage and uniform side wall coverage. While the thermochemical stability and lack of active grain boundaries in Ta or TaN layers meet the diffusion barrier requirements for Cu films, delamination or void formation has been observed [6] since the native oxide results in deleterious Cu de-wetting or agglomeration [7]. Furthermore, a diffusion barrier with a thickness <5 nm is specified for the 32 nm technology node and below [5]. For a conventional Cu dual-damascene process, the continuous PVD Cu seed layer with a minimum thickness of ~30-40 nm [8] may not be appropriate for future technology nodes. Therefore, new barrier layer approaches are being considered which employ seedless direct-plate metals.

The interconnect chapter in the International Technology Roadmap for Semiconductor (ITRS) [5] suggests that for the sub-22 nm nodes, the Cu electrochemical deposition (ECD) gap fill requirement could be achieved with the elimination of the current PVD Cu seed/nucleation layer and replacement of the TaN/Ta barrier with a material capable of supporting direct Cu electroplating. Thus, research has focused on the adhesion of Cu on direct platable materials such as W, Pd, Ir, Os and Ru. Prior results have established that W based layers dissolve during typical Cu electroplate conditions [9]; Pd is stable in chemical

solutions, but the polycrystalline structure leads to Cu interdiffusion [10]; Ir and Os have also been investigated because of their barrier properties with Cu while their effectiveness as a diffusion barrier has not been established [11, 12]. Of the many potential metals, ruthenium has received broad interest and is one of the primary direct plate materials being considered because of its lower electrical resistivity and negligible solubility in Cu even at 900 ℃ [13]. In addition, atomic layer deposition (ALD) based growth methods have been developed for Ru [14-16].

The adhesion properties of Cu on Ru have been identified as one of the most important characteristics for reliable interconnects. In Cu dual-damascene structures, electromigration (EM) failure caused by Cu atomic diffusion of metal atoms under the influence of high current densities occurs predominately in regions of poor adhesion. EM in Cu lines occurs by surface diffusion which has a lower activation energy than grain boundary diffusion [17].

Thus, adhesion and thermal stability between Cu and the adhesion/barrier layer have become technology issues. In particular, the oxidation resistance of Ru and the impact of RuO_x surface oxides on Cu wetting have not been fully characterized [13]. There is also a critical need to determine the degree of surface oxidation that limits film stability and find ways to ameliorate it once it has formed. The scientific issues are then 1) the identification of surface reactions appropriate for reduction of surface oxides [18], and 2) determination of the role of surface oxides in adhesion and islanding of the Cu films. The adhesion of Cu on Ru may be considered in terms of surface and interface energies. Kim and

Shimogaki [19] investigated stability of CVD Cu on both Ru and Ta layers and determined that CVD Cu showed relatively weaker adhesion on Ta surfaces. It has been suggested that lattice matching of face-centered cubic Cu (111), results in better adhesion to hexagonal close-packed (hcp) structure metals such as Ru than body-centered cubic metals such as Ta [13]. However, surface and interface energies are expected to provide the driving force to islanding or de-wetting even in the absence of film stress [20, 21]. To explore these effects in this study, the coverage and roughness of Cu films on Ru surfaces are characterized as a function of temperature and surface conditions.

In our previous work, a remote N_2/H_2 plasma process has been used to clean CMP Cu surfaces [22]. In this study, *in-situ* remote plasma processing was also employed for surface preparation of the Ru film prior to Cu deposition. The wetting properties of the Cu/Ru interface have been characterized as a function of temperature using in situ XPS. The effects of several cleaning processes have been studied for polycrystalline Ru adhesion layers as well as the stability or de-wetting characteristics of Cu on the processed Ru films.

4.3 Experiment

The Ru films were deposited by atomic layer deposition (ALD) onto 300 mm diameter (100) Si wafers which had a 100 nm thermal oxide (SiO_2). The films, which were provided by Intel, were ~8 nm thick. The Ru adhesion film is polycrystalline and X-ray diffraction (XRD) shows (100) and (101) peaks. The wafers were subsequently diced into ~ 1.5 x 1.5 cm^2 sections and mounted onto a

molybdenum plate using tantalum wires. The samples were then loaded into the UHV transfer line system.

The UHV system is maintained at ~5x10^{-10} Torr with multiple chambers interconnected through a linear transfer line. In this study, the experimental sequence involved *in-situ* plasma surface processing and/or annealing, surface characterization (XPS), *in-situ* Cu deposition (e-beam metallization), *in-situ* annealing (remote H_2 plasma chamber) and surface characterization (XPS). The XPS scans were obtained using a VG Clam II spectrometer operated with a Mg Kα x-ray source (h*ν*=1253.6 eV). The e-beam metallization system employed a Thermionics e-GUN™ evaporation source (100-0050). The morphological changes of the surfaces were observed using an Agilent™ AFM model 5500.

The plasma system used for the H_2 treatments is shown schematically in Fig. 4.1 and has been previously described [22]. Briefly, this chamber was designed for the application of various gases which were delivered through a quartz plasma tube at the top of the chamber. The ~32mm diameter quartz tube is encircled with a 12 turn copper coil that is coupled to a rf power (13.56 MHz) supply. The excited molecules and radicals were transported to the sample centered in the chamber below. The pressure was maintained by regulating the gas flow and controlling a throttle valve in front of the turbo molecular pump. Typical plasma operating conditions were as follows: the rf power was maintained at 30 W, the pressure at 60 mTorr, the temperature at room temperature, and the gas flow at 90 standard cubic centimeter per minute (sccm). The base pressure was 7x10^{-9} Torr.

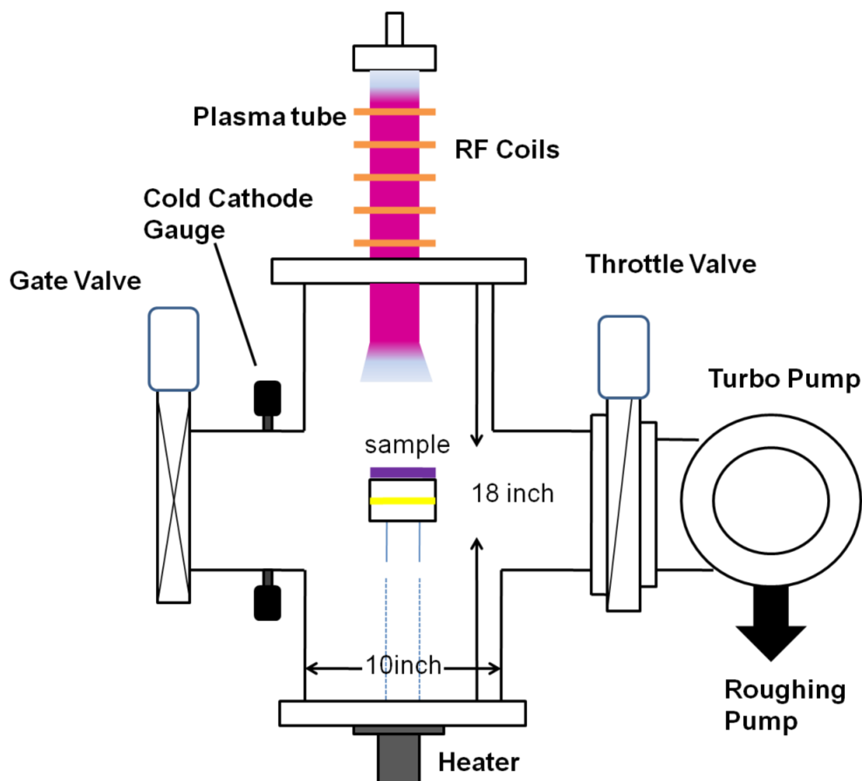

Fig. 4.1 Schematic of the RF remote plasma chamber for surface processing and vacuum annealing.

To investigate the Cu thermal stability properties on the cleaned Ru surfaces, a 10 nm Cu film was e-beam deposited on three different Ru substrates: as-received, 10 min H_2 plasma processed at room temperature, and 5 min vacuum annealed at 150 ℃. The Cu completely covered each sample such that the Ru layer could not be detected by XPS. After deposition, the samples were annealed to 450 ℃, and XPS scans were repeated to evaluate the properties of Cu on Ru. The annealing was conducted in the plasma chamber using a tungsten irradiation filament heater located behind the sample holder. During annealing, the sample was heated to constant temperature (calibrated with a Mikron-M90Q infrared pyrometer), and monitored with a Eurotherm 808 thermocouple controller located

behind the center of the molybdenum plate. The thermal stability properties were characterized using *in-situ* XPS and *ex-situ* AFM. The observation of the Ru XPS signal is then the signature for de-wetting of the Cu layer.

4.4 Result and Discussion

4.4.1 Ruthenium oxide and surface processes

To investigate the thermo chemical stability of the Ru surface oxide, the Ru samples were exposed to H_2 plasma processes for various times and characterized by XPS. Scans of the Ru $3d_{3/2}$ and $3d_{5/2}$ core levels are shown in Fig. 2 before and after 4 min H_2 plasma processing. There are two major components that contribute to the shape of the Ru $3d_{5/2}$ core level for the as-received surface as shown in Fig. 4.2(a): 1) a peak at lower binding energy (280.2 eV) associated with metallic Ru, and 2) a peak at the higher binding energy (281.2 eV) which has been attributed to RuO_2 (Ru^{4+}). It is also likely that these samples retain some residual carbon contamination from the ALD deposition, but the carbon 1s peak is obscured by overlap with the Ru $3d_{3/2}$ signal [23]. As shown in Fig. 4.2(b), after 4 min H_2 plasma processing, the Ru 3d core levels are evident at essentially the same binding energy of the as-received sample with increased intensity consistent with oxide removal.

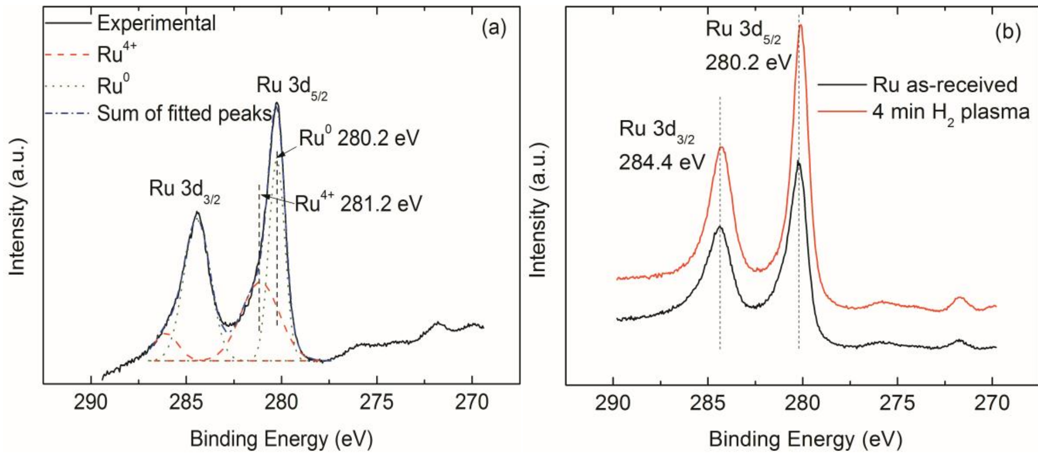

Fig. 4.2 XPS scans of the Ru $3d_{3/2}$ and $3d_{5/2}$ core levels (a) of the as-received Ru sample showing the fitting to the oxygen related and bulk peaks; and (b) comparing the as-received surface before and after H_2 plasma processing (4 min).

The presence of oxygen is confirmed by an evident O 1s peak as shown in Fig. 4.3(a). The O 1s peak has a component at 529.8 eV [24] which corresponds to oxygen atoms from RuO_2 (O^{2-}) and another component at 531.2 eV. This 531.2 eV O 1s peak has been attributed to sub-surface grain boundary oxygen [23] and higher Ru oxidation states (RuO_3 or RuO_4) may also contribute. However, the binding energies of the Ru $3d_{5/2}$ core level for RuO_3 and RuO_4 were reported to be 282.5 eV and 283.3 eV, respectively [25], which suggests that these higher oxidation states are not substantially present in the films.

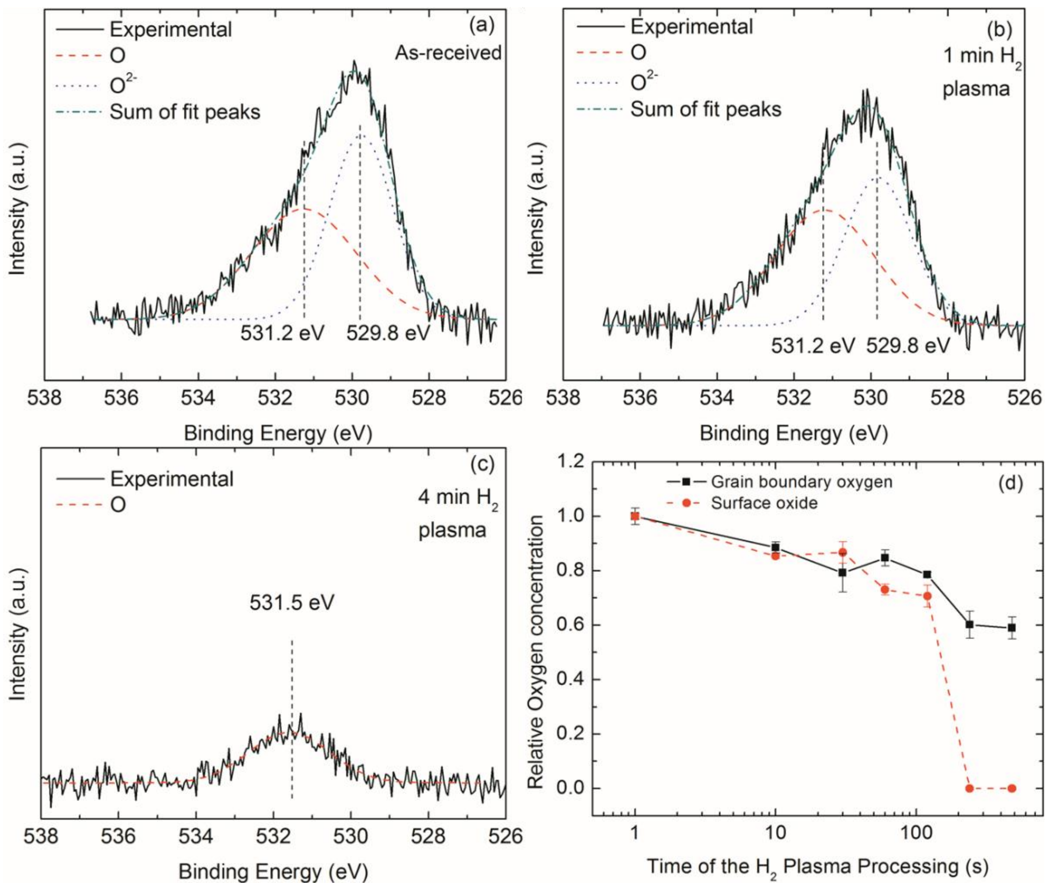

Fig. 4.3 XPS scans of the O 1s core level of (a) the as-received Ru surface; (b) after H_2 plasma processing (1 min); (c) after H_2 plasma processing (4 min); and (d) relative oxygen concentration vs H_2 plasma exposure time. The dashed lines in (a) (b) and (c) show peak fittings: where the 531.2 eV feature (531.5 eV in (c)) was associated with grain boundary oxygen and the 529.8 eV feature was associated with surface oxide.

Previous studies have described the oxygen diffusion phenomenon in Ru films. Iwasaki *et al.* [26] and Belau *et al.* [27] have detected the presence of the subsurface oxygen using angle dependent XPS spectra. Absorbed oxygen diffusion was also reported by Reed *et al.*, using LEED and AES to study the oxygen interaction on the Ru (101) surface. Due to the non-electrovalent bond

between Ru and O which results in lower electron density and higher binding energy, the 531.2 eV oxygen peak is most likely associated with absorbed atoms [25]. It is reasonable to assign these species in our case to grain boundary absorbed oxygen [23].

Upon H_2 plasma exposure the two components decrease at substantially different rates. The intensity of the lower binding energy peak (~529.8 eV) decreased faster and is no longer evident after the 4 min H_2 plasma process. It is evident that the surface RuO_2 has been substantially reduced during the H_2 plasma process [26, 28, 29]. The peak at higher binding energy (~531.2 eV), on the other hand, remains after the 4 min H_2 plasma process (Fig. 4.3(c)). The peaks were fit using Gaussian functions with both peak position and peak width as variables. This analysis suggests that the H_2 plasma treatment effectively removes the surface oxide layer, but residual oxygen within the bulk remains. The relative concentration regarding the two components are plotted vs processing time in Fig. 4.3(d).

In this study an as-received Ru sample was annealed in the plasma system under a vacuum of ~5×10^{-8} Torr. After a 5 min thermal anneal (150 ℃), neither of the O 1s peaks (~529.8 eV and ~531.2 eV) were discerned in the XPS scans as shown in Fig. 4. The elevated temperature anneal results in the removal of both sub-surface oxide and absorbed oxygen. To understand the role of H radicals and the possible presence of carbon, a low-carbon Ru film was deposited in the e-beam system on a cleaned p-type Si wafer followed by both O_2 plasma and H_2 plasma processes. The XPS scans of the O 1s peak are displayed in Fig. 4.4 and

compared with the scans of the as-received sample which may have carbon in the film. The results indicate that with or without carbon, the surface oxide (529.8 eV) was substantially removed after H_2 plasma processes indicating the role of H radicals in oxide reduction. Meanwhile, the residual subsurface oxygen remained for both samples.

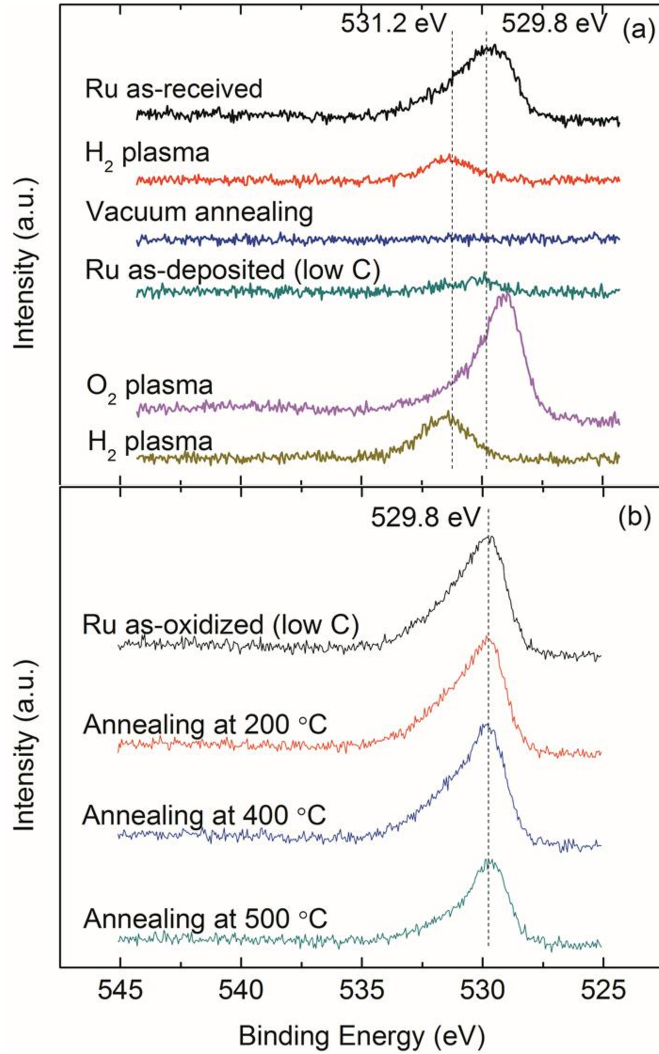

Fig. 4.4 XPS scans of the O 1s core level of (a) as-received Ru after H-plasma processing and vacuum annealing, and the carbon-free Ru film followed by

oxidation and H-plasma processing; and (b) the carbon-free Ru film following vacuum annealing.

The thickness of the Ru surface oxide was determined from the Ru and O core level scans using the following relationship [30]:

$$\Theta_O = \frac{I_O}{I_{Ru}} \times \frac{S_{Ru}}{S_O} \times \sum_{n=0}^{\infty} Exp[\frac{-nd_{RuO_2}}{\lambda_{Ru}\cos\phi}]$$

where Θ_O is the coverage or the number of absorbed oxygen per unit area (atoms/cm^2) divided by the number of Ru atoms per unit area (atoms/cm^2). One monolayer coverage refers to one oxygen atom per Ru surface atom (atoms/cm^2) on the c plane. The I_O and I_{Ru} are the integrated areas of the O 1s peak for O^{2-} (529.8 eV), and the Ru 3d peaks; S_O (0.711) and S_{Ru} (4.273) are the XPS sensitive factors for O and Ru, respectively. Moreover, d (1.55 Å) is the distance between two O or two Ru planes [31]. Also λ_{Ru} (15 Å) is the inelastic mean free path for the Ru 3d photoelectrons [32]. Here, ϕ (20°) is the angle between the analyzer and sample. From this analysis, the results indicate 2.1 monolayers of oxygen in the surface oxide. This could imply a native oxide that is about 0.6-0.75 nm thick [31]. It has been reported that oxygen can readily diffuse through RuO_2 [33]. This suggests that the Ru native oxide is limited by the reaction at the Ru surface.

During the hydrogen plasma process it appears that H radicals enable the removal of the surface oxide which is ~2 monolayers as noted above. One possible reaction route is as follows:

$RuO_2 + 2H_2 \rightarrow Ru + H_2O$ (ΔG = -31.6 kJ/mol at 297 K).

Iwasaki *et al.* proposed [24] that H radicals combine with surface O atoms to first form Ru-OH, followed by formation of H_2O which desorbs:

$$H + RuO \rightarrow Ru\text{-}OH \qquad Ru\text{-}OH + H \rightarrow Ru + H_2O$$

To follow a similar path for removal of the subsurface oxygen would involve the diffusion of H and/or OH into the film. The results indicate that the relative concentration of the grain boundary oxygen is essentially constant over the processing time indicating it is not reduced by the atomic hydrogen.

While exposure to a room temperature H plasma process removes the surface oxides, vacuum annealing of the ALD films results in the removal of both the surface and grain boundary oxygen in the Ru film. However, it has been reported that the RuO_2 surface oxide was not reduced in vacuum at temperatures up to 500 °C [34]. In contrast, Wang *et al.* [35, 36] found that CO is oxidized to CO_2 through interaction with RuO_2 at 300K. Since residual carbon may be expected after the ALD deposition of the Ru film, it is reasonable to propose that the reduction of RuO_2 during vacuum annealing occurs as follows [37]:

$$RuO_2 + C \rightarrow Ru + CO_2 \ (\Delta G = -23.7 \text{ kJ/mol at } 297 \text{ K}).$$

The presence of carbon may also assist oxygen removal during the H-plasma process. To explore these possibilities, the H-plasma process and thermal annealing were applied to the oxidized, low carbon Ru film. The XPS scans of the O 1s core level are shown in Fig. 4.4. The results in Fig. 4.4(a) again show that the H radicals substantially remove the surface oxide while leaving the subsurface grain boundary oxygen. It appears that the presence of C is not necessary to remove the surface oxide in an H-plasma process. The results in Fig. 4.4(b) show

that for the low carbon Ru film, the oxygen 1s peak intensity is unchanged for annealing to 400 ℃. This is in contrast to the results for annealing of the ALD Ru films where the surface oxide is reduced at 150 ℃. The surface oxide of the low carbon Ru film was partially reduced when the annealing temperature was increased to 500 ℃ which is in a agreement with the prior report [34]. Thus, the room temperature H_2 plasma process will reduce an oxide on Ru film surfaces independent of the presence of carbon contamination. However, the presence of carbon in the film contributes to the reduction of the oxide at elevated temperatures.

4.2.2 Cu thermal stability on Ru

To investigate the thermal stability of Cu on Ru, various Ru/Cu interfaces were characterized by XPS. By comparing the intensity of the Ru 3d core level before and after a 450 ℃ anneal, morphology changes in the Cu films can be identified. The results for the oxidized, plasma cleaned and annealed samples are summarized in Fig. 4.5. After Cu deposition and before annealing, the Ru signal is not evident indicating that all surfaces are covered with a continuous Cu film. After annealing, the Ru 3d intensity increases significantly for Cu on the as-received Ru substrate. In contrast, for Cu deposited on the Ru surface processed with an 10 min H_2 plasma or 150 ℃ thermal anneal, the Ru 3d peak is not discerned after the 450 ℃ anneal. In other words, a thermally activated process leads to Cu island formation on the oxidized Ru surface, and this process does not occur on the cleaned Ru surfaces. To display the island formation morphology,

the surface topography of each sample was measured by AFM and the results are shown in Fig. 4.6.

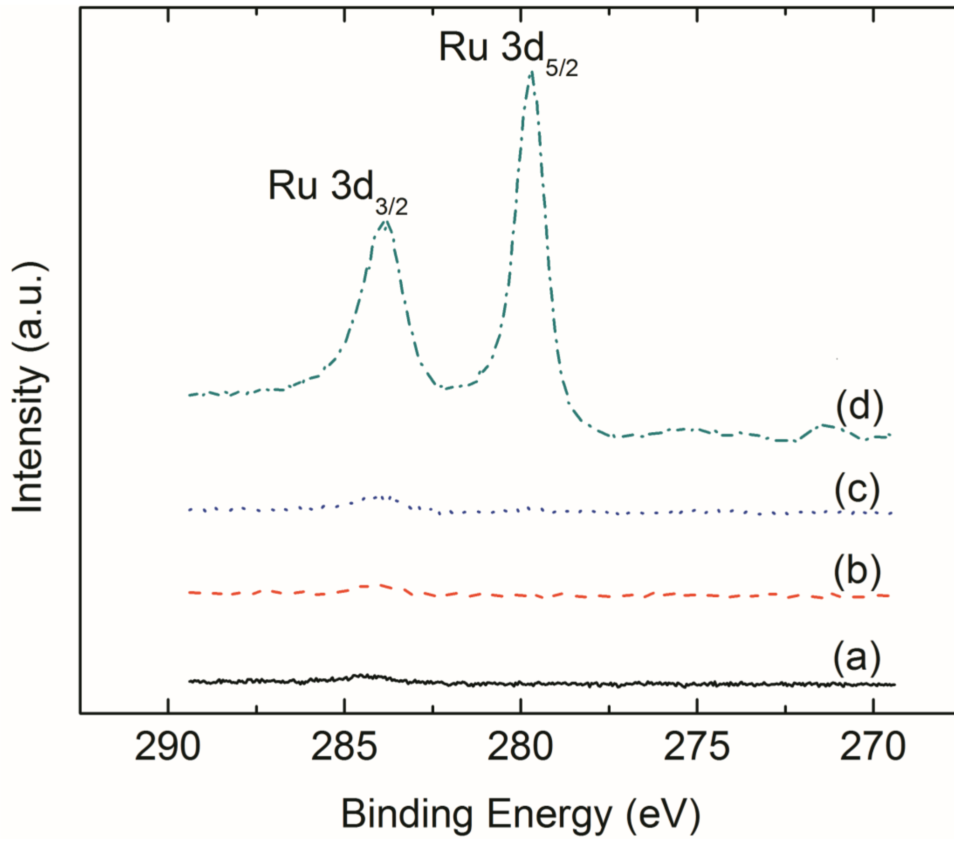

Fig. 4.5 XPS scans of the Ru 3d core level for 10 nm Cu on Ru, (a) prior to annealing; After annealing at 450 ℃ for Cu on processed Ru substrates; (b) 150 ℃ thermal anneal of Ru; (c) H_2 plasma processed; (d) as-received.

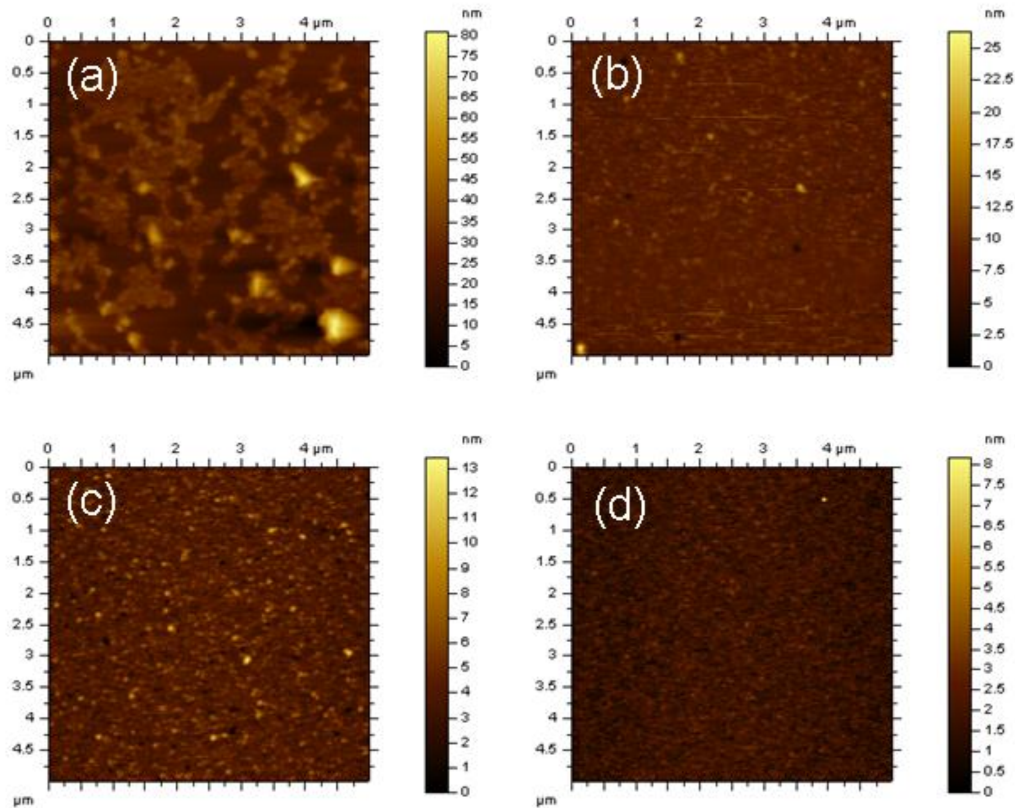

Fig. 4.6 AFM images of 10 nm Cu coated on different Ru substrates, (a) Ru as-received, RMS = 7.0 nm; (b) Ru substrate with H_2 plasma processed, RMS = 1.0 nm; (c) Ru substrate with 150 ℃ thermal flash, RMS = 0.9 nm; (d) Prior to annealing, RMS = 0.5 nm.

Islanding or agglomeration mechanisms are often described in terms of "grain boundary grooving." Genin *et al.* [38] developed a numerical analysis of the surface evolution. The model was adapted to explain the thermal de-wetting of a surface in the vicinity of a triple junction of the surfaces and grain boundary. Miller *et al.* [39] suggested grooves were formed at triple junction areas during film deposition, and the film thermodynamic stability was determined by the lowest free energy configuration of the system. If the island formation lowers the

total energy, then the film evolves toward an islanded surface when the grain size to film thickness ratio exceeds a critical value.

In light of this, the results can be explained in terms of the surface and interface energies. The initial uniform Cu coverage on both clean and oxidized Ru surfaces is achieved after room temperature deposition. This is a quasi-equilibrium stage which may have an energy barrier to further film evolution. Evidence of the grain structure is displayed in the AFM image, which shows roughness features that reflect the grain dimensions (~ 50 nm). However, during vacuum thermal annealing, the energy barrier is overcome, and the surface morphology evolves until the free energy of the system reaches its minimum. In the evolution from the quasi equilibrium stage, the grain boundary contact angle increases, and the grain boundary length decreases as the groove structure becomes dominant. The critical continuity condition occurs when the grain boundary has just disappeared (Fig. 4.7(b)), and the junction exhibits a critical contact angle θ_c. If the substrate contact angle θ_D is larger than θ_c, the grain boundary evolves to the substrate contact angle resulting in islanding and an exposed substrate (Fig. 4.7(c)).

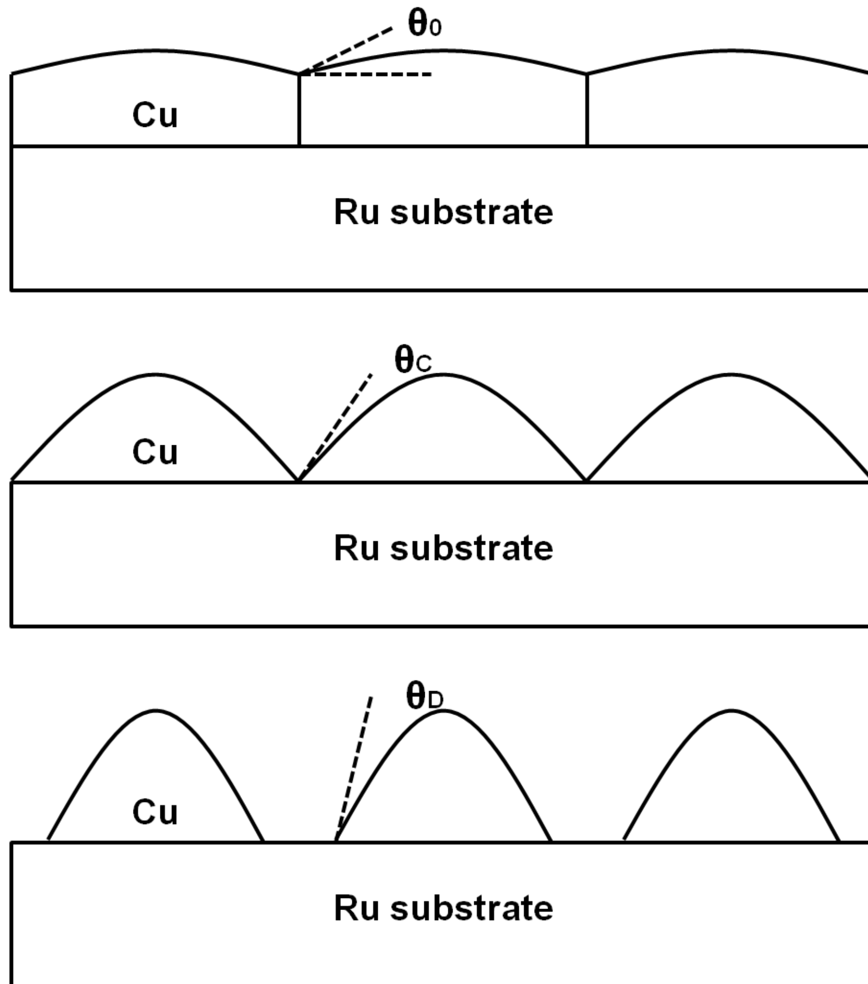

Fig. 4.7 Groove structure evolution and contact angle changes due to different surface energies configuration (a) initial stage of groove structure formation with contact angle θ_0; (b) critical continuity condition θ_C; (c) isolated Cu island formation when $\theta_D > \theta_C$.

The final equilibrium condition, therefore, may be determined by the balance of the substrate surface energy, the interface energy, and the film surface energy. In order to explore this effect, another set of experiments have been carried out: 10 nm Cu films were deposited onto as-received Ru adhesion layers and then individually annealed at different temperatures (150 ℃, 200 ℃, 250 ℃,

and 450 ℃). As shown in Fig. 4.8, the Ru signal is not evident until the annealing temperature increases to 250 ℃. Extended time annealing was carried out at 200 ℃ from 30 min to 4 h, and the substrate Ru was not detected. These results can be described by the energy barrier shown in Fig 4.9. The evolution requires sufficient energy E_A for Cu surface diffusion. Once the surface diffusion is enabled, the surface morphology configuration is ultimately defined by the surface and interface energies.

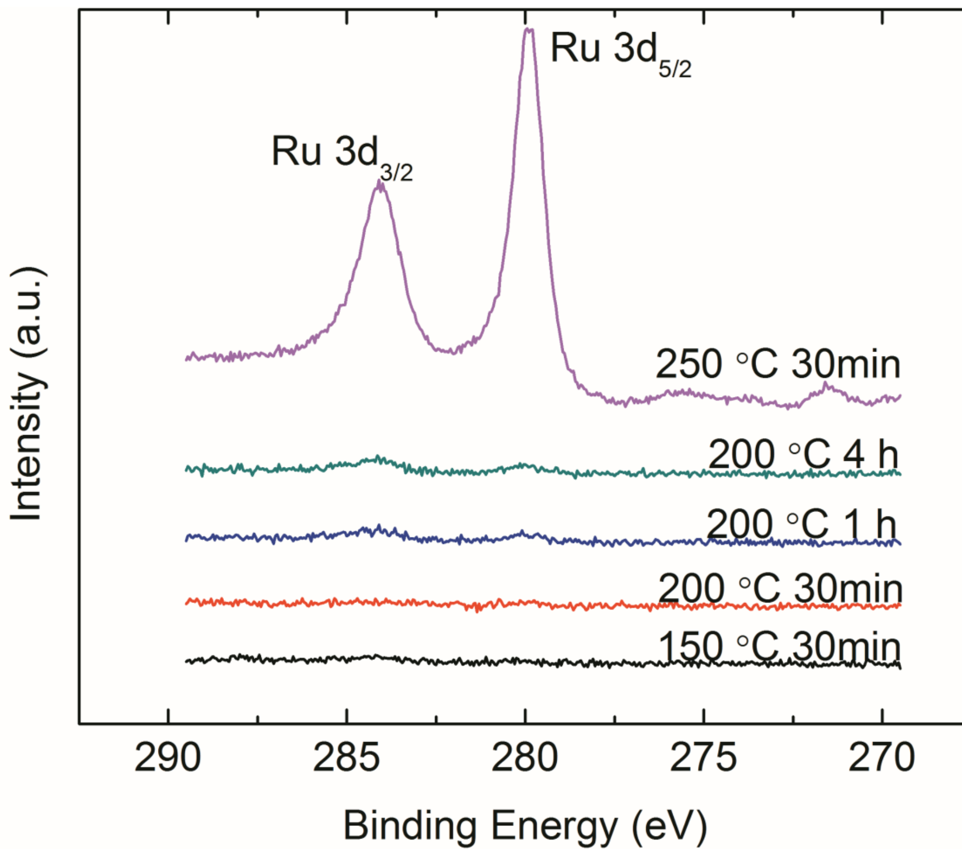

Fig. 4.8 XPS scans of the Ru 3d core level for 10 nm Cu films on oxidized as-received Ru substrates upon annealing as indicated.

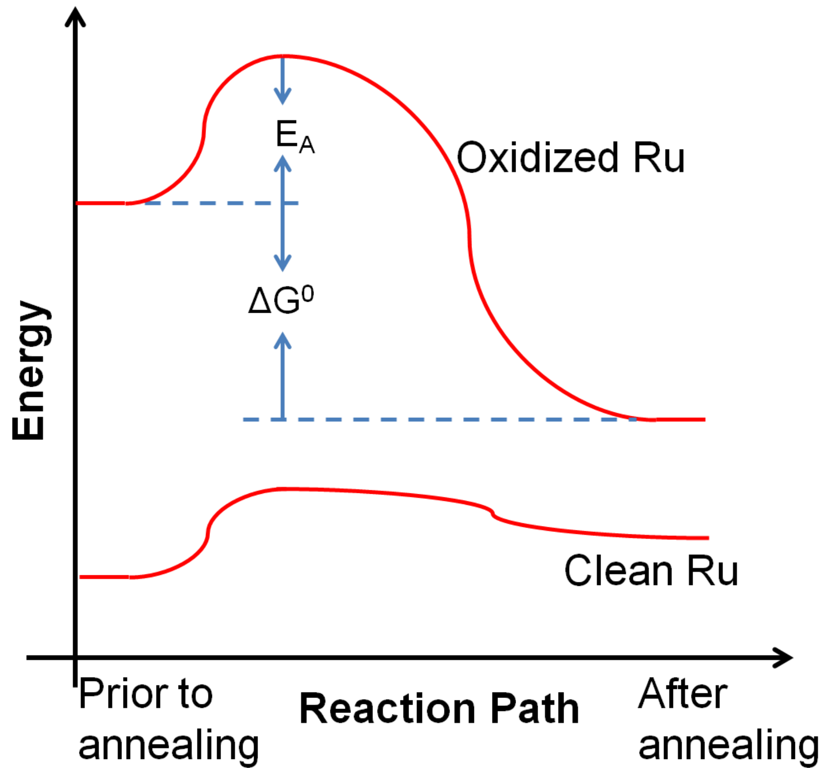

Fig. 4.9 Schematic of possible reaction paths for vacuum annealing Cu films on Ru oxidized and clean substrates.

Apparently, when the Ru substrates are oxidized, the reduced substrate surface energy due to oxidation and increased interface surface energy due to unsatisfied bonding lead to a relatively large contact angle. The contact angle, $\theta_{D,}$ of the exposed surface then exceeds the critical condition, and the surface rapidly islands. In contrast, when the oxide free Ru substrates are used, the substrate surface energy is increased and the interface surface energy is decreased compared to oxidized Ru leading to a smaller contact angle. The film is then stable against islanding.

The surface energy terms have been discussed to explain the thermal stability, grain boundary grooving and island formation. Clearly, the oxidation of

the film plays a critical role in the surface energies. We have determined that the Ru native oxide layer is ~2 monolayers, and after H_2 plasma processing, the Ru oxide has been reduced, resulting in a clean metallic surface. As discussed above, the adsorbed oxygen remains in the film; however, a metallic Ru substrate with adsorbed oxygen does not result in evident Cu de-wetting upon annealing. The results established that the surface of the substrate is critical to Cu adhesion and that an oxide of ~2 monolayers influences the stability of a Cu film on the Ru surface. The subsurface oxygen in the grain boundaries provides a negligible contribution to the surface energy and the Cu thermal stability.

4.5 Conclusion

The RuO_2 surface oxide formed on a Ru adhesion layer can be effectively removed using a remote H_2 plasma process at room temperature. The residual O in the Ru after this treatment is attributed to absorbed oxygen in the subsurface grain boundaries. However, vacuum annealing at 150 ℃ substantially removes both the surface and subsurface oxygen. We argue that above 150 ℃ residual carbon diffuses and reacts with the oxide which desorbs as CO_2.

For Cu on an oxidized Ru surface islanding, is observed upon annealing at 250 ℃. However, Cu on a H_2 plasma cleaned surface is stable to ~450 ℃. The grain boundary grooving model has been suggested to describe the morphological changes. After the initial Cu deposition, a continuous film covers the substrate. As surface diffusion is enabled, the grain boundaries shrink, and the contact angle increases until the system reaches the lowest energy configuration. Once the

oxidized substrate is exposed, the increased interface energy and reduced substrate surface energy drive the system to Cu island formation.

In this work, we conclude that a room temperature H_2 plasma process reduces the RuO_2 surface oxide on the Ru adhesion layer and substantially enhances the Cu film thermal stability to the point that the films are stable at 450 ℃. The presence of the surface oxide has been determined to be the critical aspect that leads to islanding which is attributed to a reduced Ru surface energy and an increased Ru/Cu interface energy.

REFERENCES

1. S. Murarka, Mater. Sci. Eng., R19, 87(1997).
2. C. Hu, J. Harper, Mater. Chem. Phys., 52, 5 (1998).
3. R. Gutmann, T. Chow, S. Lakshminarayanan, D. Price, J. Steigerwald, L. You and S. Murarka, Thin Solid Films, 270, 472(1995).
4. R. Rosenberg, D. Edelstein, C.Hu, and K. Rodbell, Annu. Rev. Mater. Sci., 30, 229(2000).
5. International Technology Roadmap for Semiconductors, Semiconductor Industry Association, http://www.itrs.net/Links/2010ITRS/Home2010.htm (2010).
6. R. Kröger, M. Eizenberg, D. Cong, N. Yoshida, L. Chen, S. Ramaswami, and D. Carl, J. Electrochem. Soc. 146, 3248 (1999).
7. G. Han, Y, Wu, P. Luo, J. Qiu and T, Chong, Solid State Commun. 126, 479 (2003).
8. C. Yang, S. Cohen, T. Shaw, P. Wang, T. Nogami and D. Edelstein, IEEE Electron Device Lett. 31, 722 (2010).
9. Y.-S. Kim, D.-L. Bae, H. Yang, H.-S. Shin, G.-W. Wang, J. Senkevich, and T.-M. Lu, J. Electrochem. Soc. 152, C89 (2005).
10. B. Johnson, R. Amster and L. Vanasupa, J. Electron. Mater. 27, 923(1998).
11. L. Leul, D. Norton, L. White and T. Anderson, Appl. Phys. Lett. 92, 111917(2008).
12. D. Josell, C. Witt and T. Moffat, Electronchem. Solid-State Lett. 9, C41 (2006).

13. H. Kim, T. Koseki, T. Ohba, T. Ohta, T. Kojima, H. Sato and Y. Shimogaki, J. Electrochem. Soc. 152, G594 (2005).

14. O.-K. Kwon, J.-H. Kim, H.-S. Park and S.-W. Kang, J. Electrochem. Soc. 151, G109 (2004).

15. C. Chang and F. Pan, J. Electrochem. Soc., 158, G97 (2011).

16. T. Chakraborty, D. Greenslit and T. Eisenbraun, J. Vac Sci. Technol. B, 29, 1071 (2011).

17. K. Tu, J. Appl. Phys. 94, 5451 (2003).

18. T. Madey, N. Faradzhev, B. Yakshinskiy, N. Edwards, Appl. Surf. Sci. 253, 1691-1708 (2006).

19. H. Kim and Y. Shimogaki, J. Electrochem. Soc. 154, G13 (2007).

20. D. Danielson, D. Sparacin, J. Michel and L. Kimerling, J. Appl. Phys. 100, 083507 (2006).

21. J.-Y. Kwon, T.-S. Yoon, K.-B. Kim and S.-H. Min, J. Appl. Phys. 93, 3270 (2003).

22. X. Liu, S. Gill, F. Tang, S. King, R. Nemanich, J. Vac Sci. Technol. B, 30, 031212 (2012).

23. Y. He, A. Goriachko, C.Korte, A. Farkas, G. Mellau, P. Dudin, L. Gregoratti, A. Barinov, M. Kiskinova, A. Stierle, N. Kasper, S. Bajt and H. Over, J. Phys. Chem. C, 111, 10988 (2007).

24. M. Gladys, A. Mikkelsen, J. Andersen and G. Held, Chem. Phys. Lett. 414, 311 (2005).

25. J. Shen, A. Adnot and S. Kaliaguine, Appl. Surf. Sci. 51, 47 (1991).

26. Y. Iwasaki, A. Izumi, H. Tsurumaki, A. Namiki, H. Oizumi and I. Nishiyama, Appl. Surf. Sci. 253, 8699 (2007).

27. L. Belau, J.-Y. Park, T. Liang, H. Seo and G. Somorjai, J. Vac. Sci. Technol. B 27, 1919 (2009).

28. H. Oizumi, A. Izumi, K. Motai, I. Nishiyama and A. Namiki, Jpn. J. Appl. Phys. 46, L633 (2007).

29. I. Nishiyama, H. Oizumi, K. Motai, A. Izumi, T. Ueno, H. Akiyama and A. Namiki, J. Vac. Sci. Technol. B 23, 3129 (2005).

30. V. Bermudez, J. Appl. Phys. 80, 1190 (1996).

31. F. Cotton and J. Mague, Inorg. Chem. 5, 317 (1966).

32. S. Huefner, Springer-Verlag Berlin Heidelberg New York, 2003.

33. J.-H. Ahn, W.-J. Lee and H.-G. Kim, Materials Lett. 38, 250 (1999).

34. Y. Kaga, Y. Abe, M. Kawamura and K. Sasaki, Jpn. J. Appl. Phys. 38, 3689 (1999).

35. J. Wang, C. Y. Fan, K. Jacobi, and G. Ertl, J. Phys. Chem. B 106, 3422 (2002).

36. J. Wang, C. Y. Fan, K. Jacobi, and G. Ertl, Surf. Sci. 481, 113 (2001).

37. M. Niibe, K. Koida and Y. Kakutani, J. Vac. Sci. Technol. B 26, 2230 (2008).

38. F. Genin, W. Mullins and P. Wynblatt, Acta. Metall. Mater. 40, 3239 (1992).

39. K. Miller, F. Lange and D. Marshall, J. Mater. Res. 5, 151 (1990).

Chapter 5

THERMAL STABILITY OF TI, PT AND RU INTERFACIAL LAYERS BETWEEN SEEDLESS COPPER AND A TANTALUM DIFFUSION BARRIER

5.1 Abstract

The thermal stability of 7 nm Ti, Pt and Ru interfacial adhesion layers between Cu film (10 nm) and a Ta barrier layer (4 nm) have been investigated. The barrier properties and interfacial stability have been evaluated by Rutherford backscattering spectrometry (RBS). Atomic force microscopy was used to measure the surfaces before and after annealing and, all the surfaces are relatively smooth excluding islanding or de-wetting phenomena as a cause of the instability. The RBS showed no discernible diffusion across the adhesion layer/Ta and Ta/Si interfaces which provides a stable underlying layer. For a Ti interfacial layer RBS indicates that during 400 ℃ annealing Ti interdiffuses through the Cu film and accumulates at the surface. For the Pt/Cu system Pt interdiffuion is detected which is less evident than Ti. Among the three adhesion layer candidates, Ru shows negligible diffusion into the Cu film indicating thermal stability at 400 ℃.

5.2 Introduction

Copper has been well studied as an interconnect material in advanced metallization technology due to its resistance to electromigration and its lower resistivity compared to aluminum [1-5]. Traditionally, interconnect structures employ Ta, TaN or TiN as a barrier layer with a physical vapor deposition (PVD) Cu layer that serves as a seed to Cu electrochemical deposition [1, 6, 7]. However,

the overall thickness of the seed and barrier configuration is typically 30-40 nm [9] which exceeds the requirement for the 32 nm integrated circuit technology node. Moreover, an ultrathin diffusion barrier (<3 nm thick and below) is needed for further scaling of the technology [8]. Therefore, a configuration with a Cu-plateable layer and an ultrathin barrier is desirable to minimize the barrier thickness and eliminate the Cu-seed layer.

In Cu dual-damascene structures, electromigration failure occurs predominately in regions of poor adhesion [10] which indicates that Cu film stability substantially influences the failure of the devices. The reliability of interconnect structures with multi-layer barrier structures is significantly determined by the stability of the bi-layer interfaces [11]. Thus, different direct Cu plate layers have been considered including W, Pd, Ir, Os, Pt, Ru and Ti [12-18]. The stability of Cu on these layers represents the primary technical issue associated with this approach. The stability is essentially determined by interface interdiffusion and Cu film wettability on the underlying layer. In previous work, Kim *et al.* reported that the Cu contact angle changes after annealing for Ru and Ta substrates [17]. After thermal processing, the Cu films evolved to island structures which exposed the substrates. Also Adams *et al.* reported detecting Ti segregated to the Cu free surface during 500 ℃ annealing [19]. Therefore it is necessary to investigate barrier properties and Cu wettability to determine the applicability of each direct plate material.

In a previous study, we reported that a 10 nm Cu film on a Ru substrate with a layer of native oxide tends to island after 400 ℃ vacuum annealing [20].

The islanding was driven by surface and interface energies where the reduced substrate surface energy and increased interface energy led to the island formation. In the present work, we examine both the surface morphology evolution and interfacial diffusion during annealing. Ti, Pt and Ru are selected as adhesion layer candidates for this study. Ti has been previously investigated for improved wetting properties with Cu [21]. Pt is a high melting point transition metal that is resistant to oxidation. As a reference, Ru is included since a cleaned Ru surface exhibits stable interfaces with Cu films upon annealing to 450 ℃ [20].

In this study test structures have been fabricated which included a 4 nm Ta barrier layer deposited on an oxidized Si wafer. The metallic adhesion layer (Ti, Pt and Ru (7 nm)) was deposited next, followed by a 10 nm Cu film. The films were investigated before and after vacuum annealing at 400 ℃. The stability of the structure was characterized by *in-situ* x-ray photoelectron spectroscopy (XPS), and *ex-situ* Rutherford backscattering spectrometry (RBS) and atomic force microscopy (AFM).

5.3 Experimental

The experiments were accomplished *in-situ* using an integrated ultrahigh vacuum (UHV) system. The UHV system is maintained at ~$5x10^{-10}$ Torr with multiple chambers interconnected through a ~20 m linear transfer line. The experiments in this study involve the following systems: remote H_2 plasma chamber for cleaning and vacuum annealing, electron beam evaporation for Ta, Ti, Pt, Ru and Cu film growth, and XPS for core level analysis. After completing all

in-situ measurements the samples were removed and analyzed with RBS for film stoichiometry and interdiffusion and AFM for surface morphology.

The samples were grown on 25mm dia p-type, boron doped, (100) silicon wafers with a resistivity of 0.006-0.01 Ω·cm. The oxidized Si wafers were cleaned in an ultrasonic acetone bath for 15 min, an ultrasonic methanol bath for another 15 min, and dried with ultra-high purity nitrogen gas. Then the Si substrate is mounted onto a molybdenum sample holder using tantalum wires. After transferring into the UHV system, the oxidized Si (100) surfaces are cleaned using a remote H_2 plasma process [20]. The plasma treatment conditions are as follows: rf power maintained at 30 W, H_2 pressure of 60 mTorr, substrate at room temperature, and H_2 gas flow of 90 standard cubic centimeter per minute (sccm).

To investigate the thermal stability for the different interfacial adhesion layers, a typical multi-layer metallized structure was deposited on an oxidized Si substrate (Fig. 5.1). A 4 nm Ta barrier layer was deposited on the cleaned, oxidized Si wafer followed by a 7 nm adhesion layer (Ti, Pt and Ru respectively), and finally, the 10 nm Cu film was deposited. The e-beam metallization system employed a Thermionics e-GUN™ evaporation source (model 100-0050) with a chamber base pressure of 4×10^{-10} torr. For each layer a growth rate of 0.01 nm/s was maintained with a quartz crystal thickness rate meter. After each deposition step, the samples were characterized by *in-situ* XPS. The XPS characterization is performed at a base pressure of 5×10^{-10} Torr using a VG Clam II spectrometer operated with a Mg Kα x-ray source (hν=1253.6 eV). The annealing was then conducted in the plasma chamber using a tungsten irradiation filament heater

located behind the sample holder. Samples were annealed for 30 min at 400 ℃. During annealing, the sample was heated to constant temperature (calibrated with a Mikron-M90Q infrared pyrometer), and monitored with a Eurotherm 808 thermocouple controller. The thermocouple was located behind the center of the Si wafer. The XPS characterization was conducted again after annealing.

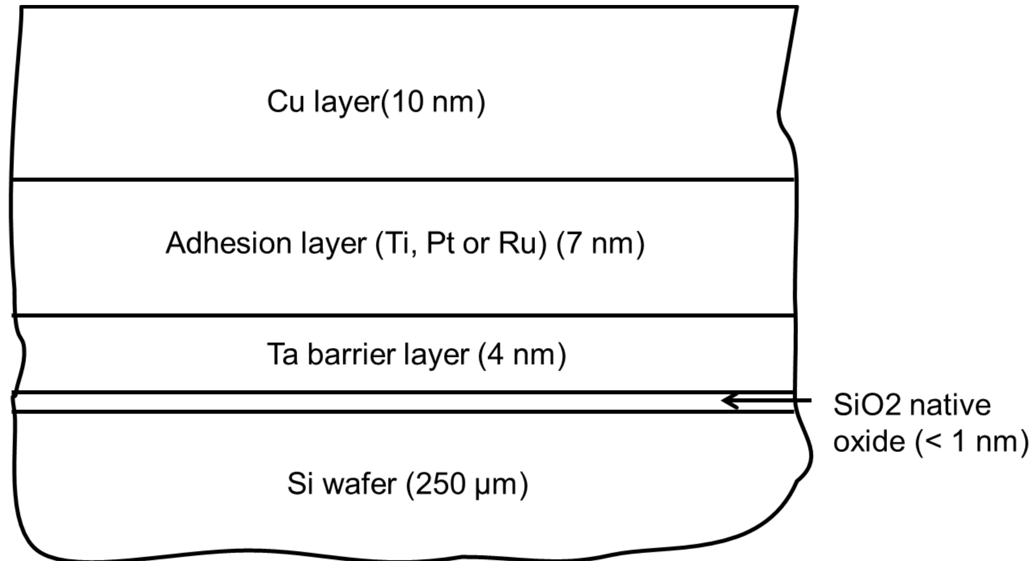

Fig. 5.1 A schematic of the multilayer structure with pertinent length scales.

After *in-situ* XPS characterization, the samples were removed from the UHV system for stoichiometry and morphology measurement. A separate set of samples were prepared to serve as the as-deposited films for the AFM and RBS characterization. The morphological changes of the surfaces were observed using an Agilent™ AFM model 5500. The RBS spectra were obtained using a 1.7 MV Tandem accelerator with 2.0 and 4.3 Mev He^{2+} beams. The RUMP program was utilized for simulation and interpretation of RBS spectra [22]. The high energy and low energy cut-offs of each peak are represented respectively by projecting the tangent to the scan at its half maximum points to the energy scale axis. The

full width at half maximum (FWHM) of the peaks for the as-deposited films are listed in Table 5.1. The FWHM was slightly larger than the 0.002 MeV instrument resolution.

	Cu	Ru	Ti	Pt	Ta
FWHM (MeV)	0.026	0.027	0.036	0.025	0.023

Table 5.1 The FWHM of each peak in the RBS spectra before annealing.

5.4 Result and Discussion

5.4.1 XPS and AFM characterization

To investigate the thermal stability of Cu on the various adhesion layers, Cu/Ti/Ta, Cu/Pt/Ta and Cu/Ru/Ta structures were deposited on oxidized Si wafers as described in the experimental section. XPS scans are carried out after the triple-layer deposition and after in-situ annealing. By comparing the XPS signal from the adhesion layer (Ti, Pt and Ru) before and after annealing, we are able to identify changes in the Cu film that occur due to the underlying adhesion layer. The relative surface atomic ratio before and after annealing is shown in Table 2. The surface atomic ratio is obtained from the integrated area of the XPS core levels normalized by the sensitivity factor. For Cu/Ti/Ta, the Ti 2p core level is weakly evident after Cu deposition, but after 400 ℃ annealing, the Ti 2p intensity increases significantly (Fig 5.2(a)). This increase in the Ti signal could indicate Cu film de-wetting and exposure of the Ti layer or interdiffusion of Ti into the Cu. For Cu/Pt/Ta, the Pt 3d core levels are not evident for the as-deposited film. But after 400 ℃ annealing, the 3d core level is evident, which

again could indicate either islanding or interdiffusion (Fig 5.2(b)). The Cu/Ru/Ta structure does not show an increase in the Ru signal after 400 ℃ annealing, which is consistent with our previous result [20].

Atomic Ratio	As-deposited	400 ℃ annealing
Ti/Cu	<0.02	5.85
Pt/Cu	-	0.79
Ru/Cu	-	<0.01

Table 5.2 The XPS surface atomic ratio of the three films before and after 400 ℃ annealing.

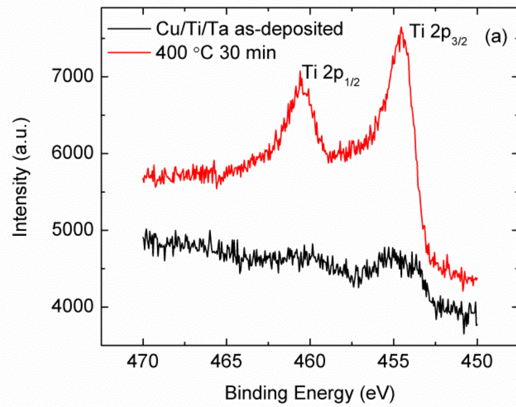

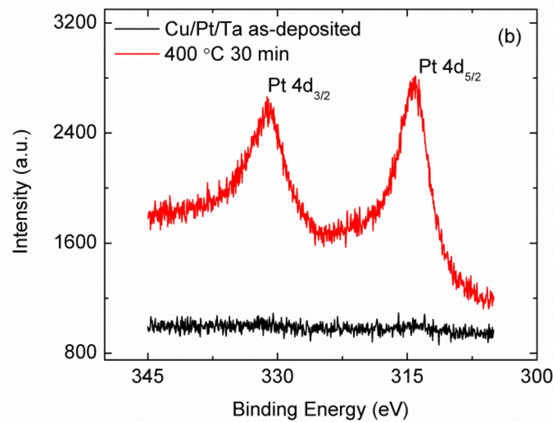

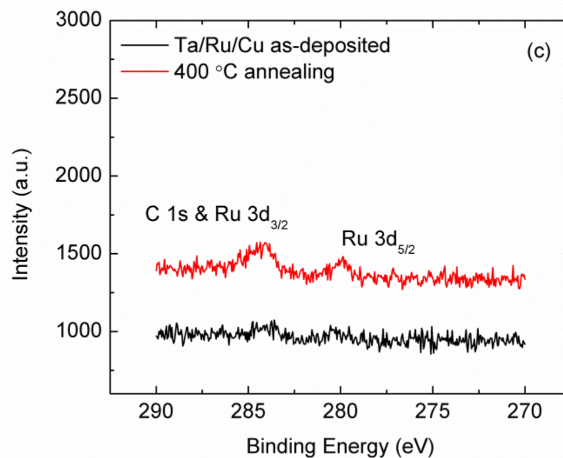

Fig. 5.2 XPS scans of (a) Ti 2p core levels for 10 nm Cu on Ti; (b) Pt 3d core levels for 10 nm Cu on Pt; (c) Ru 3d core levels for 10 nm Cu on Ru. Each frame shows scans before and after vacuum annealing at 400 ℃.

To identify if islanding occurs, the surface morphology of each sample was measured by AFM, and the results are shown in Fig. 5.3. All Cu surfaces appear uniformly covered although surface morphology changes are evident. The AFM images show no clearly discernible islanding or de-wetting phenomena. Thus, we conclude that interfacial interdiffusion occurs during annealing of the structures with Ti or Pt adhesion layers.

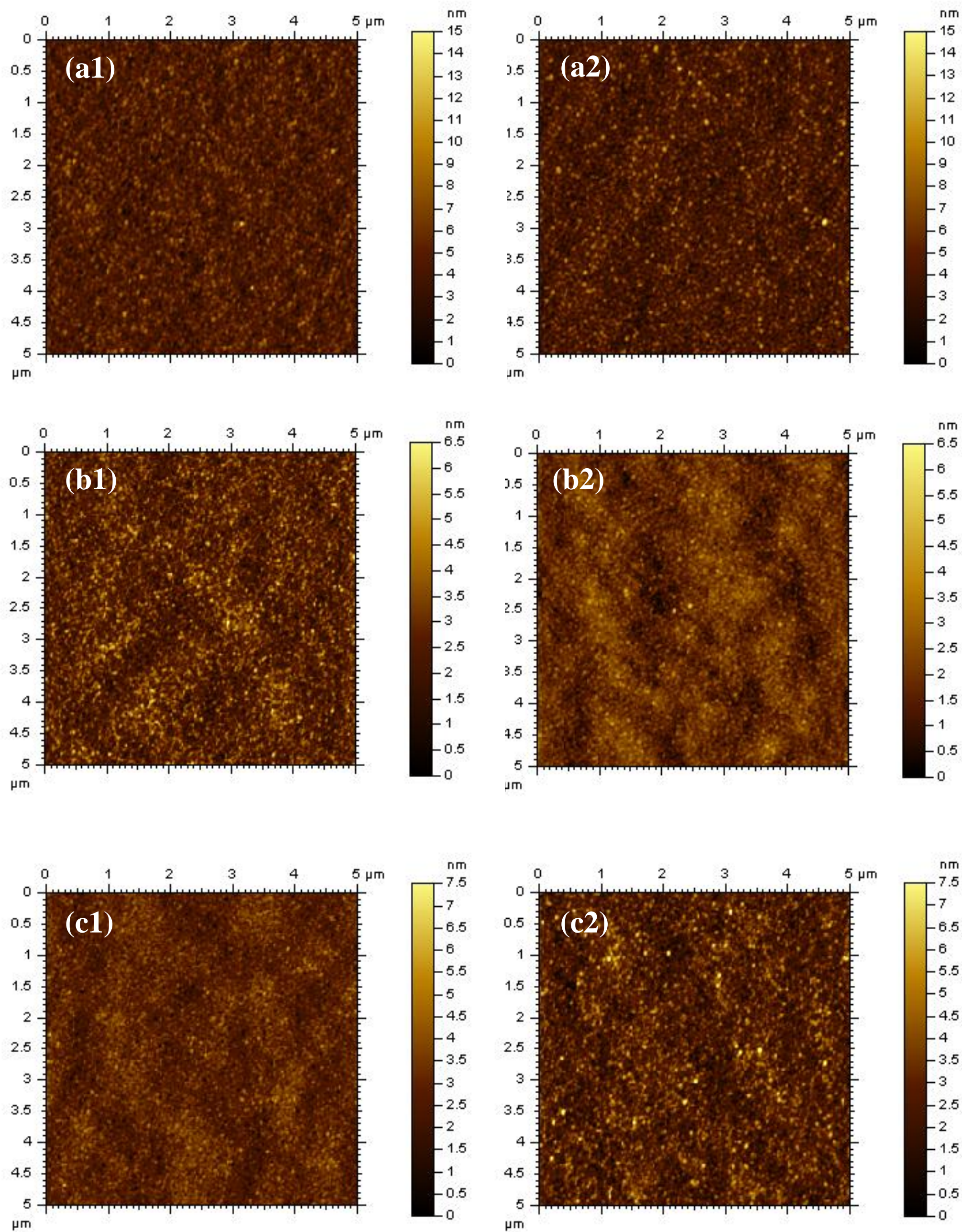

Fig. 5.3 AFM images of 10 nm Cu on different adhesion layers, (a1) Ta/Ti/Cu as-deposited, RMS = 0.61 nm; (a2) Ta/Ti/Cu 400 ℃ annealing, RMS = 1.47 nm; (b1) Ta/Pt/Cu as-deposited, RMS = 0.95 nm; (b2) Ta/Pt/Cu 400 ℃ annealing, RMS =

0.55 nm; (c1) Ta/Ru/Cu as-deposited, RMS = 1.33 nm; (c2) Ta/Ru/Cu 400 ℃ annealing, RMS = 1.1 nm.

5.4.2 RBS analysis

Fig. 5.4 shows the RBS spectra of a Cu/Ti/Ta structure before and after 400 ℃ annealing. The spectrum of the as-deposited sample shows well separated Ti, Cu, and Ta peaks. After annealing, the Ta peak is essentially unchanged indicating stable Ta/Si and Ti/Ta interfaces. The stability of these interfaces is crucial to providing a diffusion barrier layer and a smooth substrate for Cu deposition. Consequently we can conclude that the Cu-related interface variations are due to the adhesion layer and the Cu layer.

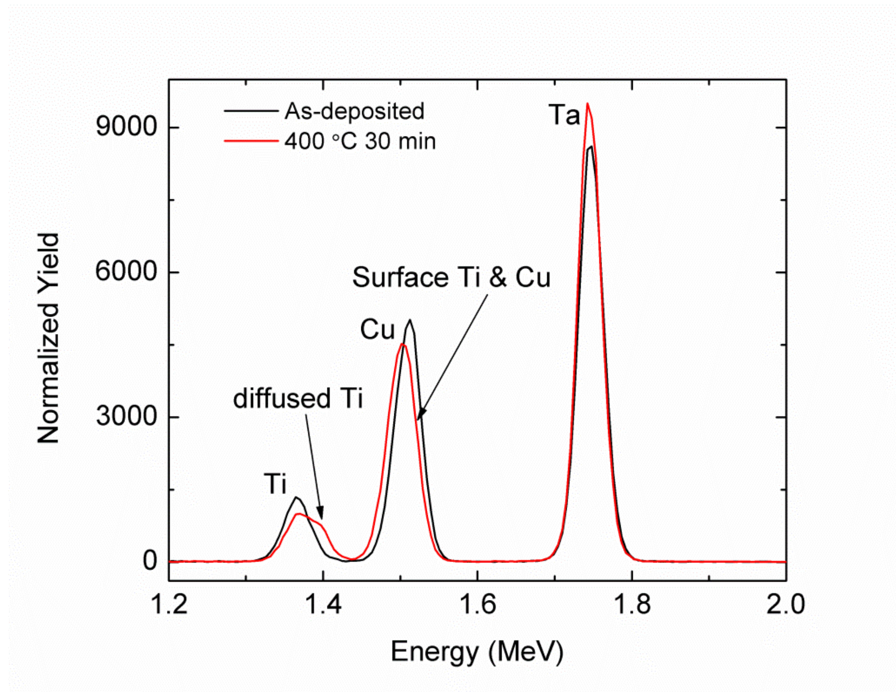

Fig. 5.4 He^{2+} RBS spectra (2 MeV) obtained from an as-deposited and 400 ℃ annealed Cu/Ti/Ta multi-layer structure.

After annealing, the high energy cut-off of the Ti peak has shifted significantly to higher energy indicating that Ti has diffused into the Cu layer. Meanwhile, the Cu peak shifts to lower energy after annealing indicating the Ti has largely accumulated on the surface. This is also supported by the XPS surface Ti/Cu atomic ratio which is over 5. After annealing, Ti and Cu interdiffuse, resulting in changes in both the XPS and RBS spectra.

The Cu/Pt/Ta system also displays evidence of interdiffusion. Since the mass of Pt and Ta are close to each other, the Ta and Pt peaks overlap in the 2 MeV spectra (Fig. 5.5(a)). With higher incident ion energy (4.3 MeV), the merged peaks can be distinguished as shown in Fig. 5.5(b). However, due to reduced energy loss as the ions pass through the film, the higher energy spectrum has reduced sensitivity. In the 2 MeV spectrum, the high energy cut-off of the Pt peak is shifted to higher energy indicating Pt is diffusing into the Cu. This is also consistent with the XPS result. But the peak position of Cu remains almost unchanged with a slight intensity drop. In the 4.3 MeV spectra, the shape of the Cu peak does not appear symmetric because it represents two separated Cu isotope peaks (Cu^{63} and Cu^{65}), and the Pt high energy edge changes slightly. Compared with the Cu/Ti/Ta system, Pt shows reduced diffusion into the Cu layer. After annealing, there is an increase of the Cu/Pt surface atomic ratio (0.79) which may indicate surface accumulation as well, but to a lesser degree Cu/Ti.

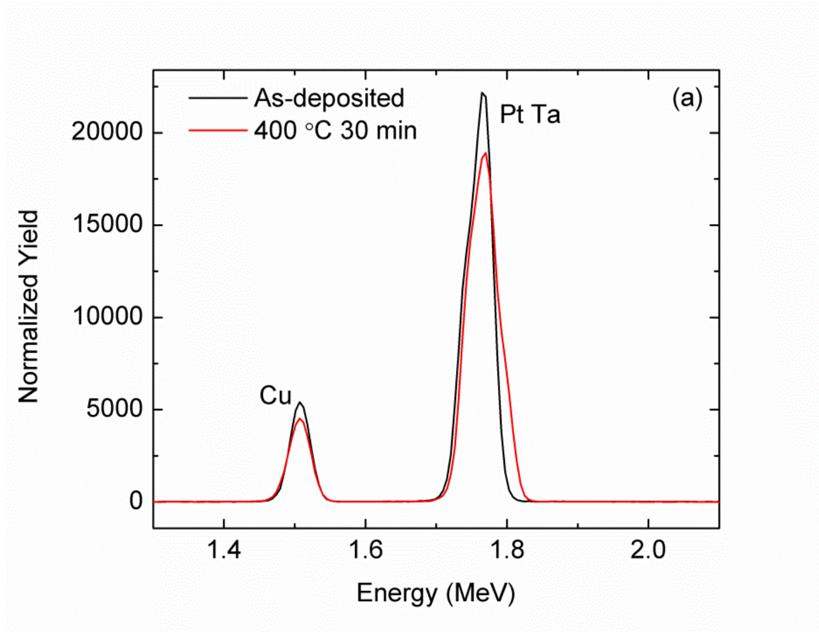

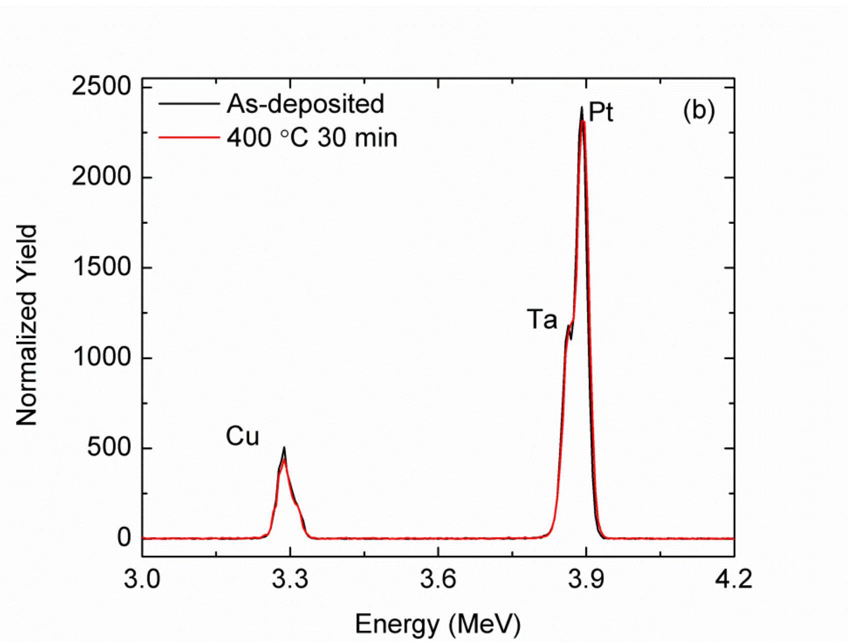

Fig. 5.5 (a) 2 MeV; and (b) 4.3 MeV He^{2+} RBS spectra obtained from as-deposited and annealed Cu/Pt/Ta multi-layer structure.

In contrast to the results of the Ti and Pt interlayers, interdiffusion was not detected in the RBS spectra for the Cu/Ru/Ta system. All layer cut-offs are

essentially aligned, and the Cu peak intensity is essentially unchanged before and after annealing. This indicates a stable interface or interdiffusion that is within the detection limit of the RBS measurement.

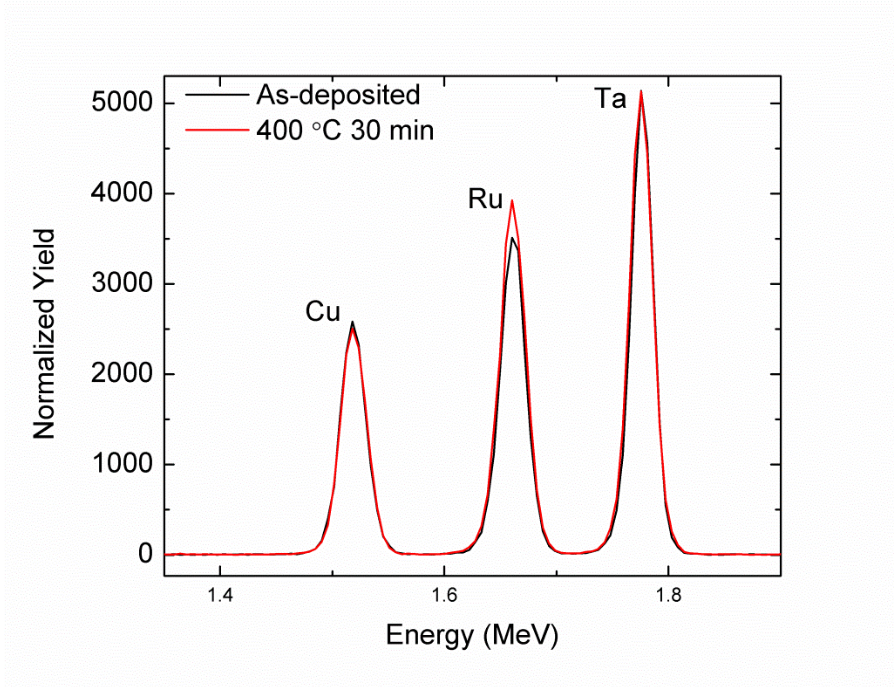

Fig. 5.6 He^{2+} RBS spectra (2 MeV) obtained from an as-deposited and annealed Cu/Ru/Ta multi-layer structure.

From the discussion above, a 4 nm Ta barrier layer has been determined to form a stable interface with oxidized Si and each of the adhesion layers at 400 ℃. Ti and Pt adhesion layers exhibit interdiffusion into Cu during 400 ℃ annealing, however, Ru exhibits improved thermal stability.

5.4.3 Cu/Ti, Cu/Pt and Cu/Ru interdiffusion analysis

The interdiffusion of Ti and Cu has been previously investigated by Iijima *et al.* who reported the temperature dependence of the interdiffusion coefficient in a Cu-Ti bilayer [23]. According to the Cu-Ti binary phase diagram [24], Ti could

react with Cu to form a range of solid solutions [25, 26]. Also, Shih *et al.* found considerable interdiffusion in the Cu/Pt system which was clearly evident in RBS spectra [27]. In the two systems, it was suggested that grain boundary diffusion contributes to the intermixing [24]. Because the annealing temperature is low compared to the Cu the melting point, the transport of solvent and solute atoms is likely driven by structural defects such as vacancies. The solvent and solute vacancies may arise during deposition and/or thermal annealing, and the diffusion process involves exchange of a vacancy and a neighboring solute (solvent) atom with a solvent (solute) atom [24]. From RBS spectra of the Cu/Pt/Ta samples, the low and high energy cut-offs of the Cu layer remain unchanged. There is a reduction of the integrated intensity of the Cu peak presumably indicating a decrease of the atomic density as Pt diffuses into the Cu layer. These results can be well described by the Kirkendall effect where two solids interdiffuse at different rates [28]. In comparison with the Cu/Ti system, the diffusion of Ti in Cu is more extensive.

For Cu/Ru/Ta, before and after annealing, the Cu/Ru interface appears stable for annealing to 400 ℃ [20]. Ru shows negligible solubility in Cu even at 900℃, and based on the binary phase diagram, there are no intermetallic compounds between Cu and Ru [29]. The stability of the Cu-Ru interface was explored using photoemission electron microscopy (PEEM), where Wei *et al.* reported Cu diffusion through defects in a 1 nm Ru thin film [30]. While the Cu-Ru system has a large positive heat of formation, He *et al.* showed simulations and results that indicated a range of metastable amorphous Cu-Ru alloys [31].

Alonso *et al.* proposed that the Cu-Ru amorphous alloy formation arises from the mutual frustration between the fcc and hcp solid solutions [32]. In our XPS scans, Ru 3d core levels after annealing are unchanged suggesting that the formation of a Cu-Ru layer did not occur or was localized to a few layers at the interface. Overall, the Cu on a Ru adhesion layer exhibits thermal stability for annealing up to 400 ℃.

5.5 Conclusion

Different Cu/(Ti, Pt or Ru)/Ta multi-layer structures have been prepared by e-beam evaporation and characterized with XPS, AFM and RBS. The Ta RBS peaks remain unchanged after annealing indicating negligible diffusion at the Ta interfaces. The stability of these interfaces is crucial to providing a diffusion barrier layer and a smooth substrate for Cu deposition.

For Cu/Ti/Ta system, both the XPS and RBS spectra indicate Ti accumulated on the surface after 400 ℃ annealing. In the Cu/Pt/Ta system, Pt interdiffusion was detected from both XPS and RBS. In comparison, it appears Ti diffused into Cu to a greater degree than Pt into Cu. The interdiffusion could be described by the Kirkendall effect. Ru as an adhesion layer exhibits a stable interface with Cu after 400 ℃ annealing. All the surfaces were relatively smooth after annealing excluding islanding or de-wetting.

In this study, we suggest that a bilayer structure of 4 nm of Ta and 7 nm of Ru will serve as a diffusion barrier and direct plate layer for Cu electrodeposition. Combined with our previous results which reported a plasma cleaning process for

removal of the Ru native oxide, it appears that this Ru/Ta bilayer could replace the current PVD-Cu/Ta barrier layer for Cu interconnects.

REFERENCES

1. R. Rosenberg, D. C. Edelstein, C.-K. Hu, and K. P. Rodbell, Annu. Rev. Mater. Sci. 30, 229 (2000).
2. S. Murarka and S. Hymes, Crit. Rev. Solid State Mater. Sci. 20, 87(1995).
3. J. Y. Park, V. K. Andleigh and C. V. Thompson, J. Appl. Phys. 85, 3546(1999).
4. A. Jian, T. Kodas, R. Jairath and M. Hampde-Smith, J. Vac. Sci. Technol. B 11, 2107(1993).
5. S. Murarka, R. Gutmann, A. Kaloyeros and W. Lanford, Thin Solid Films 236, 257(1993).
6. R. Krögera, M. Eizenberga, D. Congb, N. Yoshidab, L. Y. Chenb, S. Ramaswamib and D. Carlb, J. Electrochem. Soc. 146, 3248(1999).
7. Y. S. Kim and Y, Shimogaki, J. Vac. Sci. Technol. A 19, 2642(2001).
8. International Technology Roadmap for Semiconductors, Semiconductor Industry Association, http://www.itrs.net/Links/2011ITRS/Home2011.htm. (2012)
9. C. Yang, S. Cohen, T. Shaw, P. Wang, T. Nogami and D. Edelstein, IEEE Electron Device Lett., 31, 722 (2010).
10. K. Tu, J. Appl. Phys. 94, 5451 (2003).
11. P. Kumar, I. Dutta, M. S. Bakir, J. Electron. Mater. 41, 322(2012).
12. Y.-S. Kim, D.-L. Bae, H. Yang, H.-S. Shin, G.-W. Wang, J. Senkevich, and T.-M. Lu, J. Electrochem. Soc. 152, C89 (2005).
13. B. Johnson, R. Amster and L. Vanasupa, J. Electron. Mater. 27, 923(1998).

14. L. Leul, D. Norton, L. White and T. Anderson, Appl. Phys. Lett. 92, 111917(2008).
15. D. Josell, C. Witt and T. Moffat, Electrochem. Solid-State Lett. 9, C41 (2006).
16. M. Garza, J. Liu, N.P. Mgtoto and J. A. Kelber, Appl. Surf. Sci. 222, 253(20023).
17. H. Kim, T. Koseki, T. Ohba, T. Ohta, T. Kojima, H. Sato and Y. Shimogaki, J. Electrochem. Soc. 152, G594 (2005).
18. H. Ono, T. Nakano and T. Ohta, Appl. Phys. Lett. 64, 1511 (1994).
19. Daniel Adams, T. L. Alford, S. A. Rafalski, M. J. Rack, S. W. Russell, M. J. Kim and J. W. Mayer, Mater. Chem. Phys. 43, 145(1996).
20. X. Liu, C. Zhu, B. Eller, T. Sun, C. Jezewski, S. King, R. Nemanich, J. Vac. Sci. Technol. B 30, 052203 (2012).
21. C-C Lin, R-B Chen and R-K Shiue, J. Mater. Sci. 36, 2145(2001).
22. L.R. Doolittle, Nucl. Inst. Meth. B 9, 344 (1985).
23. Y. Iijima, K. Hoshino and K. Hirano, Metall Trans A, 8 997(1977)
24. J. L. Murray, J. Phase Equilib. Diff. 4, 81(1983).
25. X. Luo, Y. Yang, J. Li, Y. Mei, M. Yuan and Y. Chen, Composites Part A 38, 2102(2007).
26. K. Okmoto, J. Phase Equilbria 23, 549(2002).
27. D. Y. Shih, C. A. Chang, J. Paraszczak, S. Nunes and J. Cataldo, J. Appl. Phys. 70, 3052(1991).
28. A. D. Smigelskas, E. O. Kirkendall, Trans. AIME 171, 130 (1947).
29. H. Okamoto, J. Phase Equilib. Diff. 13, 440(1992).

30. W. Wei, S. L. Parker, Y.-M. Sun, and J. M. White, G.Xiong, A. G. Joly, K. M. Beck, and W. P. Hessa, Appl. Phys. Lett. 90, 111906(2007).

31. X. He, S. Liang, J. Li, and B. Liu, Phys. Rev. B 75, 045431(2007)

32. J.A. Alonso and R. Hojvat de Tendler, Phys. Chem. Liq. 46, 669(2008).

Chapter 6

SUMMARY AND FUTURE WORK

6.1 Summary

The research described in this dissertation has addressed the following topics: 1) The N_2/H_2 plasma induced modifications of low-k ILD dielectrics and contamination reduction of CMP Cu films. Plasma surface reactions with low-k ILD materials and Cu surfaces have been investigated. 2) Characterization of oxide stability and cleaning of Ru surfaces as well as the Cu thermal stability on oxidized and as-cleaned Ru adhesion layers. It was proposed that changes in surface and interface energy explain the stability or islanding of Cu on different Ru substrates. 3) Thermal stability of Ti, Pt and Ru interfacial layers (7 nm) between seedless copper (10 nm) and a tantalum diffusion barrier (4 nm). Interdiffusion between Ti-Cu and Pt-Cu after 400 ℃ vacuum annealing was observed by RBS. In addition, the accumulation of Ti and Pt onto the Cu surfaces after annealing was observed by XPS.

Carbon abstraction for low-k ILD materials during a range of N_2/H_2 plasma processing was evaluated and discussed. An initial N_2 plasma pre-treatment was proposed to “seal” the surface pores and protect the carbon groups. With the formation of N-C=O bonds at the surface, the low-k ILD surface retards H radical diffusion, which results in reduced carbon abstraction. It was found that elevated temperature enhanced the stability of the low-k ILD layer presumably by inhibiting the formation of polar Si-OH structures. Our experiments established that OH incorporation leads to a more significant increase in dielectric constant

than the change in network topography. The 380 ℃ processing temperature is within the overall temperature budget for interconnect processes according to International Technology Roadmap for semiconductors 2010. Moreover, the elevated temperature effectively induces the copper oxide to react with carbon contamination leading to a reduction in both carbon and oxide contamination. The presence of H radicals also contributes to the removal of carbonates and reduction of the remaining oxide. The active species in the N_2 plasma may react with C-C bonded structures. Thus, the elevated temperature N_2/H_2 plasma processes that minimize ILD damage also result in efficient contamination removal from the CMP Cu surfaces.

For the as-received Ru sample, the presence of oxygen is identified by an evident O 1s XPS peak. The O 1s peak has a component at 529.8 eV which corresponds to oxygen atoms from RuO_2 (O^{2-}) and another component at 531.2 eV which corresponds to sub-surface grain boundary oxygen. The ~2 monolayer native Ru oxide was reduced after H_2 plasma processing or a vacuum annealing at 150 ℃. The as-cleaned Ru surface substantially enhances the Cu film thermal stability to the point that the films are stable at 450 ℃. The thermally induced Cu film islanding was detected using *in-situ* XPS when the presence of the Ru 3d core levels indicated islanding. The presence of the surface oxide has been determined to be the critical aspect that leads to islanding which is attributed to a reduced Ru surface energy and an increased Ru/Cu interface energy. A grain boundary grooving model has been proposed to describe the morphological changes. After the initial Cu deposition, a continuous film covers the substrate. As

surface diffusion is enabled, the grain boundaries shrink, and the contact angle increases until the system reaches the lowest energy configuration. Once the oxidized substrate is exposed, the increased interface energy and reduced substrate surface energy drive the system to Cu island formation.

Different Cu/(Ti, Pt or Ru)/Ta multi-layer structures have been prepared and characterized with XPS, AFM and RBS. The Ta RBS peaks remain unchanged after annealing indicating negligible diffusion at the Ta interfaces. For the Cu/Ti/Ta and Cu/Pt/Ta system, after annealing, the high energy cut-off of the Ti or Pt peak has shifted to higher energy indicating that Ti or Pt has diffused into the Cu layer. Meanwhile, the Ti/Cu and Pt/Cu surface atomic ratio increased indicating accumulation of Ti or Pt onto the Cu surfaces. In comparison, it appears Ti diffused into Cu to a greater degree than Pt into Cu. These results can be well described by the Kirkendall effect where two solids interdiffuse at different rates. Ru as an adhesion layer exhibits a stable interface with Cu after 400 ℃ annealing. After annealing the RBS peaks and Ru core levels remain essentially unchanged indicating the thermal stability. All surfaces were relatively smooth after annealing excluding islanding or de-wetting. It is suggested that a bilayer structure of 4 nm of Ta and 7 nm of Ru will serve as a diffusion barrier and direct plate layer for Cu electrodeposition. Combined with previous results of a plasma cleaning process for removal of the Ru native oxide, it appears that this Ru/Ta bilayer could replace the current PVD-Cu/Ta barrier layer for Cu interconnects.

6.2 Future work

6.2.1 Plasma interaction at surface of ultra low-k ILD (k<2.2)

Porous-SiCOH dielectric materials are being considered as low-k materials which could be implemented in ULSI technology. However, as indicated in the ITRS 2010 interconnects section, in the 19 nm technology node and below, a dielectric constant lower than 2.2 is has been specified. Preliminary results have reported deposition and processing [1-3] of ultra low-k ILD. In our previous study, we reported that H_2 plasma processing results in significant carbon group abstraction and polar Si-OH formation, leading to an increase of the dielectric constant [4]. Thus, for post CMP cleaning processes, the simultaneous preparation for both CMP Cu and ultra low-k ILD surface is studied. Currently, the focus is on porous dielectric films with a dielectric constant of ~2.2. Due to increased diffusion occurring in the ultra low-k ILD films, multiple plasma processing steps are proposed. Also it is proposed to separate the effects induced by UV-light [5], ions [6] and neutral radicals [7]. A UV-light filter may be utilized to control the UV-light radiation and a biased substrate will be used to retard the ion bombardment. The surface properties for various plasma processing will be characterized using *in-situ* XPS and FTIR will be employed to monitor the bulk bonding changes which may determine the dielectric constant. The k value is determined using C-V measurements of capacitance structure.

6.2.2 Thermochemical stability of ultra-thin direct plate Cu barrier materials

The 2010 ITRS Emerging Research Materials chapter forecasts that < 2 nm thick barrier materials will be needed by 2015 and < 1 nm barrier materials by 2021. While numerous barrier materials have been suggested and evaluated, few

tests of these materials have been reported at thicknesses <2 nm, and there have been effectively no studies directly comparing performance of a range of potential materials. Such a comparison is needed to identify the most appropriate material (or class of materials). Also of vital importance is the need to understand the interplay between pre-barrier deposition surface preparation and the barrier material's resistance to Cu diffusion [8-11]. Therefore it is proposed to complete a survey of materials including Ta, TaN, Ru, and several other ALD compatible materials and novel SAMs and other industry suggested materials. This research would seek to identify materials most likely for success in the < 2 nm regime.

REFERENCES

1. M-C. Tseng and Y-L. Liu, Polymer 51, 5567(2010).

2. H. Yuan, J. Xu and L. Xie, Mater. Chem. Phys. 129, 1195(2011).

3. P. Lazzeria, G. S. Oehrleinb, G. J. Stueberb, R. McGowanc, E. Buschc, S. Pederzolia, C. Jeynesd, M. Bersania and M. Anderlea, Thin Solid Films 516, 3697 (2008).

4. X. Liu, C. Zhu, B. Eller, T. Sun, C. Jezewski, S. King, R. Nemanich, J. Vac. Sci. Technol. B 30, 052203 (2012)

5. T. W. Scattergood, C. P. McKay, W. J. Borucki, L. P. Giver, H. van Ghyseghem, J. E. Parris and S. L. Miller, Icarus 81, 413 (1986).

6. N. Matsunaga, H. Okumura, B. Jinnai and S. Samukawa, Jpn. J. Appl. Phys. 49, 04DB06 (2010).

7. H. Shi, H. Huang, J. Bao, J. Liu, P. S. Ho, Y. Zhou, J. T. Pender, M. D. Armacost, and D. Kyser, J. Vac. Sci. Technol. B 30, 011206 (2012)

8. Juline Shoeb, Ming Mei Wang, and Mark J. Kushner, J. Vac. Sci. Technol. A 30, 041303 (2012)

9. S. W. King, R.J. Nemanich, and R.F. Davis, Journal of the Electrochemical Society, 146 2648 (1999)

10. S. W. King, J. P. Barnak, M.D. Bremser, K.M. Tracy, C. Ronning, R. J. Nemanich, and R.F. Davis, Journal of Applied Physics, 84 5284 (1998)

11. R. J. Carter, J. R. Hauser and R. J. Nemanich, J. Electrochem. Soc. 147 , 3512(2000)

REFERENCES

A. D. Smigelskas, *et al.*, Trans. AIME 171, 130 (1947).

A. Grill, *et al.*, J. Appl. Phys. 94, 6697 (2003).

A. Grill, Annu. Rev. Mater. Res. 39, 49 (2009).

A. Grill, *et al.*, Res. Soc. Symp. Proc. 443, 155(1997).

A. Grill, *et al.*, J. Appl. Phys. 98, 074502 (2005).

A. Jian, *et al.*, J. Vac. Sci. Technol. B 11, 2107(1993).

A. M. Urbanowicz, *et al.*, J. Electrochem. Soc. 157, H565 (2010).

B. Johnson, *et al.*, J. Electron. Mater. 27, 923(1998).

C. B. Drake, J. Vac. Sci. Technol. 13, 761(1976).

C. Chang, *et al.*, J. Electrochem. Soc., 158, G97 (2011).

C. Hu, *et al.*, Mater. Chem. Phys., 52, 5 (1998).

C. Yang, *et al.*, IEEE Electron Device Lett., 31, 722 (2010).

C. Zhu, Ph.D. thesis, Arizona State University.

C-C Lin, *et al.*, J. Mater. Sci. 36, 2145(2001).

C-K Hu, *et al.*, Mater. Chem. Phys. 51, 5(1998).

D. Adams, *et al.*, Mater. Chem. Phys. 43, 145(1996).

D. Danielson, *et al.*, J. Appl. Phys. 100, 083507 (2006).

D. Edelstein, *et al.*, Reliability Physics Symposium Proceedings, 316(2004).

D. Edelstein, *et al.*, International Electron Devices Meeting, 773(2000).

D. Edelstein, *et al.*, International Electron Devices Meeting, 773(1997).

D. Josell, *et al.*, Electrochem. Solid-State Lett. 9, C41 (2006).

D. Y. Shih, *et al.*, J. Appl. Phys. 70, 3052(1991).

F. Cotton, *et al.*, Inorg. Chem. 5, 317 (1966).

F. Genin, *et al.*, Acta. Metall. Mater. 40, 3239 (1992).

G. Beamson, *et al.*, High Resolution XPS of Organic Polymers (Wiley, London, 1992).

G. E. Moore, Electronics, 38, 114 (1965).

G. Han, *et al.*, Solid State Commun. 126, 479 (2003).

G. J. Stueber, *et al.*, J. Vac. Sci. Technol. B 25, 1593(2007).

H. Abe, *et al.*, Jpn. J. Appl. Phys. 47, 1435(2008).

H. Kim, *et al.*, J. Electrochem. Soc. 154, G13 (2007).

H. Kim, *et al.*, J. Electrochem. Soc. 152, G594 (2005).

H. Oizumi, *et al.*, Jpn. J. Appl. Phys. 46, L633 (2007).

H. Okamoto, J. Phase Equilib. Diff. 13, 440(1992).

H. Ono, *et al.*, Appl. Phys. Lett. 64, 1511 (1994).

H. Shi, *et al.*, J. Vac. Sci. Technol. B 30, 011206 (2012)

H. Yuan, *et al.*, Mater. Chem. Phys. 129, 1195(2011).

I. Ames, *et al.*, IBM J. Res. Dev. 4, 461(1970).

I. Nishiyama, *et al.*, J. Vac. Sci. Technol. B 23, 3129 (2005).

International Technology Roadmap for Semiconductors, Semiconductor Industry Association, http://www.itrs.net/Links/2010ITRS/Home2010.htm (2010).

International Technology Roadmap for Semiconductors, Semiconductor Industry Association, http://www.itrs.net/Links/2011ITRS/Home2011.htm (2011)

J. A. Alonso, *et al.*, Phys. Chem. Liq. 46, 669(2008).

J. L. Murray, J. Phase Equilib. Diff. 4, 81(1983).

J. Lee, *et al.*, J. Phys. D: Appl. Phys. 43, 425201(2010).

J. Paraszczak, *et al.*, International Electron Devices Meeting, 261(1993).

J. Shen, *et al.*, Appl. Surf. Sci. 51, 47 (1991).

J. Torres, *et al.*, Microelectron. Eng. 50, 425 (2000).

J. Wang, *et al.*, J. Phys. Chem. B 106, 3422 (2002).

J. Wang, *et al.*, Surf. Sci. 481, 113 (2001).

J. Y. Park, *et al.*, J. Appl. Phys. 85, 3546(1999).

J.-H. Ahn, *et al.*, Materials Lett. 38, 250 (1999).

J.-Y. Kwon, *et al.*, J. Appl. Phys. 93, 3270 (2003).

J. Shoeb, *et al.*, J. Vac. Sci. Technol. A 30, 041303 (2012)

K. Maex, *et al.*, J. Appl. Phys. 93, 8793(2003).

K. Miller, *et al.*, J. Mater. Res. 5, 151 (1990).

K. N. Tu, J. Appl. Phys. 94, 5451 (2003).

K. Okmoto, J. Phase Equilbria 23, 549(2002).

K. Yonekura, *et al.*, J. Vac. Sci. Technol. B 22, 1071 (2004).

L. Belau, *et al.*, J. Vac. Sci. Technol. B 27, 1919 (2009).

L. Leul, *et al.*, Appl. Phys. Lett. 92, 111917(2008).

L. Prager *et al.*, Microelectron. Eng. 85, 2094 (2008).

L.R. Doolittle, Nucl. Inst. Meth. B 9, 344 (1985).

M. A. Goldman, *et al.*, J. Appl. Phys. 106, 013311 (2009).

M. A. Worsley, *et al.*, J. Appl. Phys. 101, 013305 (2007).

M. A. Worsley, *et al.*, J. Vac. Sci. Technol. B 23, 395 (2005).

M. Fukasawa, *et al.*, J. Vac. Sci. Technol. A 26, 870 (2008).

M. Garza, *et al.*, Appl. Surf. Sci. 222, 253(20023).

M. Gladys, *et al.*, Chem. Phys. Lett. 414, 311 (2005).

M. Mesi, *et al.*, Proceedings of the Fourteenth International Conference and EUROCVD-11, edited by M. Allendorf and C. Bernard (The Electrochemical Society, Pennington, NJ, 1997), pp. 278–285.

M. Niibe, *et al.*, J. Vac. Sci. Technol. B 26, 2230 (2008).

M. R. Baklanov, *et al.*, Philosophical Transactions of the Royal Society A: Mathematical, Physical and Engineering Sciences 364, 201(2006).

M. T. Bohr, International Electron Devices Meeting, 241 (1995).

M-C. Tseng, *et al*., Polymer 51, 5567(2010).

N. Matsunaga, *et al.*, Jpn. J. Appl. Phys. 49, 04DB06 (2010).

N. Posseme, *et al.*, J. Vac. Sci. Technol. B 25, 1071(2007).

O.-K. Kwon, *et al.*, J. Electrochem. Soc. 151, G109 (2004).

P. Kumar, *et al.*, J. Electron. Mater. 41, 322(2012).

P. Lazzeria, *et al.*, Thin Solid Films 516, 3697 (2008).

P. Liu, *et al.*, Jpn. J. Appl. Phys. 38, 3482 (1999).

P. Liu, *et al.*, IEEE Trans. Electron Devices 47, 1733 (2000).

R. Gutmann, *et al.*, Thin Solid Films, 270, 472(1995).

R. J. Carter, *et al.*, J. Electrochem. Soc. 147 , 3512(2000)

R. Krögera, *et al.*, J. Electrochem. Soc. 146, 3248(1999).

R. L. Deutscher, *et al.*, J. Appl. Electrochem. 16, 413 (1986).

R. P. Vaudo, *et al.*, J. Vac. Sci. Technol. B 12, 1232 (1994).

R. Rosenberg, *et al.*, Annu. Rev. Mater. Sci. 30, 229 (2000).

S. Chen, *et al.*, Thin Solid Films 519, 3897 (2011).

S. Huefner, Springer-Verlag Berlin Heidelberg New York, 2003.

S. Miyanaga, *et al.*, Thin Solid Films 518, 3509 (2010).

S. Murarka, *et al*., Crit. Rev. Solid State Mater. Sci. 20, 87(1995).

S. Murarka, Mater. Sci. Eng., R19, 87(1997).

S. Murarka, *et al.*, Thin Solid Films 236, 257(1993).

S. Murarka, *et al.*, Critical Rev. in Solid State Mater. Sci. 20, 87(2006).

S. W. King, *et al.*, J. Appl. Phys., 84 5284 (1998)

S. W. King, *et al.*, J. Electrochem. Soc. 146 2648 (1999)

S. Xu, *et al*., J. Vac. Sci. Technol. B 25, 156 (2007).

T. Chakraborty, *et al.*, J. Vac Sci. Technol. B 29, 1071 (2011).

T. Fukumura, *et al.*, Jpn. J. Appl Phys. Part 1 40, 46 (2001).

T. Homma, Mater. Sci. Eng. R 23, 243(1998).

T. Madey, *et al.*, Appl. Surf. Sci. 253, 1691-1708 (2006).

T. P. Schneider, Ph.D. thesis, North Carolina State University (1994).

T. W. Scattergood, *et al.*, Icarus 81, 413 (1986).

V. Bermudez, J. Appl. Phys. 80, 1190 (1996).

W. Volksen, *et al.*, Chem. Rev. 110, 56(2010).

W. Wei, *et al.*, Appl. Phys. Lett. 90, 111906(2007).

X. He, *et al.*, Phys. Rev. B 75, 045431(2007)

X. Hua, *et al.*, J. Vac. Sci. Technol. B 24, 1238 (2006).

X. Liu, *et al.*, J. Vac. Sci. Technol. B 30, 052203 (2012).

X. Liu, *et al*., J. Vac Sci. Technol. B, 30, 031212 (2012).

X. Luo, *et al.*, Composites Part A 38, 2102(2007).

Y. Ein-Eli, *et al.*, Electrochimica Acta, 52, 1825 (2007).

Y. Ein-Eli, *et al.*, Electrochem. Solid-State Lett. 8, B69 (2005).

Y. He, *et al.*, J. Phys. Chem. C, 111, 10988 (2007).

Y. Iijima, *et al.*, Metall Trans A, 8 997(1977)

Y. Iwasaki, *et al.*, Appl. Surf. Sci. 253, 8699 (2007).

Y. Kaga, *et al.*, Jpn. J. Appl. Phys. 38, 3689 (1999).

Y. Kim, *et al.*, J. Korean Phys Soc. 40, 94 (2002).

Y. S. Kim, *et al.*, J. Vac. Sci. Technol. A 19, 2642(2001).

Y.S. Kim, *et al.*, J. Electrochem. Soc. 152, C89 (2005).